UNIVERSITÉ CATHOLIQUE DE LOUVAIN
École Polytechnique de Louvain
ICTEAM Institute
Electrical Engineering, Antenna Research Group
1348, Louvain-la-Neuve, Belgium

Modal Analysis Methods and Design of Chipless RFID Tags with Natural Fractal Shapes

Donia OUESLATI

Thesis presented for the Ph.D. degree
in Applied Science

Examining Committee:

Christophe CRAEYE	UCL, Belgium - Supervisor
Taoufik AGUILI	UTM, Tunisia -Co_Supervisor
Ismail TEDJINI	Université Grenoble Alpes, France
Hatem RMILI	University of Monastir, Tunisia
Ridha BOUALLEGUE	University of Carthage, Tunisia
Danielle VANHOENACKER-JANVIER	UCL, Belgium- Secretary
Jean-Pierre RASKIN	UCL, Belgium - President

Private defense: 22 December 2016
Public defense: 14 February 2017, Louvain-la-Neuve, Belgium
Co-tutelle thesis agreement between UCL, Belgium and UTM, Tunisia

"Success is not the key to happiness. Happiness is the key to success. If you love what you are doing, you will be successful"

Albert Schweitzer

"Il faut rire avant que d'être heureux de peur de mourir sans avoir ri"

Jean de la Bruyère

To My Angels

My Mother, Khadija Rouissi Oueslati

Sister, Ahlem Oueslati

For their everlasting love and continued support

Acknowledgements

This thesis would not have been possible without the help of several persons who help or contributed in the preparation and completion of this joint supervision doctorate between *Université Catholique de Louvain* (UCL), Belgium and *Université Tunis el Manar* (UTM), Tunisia. First and foremost, my utmost gratitude to my supervisors, Prof. Christophe Craeye, Prof. Taoufik Aguili, and Dr. Hatem Rmili for their guidance, enthusiasm and support during these years. I am very much grateful to my doctoral jury members Prof. Danielle Vanhoenacker-Janvier, Prof. Ismail Tedjini, Prof. Ridha bouallegue, and Prof. Jean-Pierre Raskin for their suggestion and useful comments to improve this manuscript.

During my Ph.D. I had the opportunity of collaborating with many people in different Universities, *IETR, INSA-Rennes* and *CORIA, INSA Rouen, France*. I am grateful to Prof. Paul Van Dooren, Prof. François Glineur, and Prof. Isabelle Huynen for all the useful discussions and their help to solve some mathematics and electromagnetic problem. I owe them sincere thankfulness. I am very much thankful to all my professors at UTM for their teachings and guidance to have deeper knowledge in computing science and electronics area, and communication systems engineering.

It gives me an immense pleasure to thank the people who provided me unconditional support during my doctoral studies at UCL and UTM. I would like to thank Pascaline Parisot for her help in Matlab and LaTex. I am thankful to Pascaline for her frequent supervision of my works during the thesis. Every time, she accepts to review my papers, presentations, and manuscript. She was as a co-supervisor of my project. I am gratefully indebted to her for her very valuable comments on this thesis. I owe here sincere and earnest thankfulness.

I would like to also thank Shambhu Nath Jha for his collaboration during all years of my doctoral works, with him, I worked on various problems. I am also thankful to him for his first time explaining of the UCL code and the IE3D software which I used throughout the manuscript to validate my works. I am moreover thankful to my colleagues in the office, Sumit, Khaldoun, and Christopher for all the support, the respect and the professionalism during all our practical discussions. I am thankful to all antenna group. I am also thankful to François Hubin, Brigitte Dupont, David Spote, and Anthony Mazzeo for their active support in computing resource management, fabrication and measurement of the antenna systems for my project.

My thank also goes to my best friends in Louvain la Neuve (LLN), Pascaline Parisot for the fantastic moments and her big encouragements during my stay in LLN, Lamia el Fissi for her support during the professional problems and experiencing the pain of the difficult personal moments, and Yasmina Belaroussi for her encouragement even at distance. I thank Kaori, Sébastien, Emna, Cédric act.. to name few offered me kind support during my stay in LLN. Also my friends in Tunisia, Meriem Sehli, Rakia Chelouati act.. for their support during all my thesis.

I would like to specially thank my parents for their passionate patience during my doctoral works and supporting. Without their care and support, this day would have hardly come. I thank them for the many sacrifices they made for me, their unconditional support, and everything they have given me. Without them, my doctoral works would have never been started and finish. I would like dedicate my thesis works to the spirit of my grandfather Abdelbaki Rouissi. Very special thanks to my father Ali Oueslati to fending my research for more than one year to finish my research doctorate.

At last but not the least, I would like to express my sincere gratitude to the mentors of my thesis Prof. Taoufik Aguili and Dr. Hatem Rmili for the continuous support of my Ph.D study and research, and their motivation. These useful doctoral achievements would not have been possible without proper guidance, patience, motivation, enthusiasm, and immense knowledge of my doctoral supervisor Prof. Christophe Craeye. His guidance helped me in all the time of research and writing of this thesis. I express my respect and sincere thankfulness to Prof. Christophe Craeye. Finally, the funding sources from the ADRI are greatly acknowledged.

Oueslati Donia
February 14th, 2017

Abstract

Radio Frequency Identifications (RFID) systems undergo a growing demand for different functionalities, mainly for identification, tracking, and anti-counterfeiting applications. An RFID system allows the identification of objects or persons without physical contact. The RFID technology uses radio frequency (RF) waves for transmission of information between an interrogator and a tag. Nowadays, the design of the RFID tag has received great attention, which leads to an extremely low fabrication cost, a robust tagging, and a secure solution. The RFID tag comprises an antenna terminated by an integrated circuit (chip) which is powered by extracting power transmitted from the RFID reader. These tags are passive, given that they have no battery. The passive RFID system is based on the modulation of the tag's response. The passive tag is still relatively expensive, which relates to the cost of the tag's chip. Due to the lack of own power sources, the read range over which the chip can be powered is limited. Hence, several research programs are developing chipless RFID tags without ICs in an effort to fabricate cheaper tags with a small size.

The chipless tag is a fully-passive circuit and uses frequency signatures for data encoding. The tag consists of a scatterer with a shape coupled to transmitting and receiving antennas. The vast majority of chipless RFID systems achieve a specific electromagnetic signature based on the electromagnetic properties of materials and/or the design of conductor layouts.

The important challenges of the development of chipless RFID tags are the extraction of rich information with good data capacity from the tag based just on the shape of the tag. Also, the goal of the recent design of the chipless tag is the avoidance of strong interference from the environment of the tag. The main objective of this thesis is to propose a technique to solve those challenges. In other words, this thesis is focused on the synthesis of the electromagnetic signature of chipless RFID tags. A reader consisting of multiple transmitting and receiving antennas is reported in this doctoral work. The reader provides full access to the information, while specific efforts are made to discriminate the frequency signature of the tag from that of the environment.

Since the electromagnetic characteristics of the chipless RFID tag can significantly affect the tag's response, the inclusion of the electromagnetic aspects and the physical environment in the chipless tag's design and the extraction of their spectral signature are a fundamental research subject that is treated in this thesis. First, the electromagnetic signature of a printed antenna with a natural fractal geometry based on a jet-fluid is studied. The design methodology for a narrow-band printed two-dimensional irregular antenna with the fractal image is also presented and the experimental characterization is discussed in terms of impedance matching, bandwidth, gain, and radiation patterns over a large frequency band. The numerical analysis performed has reported multiband resonances. This multiband behavior was investigated in order to design a chipless RFID tag with a unique electromagnetic signature. The main contribution of this thesis consists of proposing an eigenmodes technique to control the current distribution on a printed scatterer, such as a chipless RFID tag. The method based on the singular value decomposition of the Method of Moments (MoM) impedance matrix of the printed scatterer. A methodology is devised to selectively excite certain modes using multiple near-field excitations. A beamforming process is also used on receive to realize a selective sensitivity to particular modes. Specific beamforming weights are derived such that a signature can be generated for each dominant eigenmode. Simulation results are shown for different tag shapes and experimental validation is provided for a configuration exploiting just two Ultra-high-frequency

(UHF) transmitting and receiving antennas acting as a multi-ports reader. The results highlight the multiplicity of responses that can be generated with a given tag. The multiplicity of the responses from the tag provides independent signatures for the same tag, allowing the user to better distinguish the tag from others, and to improve its independence from scattering by the environment.

Finally, the eigenmodes analysis method proposed to obtain a unique signature from the tag is reformulated using another approach for the decomposition of the MoM impedance matrix. It is based on a particular inner product which involves the Gram matrix between the basis functions defined on the structure. The use of the Gram matrix allows one to minimize the effect of the tag's discretization density on the simulated results, such as the obtained surface currents orthogonality and the stability of the eigenmodes of the tag versus frequency. This methodology is used to extract the frequency responses from different tags with a variety of geometries (square, rectangle, triangle, jet-fluid, leaf shapes, and multiscatterer structure). A specialized hardware (A reader comprises of a larger array printed on a multilayered lossy dielectric material, the reader acting as a set of near-field sources.) is used to be able to control more dominant eigenmodes, which may reveal more information from the chipless tag. The proposed design of the chipless RFID tag and the eigenmode approach allow the production of very different frequency responses associated to each selective eigenmode. Responses from the tag lead to a unique signature, entailing with rich information. Also, the frequency responses from tags with a wide variety of shapes are clearly distinct and provide the easiest way to distinguish the tag in its environment. The proposed eigenmodes technique can be exploited in different applications, for example, the banknotes security applications. Indeed, the fully passive tag can be printed on a flexible substrate or embedded into an opaque substrate, which is useful for several commercial products and/or security access application.

Contents

List of Figures

List of Tables

Notations and Acronyms

Mathematical Notations

j	$\sqrt{-1}$
a	a scalar
a^*	the complex conjugate of a
$\mathrm{Re}(a)$	the real part of a
$\mathrm{Im}(a)$	the imaginary part of a
$\|a\|$	the absolute value or modulus of a
$\widetilde{a}$	the fourier transform of a
$\mathbf{a}$	a column vector
$\mathbf{a}^T$	the transpose of vector $\mathbf{a}$
$\mathbf{a}^H$	the conjugate transpose of vector $\mathbf{a}$
$\vec{a}$	a vector
$\hat{a}$	a unit vector
$\mathbf{A}$	a matrix
$\mathbf{A}^T$	the transpose of matrix $\mathbf{A}$
$\mathbf{A}^H$	the conjugate transpose of matrix $\mathbf{A}$
$\mathbf{A}^{-1}$	the inverse of matrix $\mathbf{A}$
$\mathbf{A}_{m,n}$	the m-th row and n-th column element of matrix $\mathbf{A}$
$\mathbf{I}_N$	the $N \times N$ identity matrix
$\approx$	is approximately equal to
$\ll$	is much smaller than
$\gg$	is much greater than

Acronyms

DWM	Dielectric Waveguide Model
EVD	Eigen-value Decomposition
EEM	Eigenmode Expansion Method
EFIE	Electric Field Integral Equation
FDTD	Finite Difference Time Domain
FDFD	Finite Difference frequency Domain
FEM	Finite Element Methods
FIT	Finite Integration Technique
GEP	Generalized Eigenvalue Problem
HF	High Frequency
IC	Integrated Circuit
ID	Identification
IE	Integral Equation
LF	Low Frequency
MoM	Method of Moments
MPIE	Mixed Potential Integral Equation
PEC	Perfect Electric Conductor
PCB	printed circuit boards
PTD	Physical Theory of Diffraction
RFID	Radio Frequency Identification
RWG	Rao-Wilton-Glisson
SEM	Singular Expansion Method
SVD	Singular Value Decomposition
SHF	Super High Frequency
TE	Transverse Electric
TM	Transverse Magnetic
TEM	Transverse Electromagnetic Wave
TCM	Theory of Characteristic Modes
TX/RX	Transmit/Receive
TLM	Transmission Line Method
UHF	Ultra High Frequency

Introduction

1

1.1 Overview on RFID Technology

Radio Frequency IDentification (RFID) has been emerging as a robust technology for wireless data transmission. RFID was first proposed by Stockman in 1948 [9]; it appeared as a new form of wireless communication using the antenna load modulation technique to vary the amount of reflected power. RFID technology is used to control, detect and track a variety of items using radio waves transmission methods [10]. RFID is a

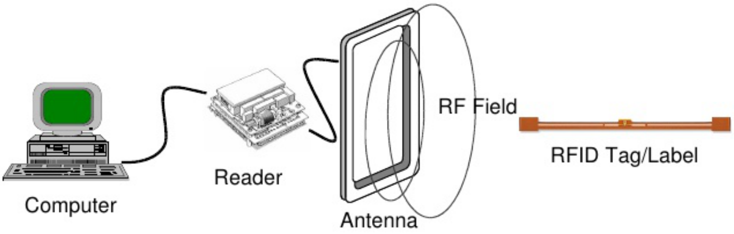

Figure 1.1: Components of RFID System [Symbol Technology].

method to automatically identify and/or authenticate an object at different distances in a short period of time using radio waves [11,12]. A typical RFID system is consisting of three important components; RFID tags, interrogators or readers, computers, and environment (Fig. 1.1).

The RFID system has been used in commercial applications since the 1970s; RFID has been applied to animal tracking, vehicle tracking and factory automation. An important RFID development was published in the paper [13] using the backscatter RFID tags technique at a frequency of 0.915 GHz. This technique is used in most RFID tags working in UHF (Ultra High Frequency) and micro-waves. The most common use of RFID technology is found in asset identification applications [12], electronic toll collection, vehicle security [12, 14], implantable biomedical devices [15], defense systems [16], and more specifically security services in the form of personal card, paper money, access control at short distance [17], and information security [10, 18].

RFID technology has recently been introduced to the consumer supply chain. Until recently, the challenge has consisted of decreasing the cost of RFID systems and developing the standards. Here, a lot of research is progressively aiming at the increase of the efficiency of RFID system and at the reduction of the supply chain costs. Those challenges of identification systems, as any other broadcasting service, involve the use of the two major parts of RFID system; RFID tag and a reader device.

The readers or interrogators are consisting of an antenna, an RF electronic module to communicate with the tag, and a control electronic module to send data to the controller. Fig. 1.2 presents the readers communication with other components of the RFID system. In operation, each reader transmits interrogation signals (with RF power, data and clock information) to the tag if it is inside the detection zone of the reader, associated with a particular environment, the energy enveloped in the emitted signal allows the operation of the tags' internal circuits. Also, the reader captures the signatures stored by the tag attached to an object. An RFID tag comprises usually two parts;

- An integrated circuit to modulate and demodulate radio signals and carry out other functions.
- An antenna to receive and transmit signals.

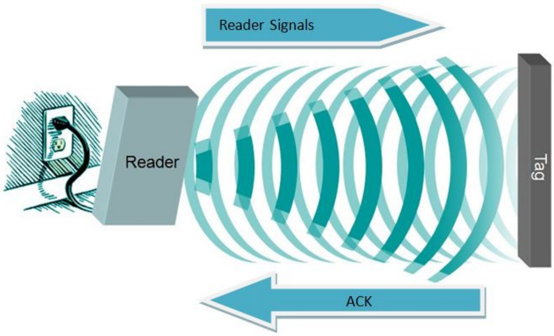

Figure 1.2: RF Components of RFID System Description [1].

The various classifications of RFID tags are based on the requirements related to performance, size, and cost [11]. Hence, we distinguish between three types of RFID tags in relation to power or energy;

- ***Active Tags***

  The active RFID tags have an on-board power source (for example, a battery; other sources of power, such as solar, are also possible). Those tags use the supplied energy to excite a micro-chip and to transmit its data to a reader. Then, an active tag does not need the reader's emitted power for data transmission. Each tag always communicates first, followed by the reader, and it can broadcast its data to its surrounding, even in the absence of a reader. Active tags have a larger radio range, which can be on the order of kilometers and communications are fast and reliable, making it ideal to locate objects or serve as landmark points [19, 20]. This comes at a high cost, thus other tag categories have been proposed.

- ***Semi-Passive (Semi-Active) Tags***

  Those tags have an on-board power source (for example, a battery), but no on-tag transmitter. Semi-passive (active) tag relies on the reader to supply its power for broadcasting. Semi-passive tags offer a longer range of readability because the used source power may allow a good functionality compared to active tags. Those tags broadcast high frequencies from about 850 to about 950 MHz, which can be read at about 30 meters (100 feet) [19] or further. These tags are less expensive to produce than the active tags, and they can be made small enough to conform to almost any product. Because these tags contain more hardware than the passive RFID tags, they are more expensive.

- ***Passive Tags***

  The third type of tags corresponds to passive tags, which do not have any on-tag power source. The tag uses the power emitted from the reader to energize itself and transmit its stored data to the reader. Using the transponder antenna, the magnetic or electromagnetic field of the reader provides all the energy required for operating the tag. With the purpose of transmitting information from the tag to the reader, the field of the reader can be modulated (e.g. through load modulation or modulated backscattering) or the energy from the field can intermediately be store by the transponder. In other words, the power emitted by the reader is used to transmit information in both ways from the reader to the tag. The communication between the tag and the reader is enabled if the tag is located inside the reader's range, when the field from the reader has sufficient intensity. Those tags have a variety of read ranges starting with less than 2.5 cm to about 9 meter. They have ranges of less than 7 meter in the ultra-high-frequency (UHF) implementation. Passive tags are smaller than active and semi-active (passive) tags, and they are more sensitive to regulatory constraints and environmental influences. Those tags have a good potential to decrease the cost. Recently, they became the cheapest and the most used tags.

As mentioned, the differences among passive, semi-passive, and active tags relate to the power source and the transmitter. All those tags contain a chip located inside an integrated circuit (IC) on the tag. Fig. 1.3 shows the classification of tags according to the frequency band, the complexity, and the cost of the tag.

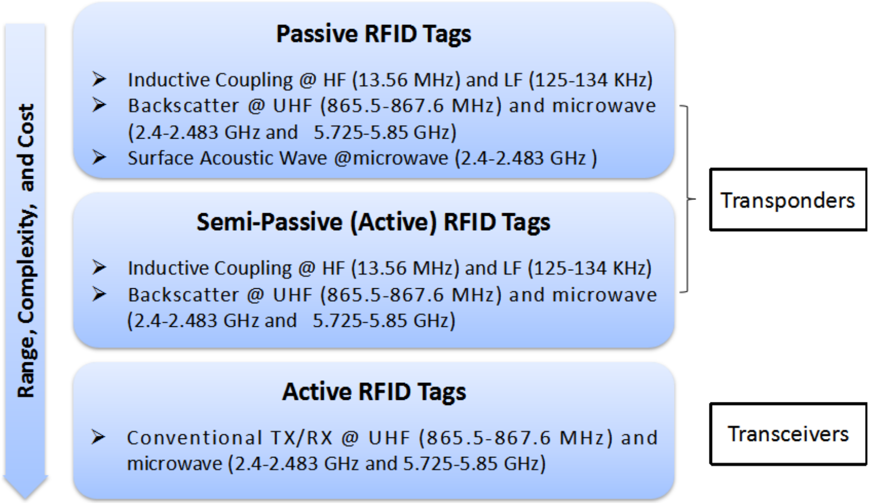

Figure 1.3: Classification of RFID Tags.

Nowadays, other RFID tags without chip are developed. Chipless RFID tags (or scatterer) have received great interest [21, 22] due to their much lower fabrication cost while their good performance is maintained. An overview of the chipless tags is presented in the next chapter.

The chipless RFID tag unit is completely passive due to the absence of an IC, while no external power supply is required [21, 23], where the tag structure can be a metallic body (scatterer) with resonant frequencies. In fact, for chipless passive RFID systems, the reader unit and the tag communicate via backscattering of electromagnetic waves [11] from the tag. It terminates to an antenna [11] which illuminates the reader area and induces currents on the scatterer. The distributed currents re-radiate the scattered fields, analyzed by the reader to decode the data transmitted from the tags. The scattering is an involved process. This phenomenon can be described in a mathematical model to study the electromagnetic behavior of the metallic tags, which is useful in the design process of chipless RFID tags.

In this thesis, the main goal is the extraction of rich information from a chipless RFID tag through its electromagnetic signature in order to minimize the falsification or counterfeiting of the passive chipless tag. In that context, we develop two methods: first, we propose a new design of chipless RFID tags based on an irregular natural fractal shape to obtain a unique electromagnetic signature for the tag. Hence, the falsification of tag content will be difficult thanks to the tag's geometry. A second method is a methodology developed to provide independent and specific signature for a scatterer using a specialized hardware: an antenna array used as a transmitter and a reader. The proposed method is based on the selective excitation of a chipless RFID tag, and its electromagnetic modes. Thereafter, unauthorized readers cannot replicate the tag's information if the tag is embedded into an opaque substrate.

Several numerical methods may exploit a mathematical model, which can represent the scattering phenomena. The precise structure of the design needs to be controlled by the designer and the use of numerical methods becomes imperative [24,25]. The most popular numerical methods that can meet this objective is described, in the next section. Nevertheless, there exist other common design strategies, particularly the methods based on eigenmode analysis techniques, which can solve this problem. Nowadays, the modeling analysis is widely used for the chipless RFID tag design. In fact, most research, along the last few years [26], uses a model approach to expand the induced currents on the tags and to provide insight in the important characteristics of the tags. The computation of modes in open or closed structures was developed more than twenty years ago. In the next section, we cover the classical model analysis methods.

1.2 Computational Methods Devoted to the Analysis of Electromagnetic Modes of Antennas

The grow of wireless communication applications has led to an increase on the research in the computational analysis area, so the challenge has been the development of the software tools to be able to characterize the electromagnetic problems in a matter of seconds. In this case, the computational tool is expected to be more appreciated in the antenna development. There are several computational tools available in the area of antenna research; each of them has advantages, but also limitations. In this sense, there still exists a need for further development in this area, as far as the electromagnetic analysis of antennas (also of metallic, printed, open/close, or loaded structures, etc) modes are concerned.

The commercial softwares (such as ansoft HFSS [27], IE3D [5], CST studio [28], etc) are actually based on some classical numerical methods such as the Finite Element Method (FEM) [29–31], the Finite-difference Time--domain Method (FDTD) [32, 33], the Finite Integration Technique (FIT) [34], the Transmission Line Method (TLM) for low frequency applications, the Geometrical Theory of Diffraction (GTD) for high frequency applications (also Physical Theory of Diffraction (PTD)), and Method of Moments (MoM) [35]. The principles of the most popular numerical methods are briefly described hereafter.

1.2.1 Brief Overview of Classical Numerical Analysis Methods

The numerical methods available to study electromagnetic structures are classified according to two axes. First, along an equation axis, differential--equation versus integral-equation. Second, along a domain axis, time--domain versus frequency domain. The Table 1.1 summarizes the classification of the numerical methods. In this section, we present the principle and characteristics of some classical numerical methods. The numerical methods can be classified according to the equation used to solve the electromagnetic problems.

- ***Differential Equation***

  Among differential equation techniques, one finds the finite difference time domain method (FDTD) [33,36] and the finite element method (FEM) [29, 30]. FDTD is a convenient tool for solving scattering and antenna radiation problems [37, 38] in time domain and frequency

	Differential Equation	Integral Equation
Time Domain	FDTD	Time Domain MoM
Frequency Domain	FEM	MoM

Table 1.1: Classification of numerical methods used in computational electromagnetics

domain, where data can be obtained over the excitation bandwidth through a Fourier transform. This method provides a major advantage. Since, the mathematical processing required for the basic analytical method is simple, the FDTD method is used to analyze complex structures in which materials may be anisotropic or inhomogeneous, as well as to time domain or frequency domain (Finite difference frequency domain (FDFD)) [39].

The FDTD method presents some limitations, such as the difficulty to analyse open structures and the need to mesh the free-space region. Using this method, it is difficult to take account the dispersive materials (where the permittivity ε and the permeability μ depend on the frequency).

As FDTD, the finite element method (FEM) is used to calculate the numerical results of radiation patterns, input impedances, polarization properties, etc. FEM is generally applied to solve both ordinary and partial differential equations in frequency domain. It is also a powerful and versatile numerical technique to handle complex geometries and inhomogeneous media. The general basic concept of the FEM [30, 31] is the subdivision of the mathematical model into disconnected components of simple geometry named finite elements. Each element presents a response which is expressed in terms of the finite value of an unknown function at a set of nodal points [40]. Then, the results of the mathematical model are approximated by connecting the collection of all elements to obtain a discrete model. The FEM has a disadvantage, common to the FDTD method, when the FEM is applied for the open structures the analyzed region has to be truncated. In general, when the FEM or the FDTD methods are applied to a given body, the whole computational volume needs to be discretized and absorbing boundary conditions around that volume are necessary to account for radiation.

- ***Integral Equation (IE)***

  This class of numerical techniques is mainly implemented in the form of method of moments (MoM) in frequency domain [35,41], although in time domain techniques are subject of intense research [42]. The MoM has been used to solve a wide variety of electromagnetic problems, scattering problems, and to analyze microstrip circuits and radiating structures. This method is based on the discretization of only surfaces (the unknowns are only defined on the interface between different homogeneous media using the surface equivalence concept). Hence, a minimum number of unknowns are needed compared to FDTD and FEM methods. MoM method leads to easy computation when dealing with open boundaries. The MoM method is usually exploited for the numerical analysis of structures made of metal or/and dielectrics. The MoM is well suited for the simulation of microstrip antennas [43, 44], for which the boundary conditions on the scatterers are carried out with the help of the electric field integral equation (EFIE) , since unknowns are defined on the metalized surfaces. The method of moments analysis of any problem involves basically three steps: first, the derivation of an appropriate IE, second the discretization of the IE into a matrix equation using basis and testing functions and its evaluation to form a matrix, and finally the solution of the matrix equations. An overview of the principle of the method of moments is presented in Chapter 3.

  In all our work, the main goal is to deal with the electromagnetic response of printed antenna arrays and scatterers on multilayer media. For this reason, we prefer to use the integral equation based on frequency domain. MoM technique is used because it is based on physical considerations. The MoM forms the basis of most commercial softwares such as IE3D Zeland [5], Ensemble from Ansoft [27], and FEKO [45].

Usually, the antennas/ RFID tags are designed by using commercial tools. As a matter of fact, the above numerical electromagnetic methods mentioned as design tools are really suitable but their major problem is that they are lacking physical insight. Recently, several research efforts giving useful ways for better antenna design took place [46]. In this context, some modal analysis methods relying on the MoM were developed for the design of antennas and to extract their electromagnetic behavior.

1.2.2 Overview of Modal Expansion Methods

Antenna design is essentially focused on wireless data transmission and radio frequency communications. The design strategies are often based on modal methods to solve the scattering phenomena [46] and obtain the induced currents on the metallic structures. The electromagnetic modeling techniques are used to obtain the desired radiation behavior of any structure geometry. Few works are raised to the physical explanation of the radiation behavior of antennas [47, 48]. The modeling analysis can satisfy this objective, as it can provide information about the modes that allow the analysis and understanding of the antenna's performance in presence of given particular excitations.

The modal analysis of structures was not just in the frequency domain in conjunction with the method of moments but also in time domain in association with the finite difference time domain [48] approach. Modal analysis methods have been developed in electromagnetics for the analysis of closed structures such as infinitely long waveguides [49,50] and cavities [47], in which it handles the electromagnetic field in closed form solutions by imposing the proper boundary conditions [51,52].

In antenna analysis, three well-known modal analysis methods have been developed for particular structures: first, the spherical mode method is proposed in 1948 [53] by Chu, and later by Harrington in 1960 [54]. The method discussed the fundamental limitations in antennas taking into account its performances in terms of bandwidth. It is based on the propagating modes within a sphere, where the antenna can be enclosed. The radiated power of the antenna can be defined from all contributed modes. Many propagating modes can be supported by large antennas. Then, the enclosing sphere should be large enough. The spherical mode method introduced by Chu and Harrington is limited to antennas with small size [47]. Second, cavity model methods had taken by Lo *et al.* in the late 70's, when trying to provide a modal analysis for microstrip antennas [55], considered as a lossy resonant cavity. To offer a simple physical insight into the resonant behavior of microstrip antennas, the cavity model takes into account the Fringe field along the perimeter of the patch, and the higher order resonant modes, as well as the feed inductance [47]. However, the application of this method is limited to the regular patch (rectangular, circular patches, etc). The patch can be printed on a single layer of a thin substrate. Finally, the dielectric waveguide model method (DWM) is also a popular modal expansion method, it has been used mainly to find the resonant frequencies of rectangular dielectric resonant antennas [56]. The modal analysis of other than rectangular dielectric resonant antennas can be developed using other engineering formulas [57] or full wave simulations [47].

The modal analysis methods describe above provide clear physical insights into the resonant behavior and radiation performance of antennas. Another general modal analysis method is developed for solving a wider variety of antenna problems. In the 70's, another modal analysis theory named theory of characteristic modes (TCM) was developed as a versatile modal analysis tool for conducting bodies with arbitrary geometries and metallic antennas [46]. The analysis and design of an antenna using the TCM give information about: the resonant frequency of any mode, the modal radiation fields in the far field range, and the modal currents on the surface of a structure.

The TCM was proposed for the first time by Garbacz in 1965 [58], while the characteristic modes (CMs) were not well defined yet. CMs correspond to the eigen-vectors of a weighted eigen-value equation [58]. In the early seventies, Garbacz and Turpin [59] have introduced the complete TCM and the development of the computation of CMs. Garbacz and Turpin define the CMs as a set of surface currents and radiated fields that characterize the obstacle, which are independent from external excitation [60]. Those CMs lead to a particular orthogonal set of modes in the development of any induced current on the surface of the obstacle. The far-fields associated with the orthogonal currents have the useful orthogonal properties over the source region and the radiation sphere at infinity. Harrington and Mautz reformulated the TCM in 1971 based on the operator in the electric field integral equation (EFIE) on the conducting body [61, 62]. This operator relates the current to the tangential electric field on the object. To reproduce the same modes as defined by Garbacz and Turpin, Harrington and Mautz propose to diagonalise the operator and to choose a special weighted eigen-value equation. The TCM formulation described by Harrington leads to a simpler derivation of the TCM proposed by Garbacz and it is applicable to perfectly electrically conducting (PEC) bodies of arbitrary geometry. Afterwards, this formulation is extended by Harrington *et al.* to enclose dielectric, magnetic, and both dielectric and magnetic objects [63]. Recently, the CMs formulation and computation are primarily used considering the approach of Harrington. Over the last five years, several new investigations on these CM formulations have been developed for the modal analysis of patch antennas printed on multilayered dielectric media, of dielectric bodies [64–66], and of dielectric resonator antennas [67]. The mathematical formulation of TCM is detailed in Chapter 3.

The TCM has been extensively validated through several platform antenna designs [47], such as electrically small antennas where some publications were focused on this subject. As presented in [47], after the year 1980 it exists 10% of publications on CM-based electrically small antenna designs from all publications on the CM-based antenna research topics. The electrically small antennas include the radio frequency identification (RFID) tag antenna. In the last few years, some publications were focused on modal analysis of the RFID tag antenna in ultra-high frequency based on TCM [26, 68, 69].

In light of this research topic, a modal analysis method is proposed in this thesis, to determine the dominant and higher order modes of currents excited on passive chipless RFID tags using a simple eigenmodes techniques. The chipless RFID tags with different geometries are printed on a lossy dielectric substrate backed by a ground plane. The proposed method is based on the method of moments (MoM) and the singular value decomposition (SVD).

1.3 Goal of the Thesis

The objective of this dissertation is to add insights from an electromagnetic point of view into information security issues in RFID systems, leading to the electromagnetic analysis of passive chipless RFID tags using a new modal technique.

Chipless passive tags are currently proposed for radio frequency identification of an object because chipless tags are suppose the cheapest, since they do not have a chip and no modulation impressed the backscattered signal. Each chipless tag is associated to signatures resulting from the tag's geometry. The signature can be retrieved from the reader to identify or authenticate a given tag. This leads to two important challenges: First, the discrimination of the response of the tag with regards to that of the environment. Second, the extraction of sufficiently rich information from the tag, as it relies entirely on the tag's shape (characterized by a unique signature). This work strives to contribute to those tasks. Within this framework, the goal of this thesis is to propose a new way to solve those challenges. This work is divided into three principal parts.

In a first part, a printed antenna design based on two-dimensional natural fractal shape is presented. The experimental results in terms of antenna performances over a wide frequency band allow a unique electromagnetic response of the antenna. The proposed structure can be used as a chipless RFID tag, which is characterized by a special signature.

In a second part, a numerical method is proposed to excite specifics modes on the tag using an array as a reader. The excited modes contribute to strengthen the response of the tag and to enrich it through multiple responses. The main purpose of this part of the work is the analysis of the responses of chipless passive RFID tags over the super-high-frequency

(SHF) range using a novel eigenmode approach for near-field RFID applications. This eigenmode analysis method is based on the singular value decomposition. The eigenmode method is used to exploit specific frequency responses of the tag which can be printed on a thin lossy dielectric substrate backed by a ground plane. In this work, the eigenmodes in a frequency band are efficiently computed using a self-developed numerical code based on the method of moments and not the commercial electromagnetic simulators IE3D, FEKO, CST, or HFSS because the latter do not provide access to the MoM impedance matrix of the chipless RFID tag.

The proposed eigenmodes method is leading to independent signatures for a tag thanks to the multiplicity of frequency responses resulting from the tag's shape using the developed eigenmode analysis technique and a reader consists of multiple antennas. The proposed method allows one to improve the separation of the tag's signature from scattering by the environment. Hence, the passive chipless tag can be easily distinct from other scatterers present in the environment.

Finally, in order to exploit more specific responses and to distinguish the tags from each other, an extension of the proposed eigenmode method is presented through a reformulation of the methodology and the use of tags with complex geometries, which provided a unique electromagnetic signature for the tag.

1.4 Structure of the Thesis

The novelty and importance of the contributions for this doctoral work will progress with the chapters. Starting from Chapter 2, an antenna design is proposed with a structure based on an irregular fractal geometry. The structure presents an important electromagnetic response, which allows one to design a chipless RFID tag with the proposed natural fractal geometry. After that in Chapter 4, the eigenmodes technique based on the SVD decomposition can be taken as a first approach to extract the frequency responses of a chipless RFID tag. Ending in Chapter 5, the eigenmodes method based on an alternative decomposition to SVD for printed tags with different geometries can be considered as the most important contribution.

1.4.1 Chapter 2: Design of Chipless RFID Tags Based on Natural Geometry

The second chapter presents the field of passive chipless RFID systems from its developments to its applications. It also introduces an experimental study of a chipless RFID tag design. An antenna printed on a lossy dielectric substrate backed by a ground plane is proposed with a structure based on natural fractal geometry (jet fluid image). A numerical analysis of the printed antenna on a dielectric substrate has carried out using the commercial software HFSS on a wide frequency band (from 1 to 20 GHz). An experimental characterization of the antenna (gain, radiation pattern, resonant frequency, etc) has been presented over the band 1-20 GHz. A unique electromagnetic response is extracted from the antenna. The specificity of the frequency response obtained from the proposed antenna allows the use of this structure as a chipless RFID tag, where it can be used for the security application. The work presented in Chapter 2 has been published in [18].

1.4.2 Chapter 3: Modal Analysis Techniques of scatterers

The main focus, in the third chapter, is given on the Modal analysis of metallic plate object and printed scatterer on a lossy dielectric substrate. This chapter proposes three analytical techniques to exploit the current distribution induced on the structure according to a set of eigenmodes. The results obtained using the proposed modal techniques are compared to those obtained through the theory of characteristic modes (TCM) reformulated by Harrington built around a generalized eigen-value problem (GEP). All those methods are usually based on the Method of Moments (MoM) generalized impedance matrix. First, the principle of MoM method is given, and the MoM technique for multilayered media is discussed. Later, the mathematical formulation of the TCM is briefly presented. After that, eigenmodes techniques are proposed based on the eigen-value and eigenvector decomposition (EVD) and the SVD to exploit the total current on the scatterer. The validation of the proposed techniques is presented through a comparison of the total current distribution induced on the structures determined directly through the MoM, the TCM, and the other proposed techniques. Also the convergences of modes are studied for different structure using the TCM and the proposed eigenmodes techniques. The EVD--eigenmode, and the SVD-eigenmode approaches are the novel contributions in this chapter. The work related to the eigenmode technique based on the EVD decomposition presented in this chapter has been published in [70].

1.4.3 Chapter 4: Selective Excitation of Chipless Passive RFID Tag using SVD-Eigenmode Approach

In chapter 4, an eigenmode technique is proposed to control the current distribution on a printed chipless RFID tag. The method relies on the SVD decomposition of the method of moments (MoM) impedance matrix of the printed tag. A new methodology is devised for selectively excite certain modes on the tag using multiple near-field excitations. Besides, a near-field beamforming process on receive is also used to realize a selective sensitivity to specific modes. Then, specific beamforming weights are derived such that a signature can be generated for each dominant eigenmode on the tag. The simulated results obtained from the implemented code and from the commercial software IE3D are compared for different tags. Experimental validation is provided for a configuration exploiting just two antennas as transmitters and receivers and a tag with square geometry. The antenna array is printed on a multilayered dielectric material acting as near-field sources. The array is considered as a reader to transmit power to the tag and to receive the tag's information. The goal of the eigenmode approach is the exploitation of eigenmodes that may elevate that signal above the background response, while providing a highly characteristic signature that can be generated with a tag.

1.4.4 Chapter 5: Extended SVD-Eigenmode Approach for Selective Excitation of Scatterers with Complex Structures

Chapter 5 is divided in to the following main parts: First, the SVD-eigenmode method proposed in Chapter 4 is extended to solve the problem related to the influence of the scatterer's discretization on the simulated results, such as the obtained responses from the chipless tags. This means that the modes on the structure could be stable with changing the mesh of the given structure. In this context, the reformulation of the eigenmodes technique employs the Gram matrix [71] to give a new definition of the eigenmodes of the scatterer based on a new scalar product. This product able to better represents the interaction between physical current distributions. The modified eigenmodes approach is proposed to obtain richer responses from the tag and to minimize the effect of the discritization density of the metallic scatterer.

The challenge of most of the modal analysis method is to be able to match modes between adjacent frequencies, in other words the modes on any structure are unstable versus frequency and they do not appear in a good order at each frequency [72,73]. This problem is presented in Chapter 4 while the extended eigenmodes method has led to more or less the stability of the modes versus the frequency. Second, the eigenmodes approach based on a new scalar product is extended through the use of a larger number of transmitting and receiving antennas considering as a reader. This extension allows the selection of other wanted eigenmodes and to enrich the information for the tag, as well as using different shapes for the scatterer such as irregular fractal geometries.

1.4.5 Chapter 6: Conclusion and Future Works

Chapter 6 summarizes the important findings and outcomes of this thesis project and highlights the key aspects of the work. A brief review of each chapter is also discussed in conclusion. This chapter suggests some future research lines.

Design of Chipless RFID Tags Based on Natural Fractal Geometry

2

2.1 Introduction

Radio frequency identification (RFID) system is comprised of three principle components: antenna, reader, and chipless tag or transponder. As mentioned in Chapter 1, a RFID tag can be active, semi-passive (active) or passive. Those RFID tags have many potential applications in several fields, boosted by their low cost. The challenge of all RFID tags' development is to reduce the tag cost. Recently, chipless RFID tags have been considered as a solution of the cost problem while affirming good performances as the electromagnetic behaviors. This chapter presents main types of chipless RFID tags, and their operation principles. The chapter is divided in two parts. A brief state of the art clearly highlights the design process developed in chipless RFID tags and its importance in several applications. In the other hand, an example of chipless RFID tag design is proposed to secure the system by considering a special chipless tag with an irregular fractal (see Appendix A) shape inspired from the geometry of a liquid jet [74]. The experimental investigation of the antenna performances over a frequency band extending from 1 to 20 GHz illustrates a specific electromagnetic response of a printed antenna based on the natural complex image. Therefore, the proposed patch can be used as a chipless RFID tag for security applications with reference to complex and unique signature of the tag, where the signature is difficult to be replicated by an unauthorized reader.

2.2 Chipless RFID Technique

The chipless RFID technique is a recent research area, which has emerged in 2002 [75]. However, the basic concept was developed half a century ago with one of all first RFID system designed by Léon Theremin in 1945. The RFID systems introduced in Chapter 1 can seem very different from each other. In all cases, we find the two important elements, the transponder and the reader but the difference is related to the RFID tag component i.e. the electronic chip connected to an antenna. Chipless RFID systems use the electromagnetic properties of materials and design various conductor shapes to attain specific electromagnetic performance. The overall system of a chipless RFID tag is shown in Fig. 2.1.

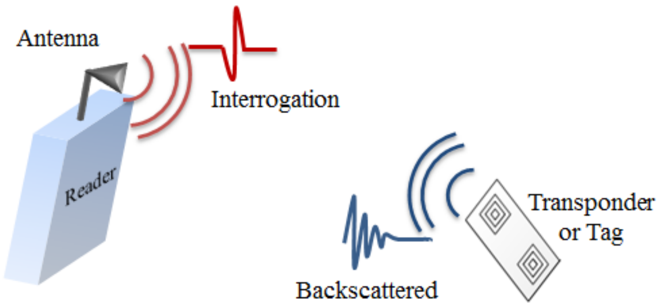

Figure 2.1: Chipless RFID system including the reader and the chipless tag.

2.2.1 Chipless Transponder Characteristics

Chipless RFID tag is the name of the passive RFID tag that does not use a semiconductor chip [76]. The tag (transponder) does not contain any integrated circuit technology to store information. The chipless RFID tag is a passive reflector of a signal emitted by the RFID interrogator. The tags can use plastic or conductive polymers, or materials such as conductors that reflect back a portion of the radio waves beamed at them [77,78], the unique return signal can be used to encode information which is implemented in the reflected electromagnetic radiation. Most chipless RFID systems use the electromagnetic properties of materials and design various conductor shapes to achieve particular electromagnetic behavior. There are different types of chipless tags described in the literature: the main groups of chipless RFID tags are presented in Fig. 2.2.

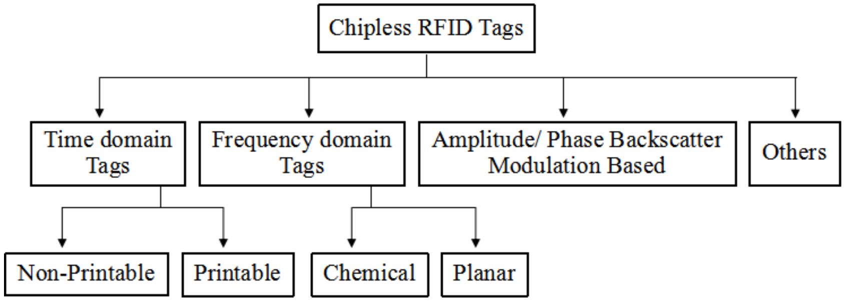

Figure 2.2: Classification of groups of chipless RFID tags.

2.2.1.1 Time Domain Reflectometry (TDR)

TDR-based chipless RFID tags are interrogated by sending a signal from the reader in the form of a pulse and listening to the echoes from the pulse. A train of pulses is thereby created by tag, which can be used to encode data. There are two family of chipless RFID tag operating on the principle of TDR:

- **Non-Printable**

  A surface acoustic wave (SAW) tag is a TDR-based chipless tag. It is developed by RFSAW Inc. [75]. SAW tags could well replace chipped tags, they do not provide a printable solution due to their piezoelectric nature, which cannot be printed on papers/plastic based items such as banknotes. The SAW tag is created by one or multiple reflectors and an antenna allows the transformation of the radio frequency waves to acoustic waves. The radio frequency waves are transmitted by the reader and they are converted into SAWs using an interdigital transducer (IDT). The SAW is reflected by the used reflectors, which create a train of pulses with phase shifts [79–83]. Those pulses are converted back to an electromagnetic (EM) waves using the IDT. The EM waves are detected at the reader, where the tag's response is decoded [84–86]. However, the cost of the SAW tag is almost the same as the one of commercial RFID. This is due to the fabrication tolerance of the order of the micrometre (μm) [76] and also of the requirement of the piezoelectric substrate with Interdigital Transducers. The concept of the RFID SAW tags is presented by Fig. 2.3.

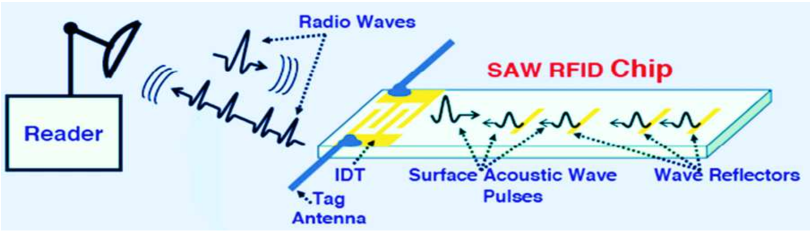

Figure 2.3: Architecture of the chipless RFID SAW System [2].

- **Printable**

  A TDR-based chipless tag can be printable and it has been described in [87,88]. These tags translate data using multiple precisely delayed back-scattered pulses of the interrogation signal using multiple capacitive loadings at particular points of the microstrip line. Printable chipless tags can be found either as Thin-Film-Transistor Circuits

(TFTC) or microstrip-based tags with discontinuities. TFTC tags are printed at high speed on low cost plastic film. TFTC tags offer advantages over active and passive chip-based tags due to their small size and low power consumption. Each data encoded by this tag needs a delay line, then the size of the tag increases. Fully printable chipless RFID tags can use spectral signature encoding based on space filling curves [89] and capacitive tuned dipoles [90].

The printable chipless tag is a reproduction of the SAW tag using microstrip technology in time domain. The experiments on these chipless techniques have been reported, where limited data have been successfully encoded.

2.2.1.2 Spectral Signature

Spectral signature-based chipless tags encrypt information into the spectrum by means of resonant structures. Each data is usually associated with the peak of the resonant frequency at a predetermined frequency in the original spectrum. Then, the interrogator extracts the data on the tag structure by detecting the resonances of the tag frequency signature [91–93]. The advantages of this family of tags are: the scatterer is fully printable and the data storage capability is higher compared to other chipless tags. Yet, a large spectrum is needed for data encoding and wideband dedicated on the reader side. In the literature, two types of spectral signature tags based on the nature of the tag can be distinguished: chemical and planar circuit.

- **Chemical**

  These chipless tags are designed from a deposition of resonating fibers or special electronic ink. These tags consist of tiny particles of chemicals which exhibit varying degrees of magnetism. Also, the electromagnetic waves impinge on the tag which resonates at distinct frequencies [94]. We find as chemical chipless tag: ink-tattoo chipless RFID developed by Somark Innovations [95] and nanometric material based [96]. They are very cheap and can easily be used inside banknotes and important documents. These tags are not expensive and can work on low grade paper and plastic packaging material. So, they only operate at some kHz frequencies, although this gives them very good tolerances to metal and water.

- **Planar circuit chipless RFID Tag**

  They are designed using planar microstrip/co-planar waveguide or strip line resonant structures such as antennas, filters, and fractal structure. They are printed on thick, thin and flexible substrates [3]. Reported frequency domain based tags can be grouped into two categories: multi-resonator based tags which comprise transmitting and receiving antennas and multi-resonating circuit. In most of the reported tag developments, the latter consist [97–100] of narrow-band circuits using different microwave resonators. These resonators are either connected or coupled to microwave transmission line and both ends of the transmission line are connected to two UWB antennas. The other category is the multi-scatterer based on tags which consist of scatterers resonators with different dimensions. Each resonator can work as a receiving antenna, a filter, and a retransmitting antenna. Hence the effect of the UWB antennas and transmission line dimension can be eliminated and these tags present better bit encoding capacity than multi-resonator based tags. The electromagnetic response of the muti-resonator based tag can be achieved with a structure using multiple signals giving out scatterers [101–105]. Usually, the scatterer receives an interrogation signal from the reader and reflects back to the reader. At resonance, it generates a different EM signature. In the already described groups of chipless tags, there is still a novel research of other type of chipless tag as the amplitude/ phase backscatter modulation based chipless tags, where the data encoding is achieved by changing the amplitude of the phase of the backscattered signal by the variation of the antenna loading of the tag [106]. Others approach are reported to the design of the chipless tag and obtain better signature of the tag. Chipless RFID tags can be used in many different environments than RFID tags with electronic circuits. Many researches about the chipless RFID designs are based on the frequency domain. Then, to create specific resonances on the frequency domain of the interrogation signal, there are different types of approaches, which are presented in the next sections with the important recent development of this type of tags.

2.2.2 Development of Design Chipless RFID Tags

The previous section has presented different family of chipless RFID tag that allows a comparison among the principle chipless RFID techniques. Most of those techniques are still in research to meet the expectations of current and future major applications. Most of the applications require a good chipless RFID system design with very interesting performances such as:

– The cost (the cost of the tag), where the chipless RFID tag considers the cheaper one. This places the limits on the tag design and the choice of materials for construction. The interesting conductors that can be used are copper, aluminum and conductive ink, and the dielectrics are polyester and printed circuit boards (PCB) substrates.

– The dimension of the tag is dependent on the desired frequency and the size of the tagged item.

– The required bandwidth and memory capacity.

– The read range and management of collisions.

– The security is the most important performance require by any applications.

Hence, the choice of a tag and the process design of a chipless RFID system is determined by the application (with specifications and challenges) for which it will be deployed.

Chipless RFID tags have been envisaged for various types of applications such as automatic identification, conveyor belt control [97], liquid-bearing [19,107], and security systems [108]. Recently, the chipless tags are usually used in security applications because they have been considered as a good solution to reduce the tag cost while maintaining good performance [21,109]. Due to the absence of its integrated circuit (IC), the chipless tag is completely passive, low cost, robust, and does not require a power supply [110].

Among various design techniques used for chipless tags, based on time [111, 112], frequency [113, 114], phase [115], and image [116]. The frequency domain technique provides an important data capacity for chipless RFID tags [117] based on the backscattered magnitudes responses versus frequency. A chipless RFID system can provide an extra layer of security against counterfeiting when using transparent conductor. A tag may be printed without being visible. The security of the applications can be achieved from the frequency signatures of the chipless tag which allow the specification of the tag. In this context, a design of chipless RFID tag is proposed, in the next section, to determine a unique signature of the tag, and a modal analysis method is proposed, in chapter 4, to obtain multiple frequency responses of the tag.

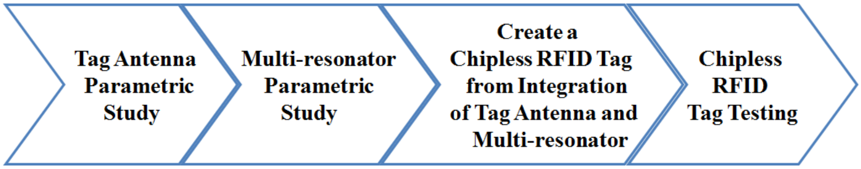

Figure 2.4: Chipless RFID tags process [3].

The process design chipless RFID tags have four steps [3] as shown in Fig. 2.4. Each tag design technique consists of the designing of the tag antenna and the achieving of the necessary antenna parameters; return loss bandwidth and radiation pattern. Using the tag antenna design, the resonators (Multi-resonator based tags defined before) are designed and optimized. Then, the optimized tag antenna and the multi-resonating circuit are combined to obtain a chip less RFID tag. The last step of process design tag is the theoretical verification by testing the resulted tag in a wireless experimental setup to verify its robustness [3]. Recently, most of the design chipless RFID methods are based on printed tag and frequencies beyond the S-band (above 2 GHz) [97, 118, 119]. In a same way, the goal of the recent research is to obtain better properties of the chipless RFID tag as the resonance (signature of the tag), the radiation characteristics of the tag, and the increase the performances of the tag.

In the following section, the design of the tag antenna, multi-resonator and integrated tag is presented. The proposed tag antenna is a printed antenna on dielectric substrate backed by a ground plane with a complex natural shape.

2.3 Design of Chipless RFID Tag Based on Irregular Fractal Geometry

The fractal concept [120] has impacted many areas of science and engineering. In telecommunications, the fractal approach (see Appendix A for fractal geometries' definition) was applied to antennas [121, 122]. It has produced innovative structures with miniature shape, multiband and/or wideband behaviors, and good radiation properties [123–125]. The study of antennas with complex fractal geometry still remains limited. Recently, some publications are focused in this area: the electrochemistry technique was applied to obtain two-dimensional (2D) [126–128] and three-dimensional (3D) irregular fractal antennas [129, 130] characterized by multiband and wideband behaviors which may permit their use in wireless multi-frequency and broadband telecommunications.

The 2D and 3D-antennas were proposed for UWB applications, and for concealment and detection, respectively. In [131–133] a fractal jet-fluid was investigated for the design of a 2D irregular fractal printed antenna based on a real image of the jet. The antenna showed also a multiband behavior useful for multi-frequency wireless applications. A 2D pseudo random aggregation model was applied also to generate clusters used in the design of an irregular fractal printed antenna for ultra-wide band radio systems [134]. In the same context, fractal geometries were used for design of

RFID systems thanks to good performances of fractal antennas [135–137]. All research presented in this field are based on fractal deterministic (see Appendix A). Here, a printed fractal antenna based on natural complex shape translates to a variety of design opportunities for chipless RFID tag.

2.3.1 Design of Complex shape-Antennas

The natural image used in the present work is obtained with a liquid jet issuing from an injector [131, 132]. Details on the process to obtain the image were given in [74, 138]. In Appendix A, a brief explanation of the steps used to obtain the natural fractal image is given. Fig. 2.5. (a) shows the image of the liquid jet-fluid. After implementation of image analyzing tools, the shadow of the continuous jet-fluid is produced which gives the irregular fractal image (Fig. 2.5. (b)) used for design of 2D printed irregular-patch antenna.

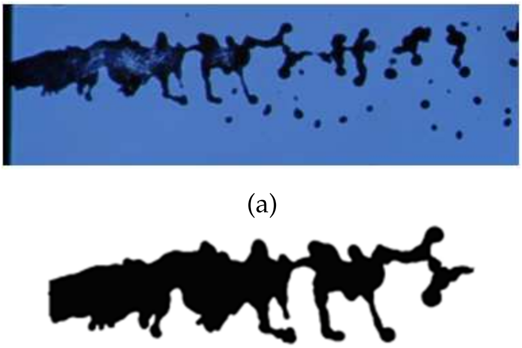

(a)

(b)

Figure 2.5: Image of the jet of heptane issuing from a triple-disk injector; (a) initial image and (b) shadow of the continuous jet.

2.3.1.1 Antenna conception

In a microstrip antenna field, the edges of the radiating patch are a key parameter to analyze its radiation behavior. As a printed antenna, we have investigated a structure with high irregular patch boundary as the printed--jet antenna. To simulate a printed antenna based on this types of geometries under the the simulator software HFSS [27], we first detected the contour of the jet image by using a developed Matlab [139] code, which defines the boundary of this shape (Fig. 2.6. (a)). A VBS (Visual Basic Script) macro

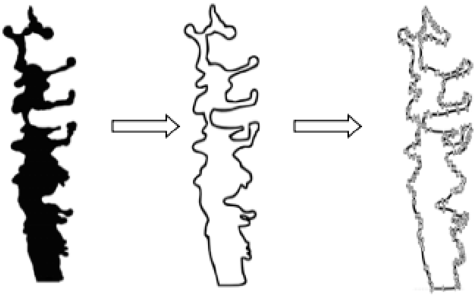

(a)

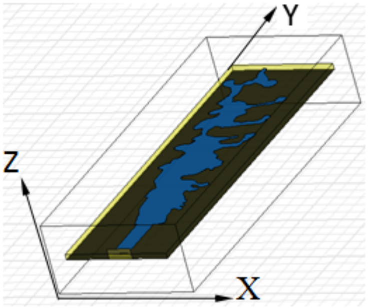

(b)

Figure 2.6: Design Antenna processing: (a) Contour detection using developed code, (b) 3D-Model of the printed irregular-fractal antenna with software HFSS.

was second implemented to import the boundaries of the fractal jet geometry and to reproduce the fractal patch under the simulator HFSS. Finaly, the 3D-model of resulting printed antenna under HFSS is created and it is presented in Fig. 2.6. (b).

Next, the tag antenna was designed and realized by considering the fractal image obtained in the above section which is the shadow of the continuous jet (see Fig. 2.5. (b)). A fractal patch of maximum length L_p= 4.2 cm and width W_p= 1.2 cm was printed on a Duroïd substrate of thickness 0.08 cm and permittivity 2.17 (Fig. 2.7) whereas a microstrip of length L_f= 0.8 cm, width W_f= 0.245 cm and impedance Z_0 = 50 Ω was used as a feed--line. The length L_p and width W_p of the radiating patch are defined as the dimensions of the smallest rectangle containing the fractal image. The feed-line is situated at the distance X= 0.25 cm from the inferior edge of the rectangle $L_p \times W_p$. The bottom face of the substrate was metalized and acts as a ground plane. Fig. 2.7. (b) shows the realized prototype with a substrate of dimensions L_s= 5.1 cm and W_s= 1.5 cm.

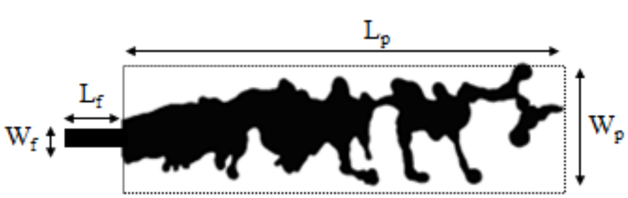

(a)

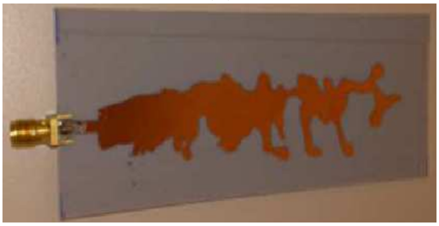

(b)

Figure 2.7: The proposed fractal-patch antenna: (a) fluid-jet image and feed-line, (b) prototype of the realized antenna.

Finally, the tag antenna was studied numerically and experimentally by determining all the resonant frequencies and their associated radiation properties.

2.3.1.2 Frequency Signature's Principle

One main application of frequency-domain-based chipless RFID tags is security where the electromagnetic signature technique is used to protect confidential data in RFID systems from unauthorized readers. The concept of frequency signature is based on the interrogation of the RFID tag with a multi-frequency signal and the distinction of attenuated frequencies (represented by logic ″0″) from non-attenuated frequencies (represented by logic ″1″) [92, 118]. The variation of the amplitude and/or phase of the signal sent back to the reader determines the nature of the logic state ″0″ or ″1″. Therefore, by encoding N-bit digital word with N attenuated frequen-

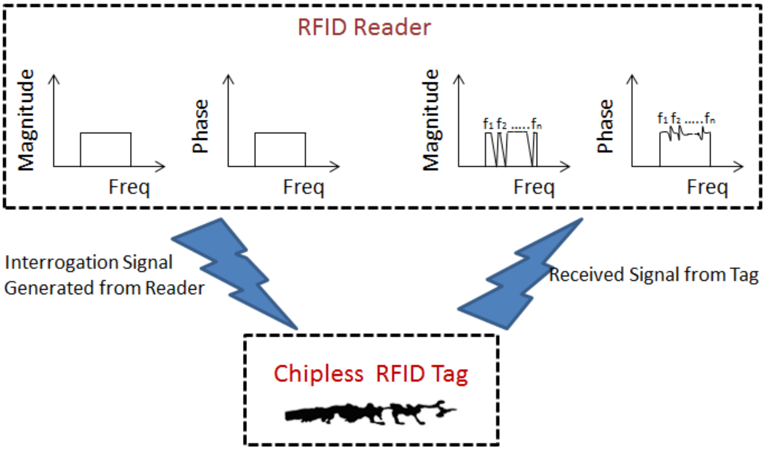

Figure 2.8: Operating principle of the proposed chipless RFID tag based on the electromagnetic signature of an irregular fractal-jet printed antenna.

cies, where each bit represents a single frequency, we can create a unique frequency signature associated to the tag. Fig. 2.8 shows the proposed operating principle of the frequency signature-based chipless RFID tag. The frequency signature represents then the total response of the fractal-tag characterized by a set of amplitude attenuations and phase jumps at all the resonant frequencies of the fractal antenna, which generates a unique code (tag ID) directly depending on the shape of the fractal patch. The proposed chipless tag based on the irregular-fractal geometry of the fluid jet, may then be an adequate solution for the security of confidential data in RFID systems due to its complex and unique electromagnetic signature.

2.3.2 Experimental Characterization

To illustrate the particular electromagnetic response of the fractal antenna, we have characterized its experimental performances in terms of impedance matching over the frequency band [1-20] GHz, and gain and radiation patterns at frequencies 3.478, 4.858, and 5.256 GHz. Fig. 2.9 and Fig. 2.10 illustrate the impedance matching behavior of the fractal antenna over the band [1-20] GHz; Fig. 2.9 illustrates both measured and simulated magnitudes of the return loss, and Fig. 2.10 shows the measured phase. We can notice from Fig. 2.9 a good agreement between simulation and measurements. For better analysis of the antenna impedance bandwidth behavior versus the frequency, the magnitude and the phase evolutions have been presented in Fig. 2.11 and Fig. 2.12, respectively, over the frequency bands L, S, C, X, and Ku covering the range from 1 to 18 GHz. Table 2.1 resumes measured impedance matching results that can be deduced from Fig. 2.11 and Fig. 2.12.

In Table 2.1, we have reported the main resonant frequencies (only for $|S_{11}| < 10$ dB) of the antenna and their associated values of $|S_{11}|$ in the explored frequency range [1-20] GHz. We can note that the irregular fractal patch is characterized by a high multi-frequency behavior, which is confirmed in Fig. 2.11 and Fig. 2.12, by the existence of multiple dips in the magnitude and jumps in phase, of the return loss. Table 2.1 resumes also the main results dealing with the resonant frequencies, their impedance bandwidth, and their possible number of encoded bits for both the magnitude and the phase of the return loss in all the sub-bands L, S, C, X, and Ku of the frequency range [1-18] GHz.

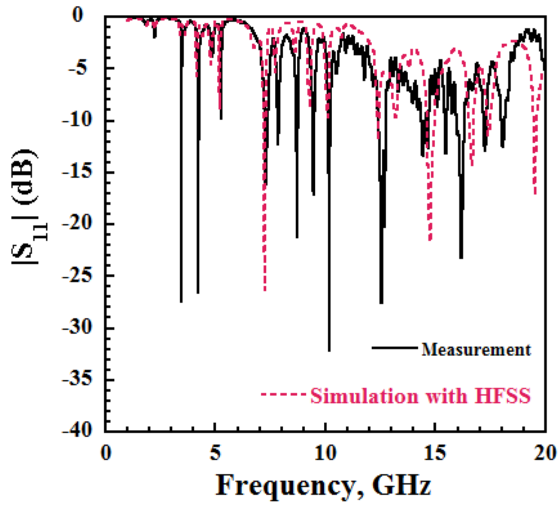

Figure 2.9: Evolution of the irregular fractal-jet antenna reflexion coefficient over the frequency band [1-20] GHz.

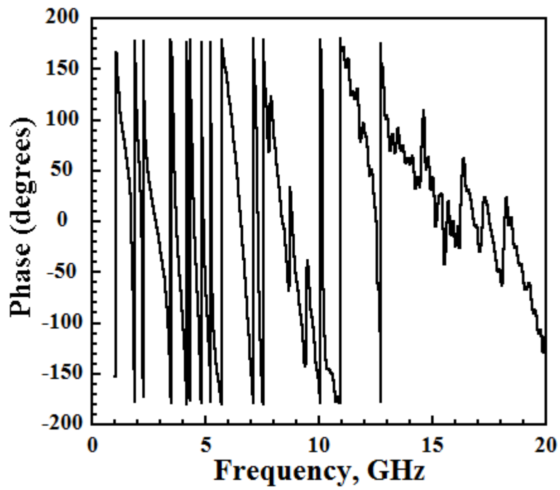

Figure 2.10: Evolution of the irregular fractal-jet antenna measured phase over the frequency band [1-20] GHz.

Following the analysis of the obtained results from Fig. 2.10 and Fig. 2.11

Table 2.1: Measured results ($\mid S_{11} \mid <$ -10 dB) deduced from Fig. 2.11

F_n, GHz	3.47	4.22	5.25	7.28	7.84	8.7	9.45	10.16	12.54	14.42	14.66	15.47	16.18	17.25
$\mid S_{11} \mid$, dB	-27.4	-26.6	-10	-16.1	-12.3	-21.2	-17.1	-32.1	-27.5	-13.4	-12.6	-13.1	-23.2	-12.9
Bandwidth, MHz	10	15	0	135	57	74	80	95	347	177	98	88	363	141
Bands	L and S	C				X			Ku					
Nb of encoded data from S_{11}	1 bit	4 bits				3 bits			6 bits					
Nb of encoded data from Phase	5 bit	8 bits				7 bits			11 bits					

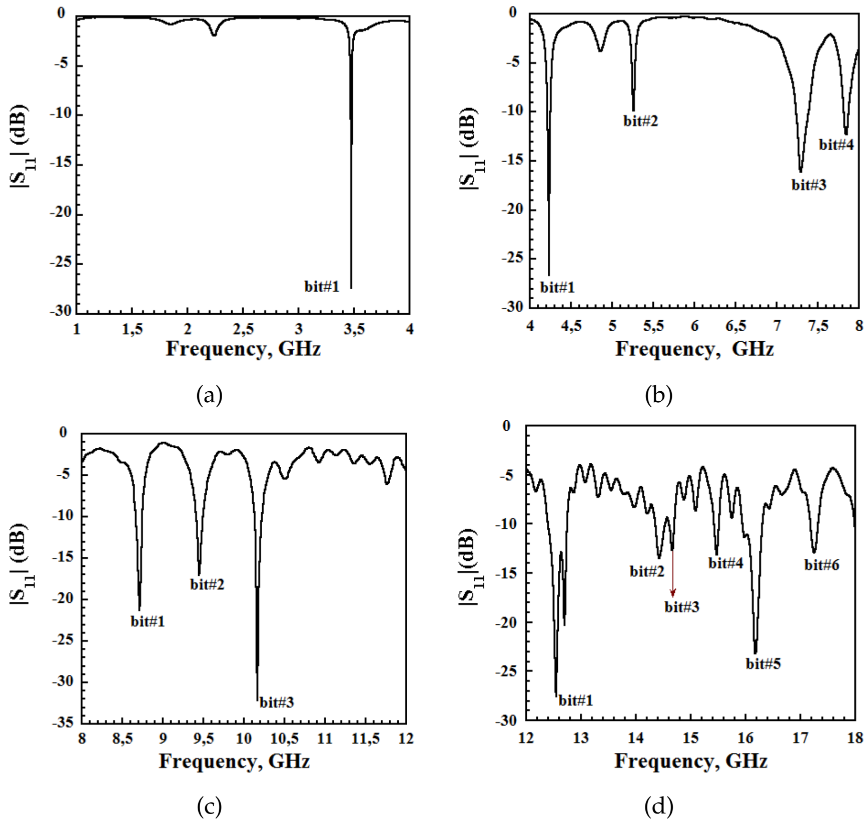

Figure 2.11: Evolution of the measured antenna return loss magnitude over the frequency range [1-18] GHz: (a) L and S bands; (b) C-band; (c) X-band; (d) Ku-band.

and Table 2.1, we can deduce that:

- The fractal structure is characterized by a unique distribution of narrowband resonances.
- We can encode data from the magnitude or the phase of the antenna return loss due to these resonances, where the amplitude attenuation and the phase ripple at one particular frequency represent the logic state ″0″ otherwise we have the logic state ″1″ (no attenuation and no phase ripple).

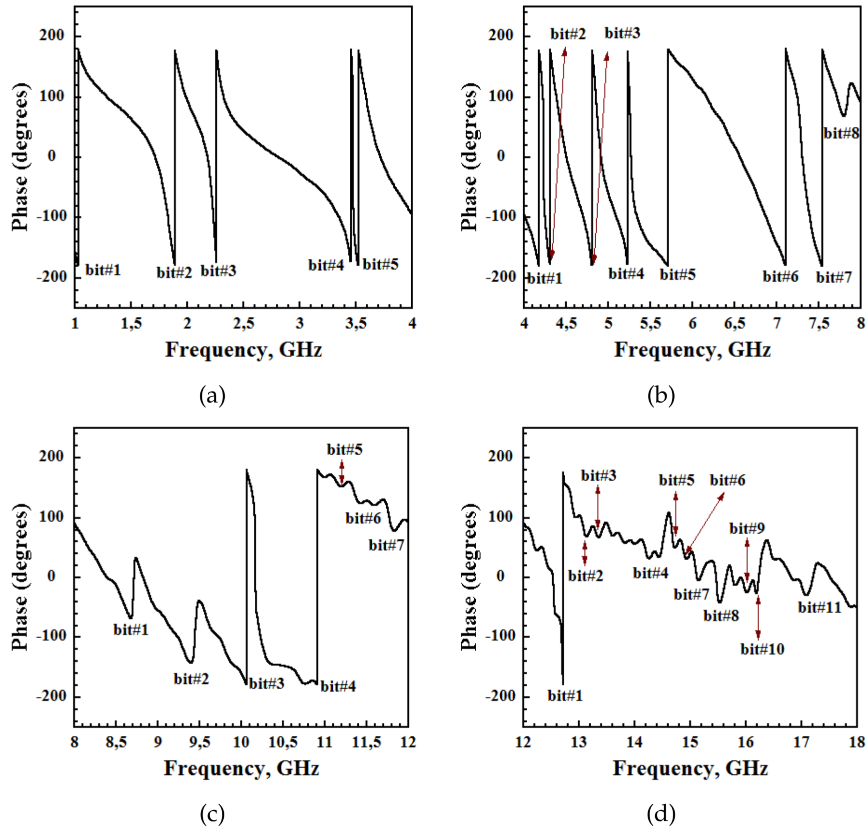

Figure 2.12: Evolution of the measured antenna return loss phase over the frequency range [1-18] GHz: (a) L and S bands; (b) C-band; (c) X-band; (d) Ku-band.

– The capacity of encoded data depends on the considered technique for encoding data (amplitude or phase), and the frequency band. This capacity seems to be better for the phase at the lower frequency sub-bands L, S, C, and X, and for module at higher Sub-band Ku. For example, we can encode 8-bit digital word due to the fact that there are eight phase jumps over the C-band (Fig. 2.12. (b)), and 6-bit digital word due to the fact that there are six resonances over the Ku-band (Fig. 2.11. (d)).

– The chipless transponder based on the fractal jet antenna can encode, over the total band [1-20] GHz, 14 and 31-bit digital words using the amplitude and phase encoding techniques, respectively. We estimate that these properties are sufficient to prove the successful and adequate proposition of this tag to encode data for security application.

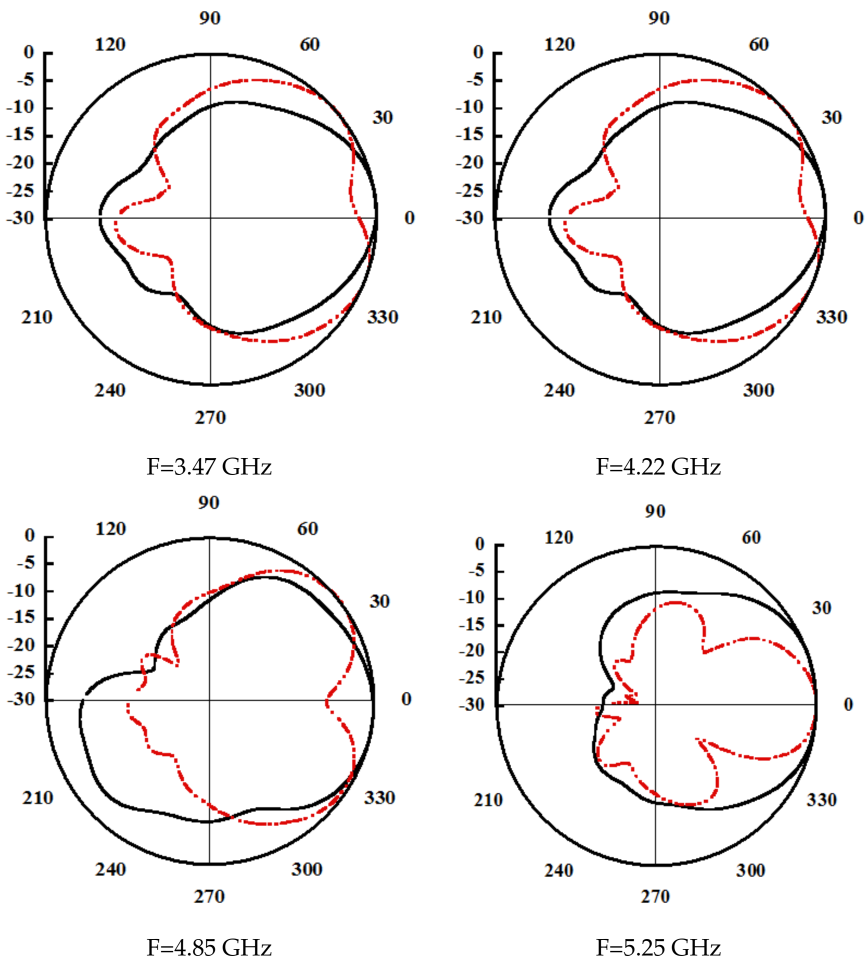

Figure 2.13: Measured radiation patterns at resonating frequencies 3.47, 4.22, 4.85 and 5.25 GHz in E-plane (- - -) and H- plane (——).

As the anechoic room (SATMO) used at the IETR-INSA institute covers the frequency range from 1 to 6 GHz, the radiation patterns were measured only at frequencies 3.47, 4.22, 4.85, and 5.25 GHz. The highest measured value of the gain was 7 dB at the frequency 4.22 GHz. Fig. 2.13 shows the 2D-measured radiation patterns in both E-plane (yoz) and H-plane (xoz) at resonant frequencies 3.47, 4.22, 4.85, and 5.25 GHz. We can remark that these patterns are smooth (no ripples and few dips) and without secondary lobes, especially for the H-plane.

The tags with fractal irregular geometries can provide a specific electromagnetic signature thanks to the irregular geometry of the patch boundary and size, which confirms the previous result reported in [127, 131, 132] for this type of structures.

The proposed fractal antenna can be applied for the design of two types of printable chipless frequency signature-based RFID tags: retransmission--based tags and backscattering or radar cross section (RCS)−based tags. Fig. 2.14 shows the proposed prototype of the retransmission-based tag. In fact, the fractal tag (Fig. 2.14. (b)) is composed with a receiving UWB antenna (Fig. 2.14. (a)) and the fractal patch (Fig. 2.7. (b)). The parameters design of the UWB antenna and its impedance matching properties over the frequency band [1-12] GHz are reported in [140].

The retransmission-based tag [89,90,99] can use an UWB/SWB antenna to receive and then retransmit the interrogation signal from the fractal antenna as shown in Fig. 2.14. (b). When the RFID tag, composed of both the UWB-antenna and the fractal jet antenna, is illuminated with a wideband signal, first the UWB antenna receives this signal, and then the irregular fractal antenna resonates at only some frequencies, then the multi--frequency signal is retransmitted back to the reader. Finally, the reader converts the spectral signature of the tag into a series of binary data bits (ones and zeros). Cross-polarized horn antennas with a reflective shield may be used. For this technique, the tag is usually large in size (because it contains both the emitting and receiving antennas), requires a metallic ground plane, and its reading procedure is highly dependent on the angular orientation of the tags.

(a) (b)

Figure 2.14: Prototypes of proposed retransmission based RFID fractal-tag.

Therefore, by using the proposed fractal-antenna we may improve the tag performances as the antenna presents many resonance frequencies, large ground plane, and may be compacted by using just a scale law for the fractal patch without much reducing the number of resonances.

The backscattering-based tags which use the fractal patch for both receiving and then retransmitting the signal should be relatively more compact in size compared to the retransmission based tag, described previously. The proposed tag may produce a unique RCS signature characterized directly by the complex and irregular shape of the resonating patch.

Recently, many types of chipless RCS-based tags were studied and some limitations of their use were reported [141–144]. In [110], a chipless tag based on capacitively tuned dipoles was designed but size of the resonating elements and also strong mutual coupling between them restrict the data encoding capacity of the tag. Chipless RCS based on space filling curves and compact resonators were also investigated but these tags require a significant layout modification for bit encoding [142]. Whereas chipless RCS based on slot resonators [143] and split ring resonators [144] have shown a very short reading range.

The proposed fractal patch may also improve the performance of the RCS-based tag because it employs a simple compact fractal patch without resonating elements, slots or split resonators. Which may avoid the drawbacks cited above, and increase data encoding capacity and reading range of the tag.

2.4 Conclusion

In this chapter, the brief chipless RFID concept to understand the chipless RFID technology with a brief literature overview has been presented. The differences between groups of chipless RFID tags, which are several and varied as the conventional RFID, are discussed. As mention in this chapter, the chipless RFID technology has become quite widespread in several applications because of the development of tag design, which imposes different lower level challenges such as: low cost of chip less tags, small size, and good tag performance.

In this chapter we proposed a design of a chipless RFID tag antenna with complex shape. The structure is based on a natural fractal image obtained from a liquid jet-fluid injector. The electromagnetic response of the printed antenna based on this natural geometry has been studied. First, we have designed and simulated the antenna by using the commercial software Ansoft-HFSS. The numerical analysis of the tag antenna has revealed mainly multi-resonances for the structure. This multiband behavior was investigated in order to design a chipless RFID tag with a unique electromagnetic signature. The proposed tag can be used in different services such as security access control. Also, it can be applied to secure chipless RFID systems, especially by combining the proposed design technique with invisible tags that can be embedded into packaging, paper or film. Other techniques were used to analyze the electromagnetic signatures of chipless RFID tags based on numerical analysis methods. Modal analysis is one of them, and different modal techniques can be used to study the electromagnetic phenomena. A modal analysis method and other proposed modal techniques are discussed in next chapter. In this context, a new modal analysis method, based on a special eigenmodes set on the tag through a mathematic formulation, is proposed in this doctoral thesis. The proposed eigenmode approach is allowing the user to obtain specific frequency responses from a chipless tag, and those responses provide independent signatures of the tag.

Modal Analysis Techniques of Scatterers

3

3.1 Introduction

During the last decade, the rise of chipless RFID applications has led to risen significant interest in antenna design and especially on design processes for chipless RFID systems for security applications. Most of those works use classical numerical methods using the commercial software to study the electromagnetic behavior of the scatterer. Other analysis methods provide more thorough physical insight to explain the working mechanism of chipless tags:

- **Singular expansion method (SEM)** [26] is a method which provides the exploitation of the induced currents on the scatterer versus the frequency domain poles of the scatterer. SEM was introduced by Carl Baum [145], it was developed to describe the general behavior of an object's response illuminated by an electromagnetic wave. The SEM was widely used in the radar domain and studied for target identification [146,147] from the information present on the poles. From this information the global shape and the constitution of the excited target can be described. In antenna engineering the SEM was used, for example, to model the time response of the current of a wire antenna

[148]. Recently, the SEM has been applied in time and frequency domains to analyze the characteristics of an antenna (antenna radiation patterns, directivity and gain) using residues [149–151] associate with some poles. Also, this method was used later in identifying and designing chipless RFID tags [152, 153]. SEM has a known limitation, related to poles extraction being very sensitive to noise [151] and it can be used in time domain.

- **Eigenmodes expansion method (EEM)** [26] is a method which allows expanding the currents from the scatterer using the eigenmodes of the structure. The induced currents on the scatterer can be easily expanded versus the eigenmodes of the dyadic Green's function [154] of the structure in the frequency domain. The EEM has been provided to find the eigenmodes, eigen-values and the complex natural resonances of the scatterer. The theory of characteristic mode (TCM) induces a weighted eigen-value equation for arbitrary shapes; its implementation is easier than SEM based on its mathematical formulation to obtain the current distribution on the scatterer surface. The modes on the scatterer are obtained as specific eigenmodes of an impedance matrix, which is calculated using the famous numerical method, method of moments (MoM). The TCM will be discussed in further detail in Section 3.3.1.

Other methods are proposed in this chapter based on the eigenmodes on a scatterer to exhibit the resonance frequency of the structure under consideration, the induced current on the tag by the antenna, and the physical explanation of the radiation of the scatterer. The eigenmodes can be found from an eigen-value equation commanding the structure. In this chapter, we first summarize the theory of characteristic modes (TCM) and also we derive other eigenmode analysis methods to expand the induced current of the scatterer. Finally, a comparison between the TCM, the proposed methods and the direct calculations based on the MoM are present. Next Section will be an overview of the Method of Moment technique. This class of method is explained for a printed structure on a dielectric substrate and backed by a ground plane. We consider metallic patches printed on the infinite dielectric substrates backed by an infinite ground plane. In the same section, the results obtained with the developed MoM code for multilayer medium case is validated using results obtained with the commercial software IE3D. The same code will be used throughout the manuscript to compute the MoM impedance matrix. In Section 3.3.1, a general overview of the mathematical formulation of TCM is recalled to represent the current on a scatterer in terms of eigenmodes of the same metallic structure. On the other hand, we propose other eigenmode techniques based on the eigen--value decomposition (EVD) or on the SVD decomposition of the MoM impedance matrix to generate the current induced on a scatterer. In the last section, a comparison between the illustrated methods will be discussed using a scatterer. It is already studied in literature using TCM. This validation is based on the resulting induced current distribution on the scatterer versus their eigenmodes.

3.2 The Method of Moments

The conventional method to subtract the eigenmodes has been in conjunction with the Method of Moments (MoM) formulation [35, 155] in the frequency domain. The MoM technique is a very robust numerical method for solving the currents induced on the metallization of structures printed on multilayered dielectric media, it is the focus of several new studies [156, 157]. The MoM is used to solve Maxwell's equations in the Integral--Equations (IE) form [41], which is mainly implemented in frequency domain, though time-domain methods are also of interest [42].

A fundamental principle of the MoM technique [35, 158, 159] is used to convert integral equations into a linear system of equations that can be solved numerically using a computer [160–162]. A general overview of the MoM formulation [35, 163] is given in the next section.

3.2.1 Principle of the Method of Moments

In this section, we describe the MoM implemented in an in-house code developed at UCL to simulate finite metallic structures printed on a layered [164] and multilayered infinite dielectric substrate backed by an infinite ground plane. The developed code based on the Method Moment will be used to determine the electromagnetic behavior (resonant frequency, impedance and admittance matrices, a mutual coupling, and $\cdots$) of various printed structures throughout the thesis.

The MoM is a linear algebra technique to approximate the solution of linear operator equations, which have the common form

$$L(x) = v \tag{3.1}$$

where x is an unknown function to be determined (field or response), the linear operator L is the integral-differential type, and v is the forcing known function (source or excitation). Irrespective of the approach, the operator equation (3.1) can be solved following the numerical procedure known under MoM. This requires that the function x can be expanded as a linear combination of N known basis functions $x_n(n = 1, 2, \cdots, N)$, given from

$$x = \sum_{n=1}^{N} i_n x_n \tag{3.2}$$

where i_n is an unknown coefficient associated to each x_n. Using linearity of L and inserting this combination into (3.1), the linear equation can be reduced to

$$\sum_{n=1}^{N} i_n L(x_n) \approx v \tag{3.3}$$

where the basis function x_n are used to model the expected behavior of the unknown function over its domain of L. Then, the step remaining to solve (3.3) is to find the N unknown constants i_n $(n = 1, 2, \cdots, N)$. This can be accomplished by having N linear independent equations from evaluate (3.3). It is known that the MoM equations are basically comprised of boundary conditions for tangential fields, at N different points. Those conditions allow to provide an inner product $\langle f_t, v\rangle$, where f_t is a weighting function named testing function [35]. To choose these testing functions; the point matching way can used where the tangential fields are enforced at N points on the surface of an object [40]. Hence, any solution is very sensitive to those points and the convergence of the MoM not be optimal [40]. However, other way can be better in the choice of the testing functions where the set of testing functions and basis functions is similar. This important way is referred to the Galerkin approach [35, 163] , and allows to obtain symmetric system and linear algebraically equations. Throughout the domain of the linear operator L, N testing functions are defined. Hence, the inner product of each f_t with the residual function equal to zero, then it written as:

$$\sum_{n=1}^{N} i_n \langle f_{t_n}, L(x_n) \rangle = \langle f_t, v \rangle \tag{3.4}$$

We can present (3.4) in $N \times N$ linear matrix equation

$$\mathbf{Z}I = V \tag{3.5}$$

where $\mathbf{Z}$ is a matrix of size $N \times N$ obtained from the inner product of the testing functions with $L(x_n)$, I represents the vector of unknown coefficients i_n, and V equal to the inner product of f_t and source function v. Then, by solving (3.5), the coefficients i_n can be found using matrix inversion techniques as

$$I = \mathbf{Z}^{-1}V \tag{3.6}$$

The following section introduces the popular basis functions in MoM. The basis functions illustrated below are used in this work to expand the surface current of structures.

3.2.2 Basis Functions

Each numerical solution of electromagnetic problem is based on the choice of the basis functions x_n. The basis functions were originally proposed in [165]. We can find many possible sets of basis functions in the literatures [166–168]: (i) the local or elementary functions which are nonzero only in a part of the domain function (it can be the surface of the structure). (ii) the global domain basis functions which exist over the entire domain of the functions. The famous elementary local basis functions in the MoM, which will be used in this work, are referred to as

- **The Rao-Wilton-Glisson (RWG)** elements on triangles [169]. It is the very usually used basis functions. Fig. 3.1 illustrates the RWG basis functions which contain a pair of triangles. RWG basis functions is firstly used to solve the electromagnetic scattering problems of arbitrary shape in [169], later to generalize inhomogeneous dielectric mediums by [170]. Using RWG method, the vector current distribution inside the triangle element can be extract from the linear superposition of unit currents along the three sides of the triangle.

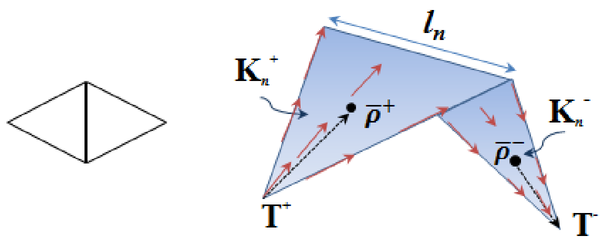

Figure 3.1: RWG Basis functions defined on the triangular mesh.

- **Rooftop basis functions** [171, 172] can be a good choice to discretize the simple objects like as rectangular type structure. The rooftop basis functions in X and Y-directions are depicted in Fig. 3.2,

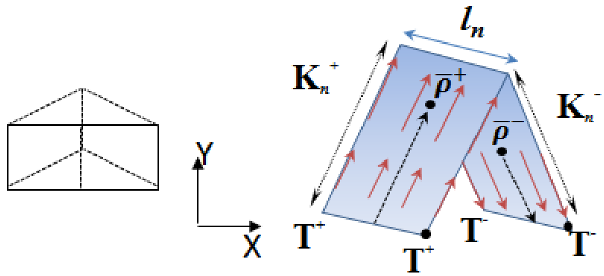

Figure 3.2: Geometry of a rooftop basis function.

In the examples given for this manuscript, unless otherwise stated, we will generally use the Rao-Wilton-Glisson (RWG) basis functions which are very useful for arbitrary structures. The source excitation (the port of an antenna) is introduced from one aggregate rooftop basis function. The discretization of structures is carried out with the help of the GMSH software [4, 173].

3.2.3 MoM Impedance Matrix for Scatterer

As announced in the previous sections, to apply the MoM to solve equation (3.1), four steps are needed:

– Derivation of the appropriate integral equation (IE),
– Discretization process to obtain a matrix equation (3.5) using basis functions and testing functions. In the developed code, we used Galerkin testing functions; i.e. the set of testing functions corresponds to the set of basis functions.
– Evaluation of the matrix elements.
– Solving the matrix equation and obtaining the parameters of interest.

In this work, we will use MoM approach based on IE, hence the boundary conditions mentioned in Section 3.2.1 for a pure metal object (scatterer) are enforced with electric field integral equation (EFIE) [174]. The surface current density $\bar{J}$ (for electric current distribution case) on the surface S of a structure (see Fig. 3.3) is defined as follows, using equation (3.2).

$$\bar{J} = \sum_{n=1}^{N} i_n \bar{f}_{b_n} \tag{3.7}$$

where the known basis functions are named here $\bar{f}_b$ and i_n is the unknown coefficient to be determined. As mentioned before, while we applied the Galerkin testing to EFIE, the linear MoM matrix equation (3.5) is obtained and its solution leads to the unknown coefficients i_n, and then the surface current on the surface of a structure. The elements of the MoM impedance

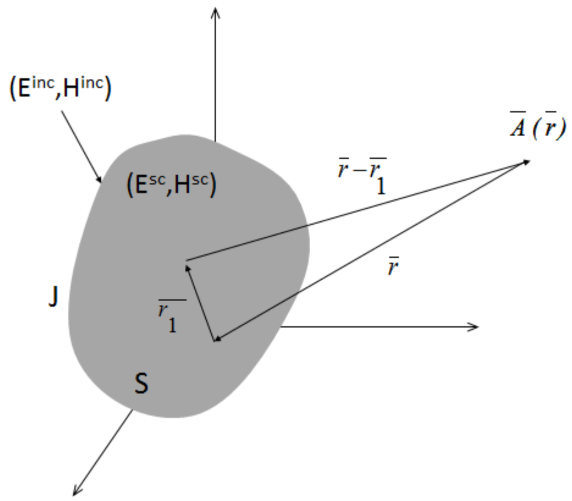

Figure 3.3: Geometry Scattering Problem and observation coordinate.

matrix **Z** in (3.5) represent the interaction between the source elementary basis function ($\bar{f}_b$) and testing functions ($\bar{f}_t$). In the absence of normal components of the basis and testing functions on the edge of a domain S_1 and other S, an element of **Z** is written as [175, 176] :

$$\begin{aligned} Z_{t,b} &= -\int_S \int_{S_1} [\, j\omega\, \mu\, \bar{f}_t\,(\bar{r}) \cdot \bar{f}_b\,(\bar{r}_1) \\ &\quad + \frac{1}{j\omega\, \epsilon} \nabla \cdot \bar{f}_t\,(\bar{r})\, \nabla_1 \cdot \bar{f}_b\,(\bar{r}_1)\,]\, G(\bar{r},\bar{r}_1)\, dS_1\, dS \end{aligned} \tag{3.8}$$

where ω is the angular frequency, and ε and μ are the permittivity and permeability of the host medium, respectively. The factor $G(\bar{r},\bar{r}_1)$ is the Green's function of free space and it expressed as

$$G(\bar{r},\bar{r}_1) = \frac{e^{jk|\bar{r}-\bar{r}_1|}}{4\,\pi|\bar{r}-\bar{r}_1|} \tag{3.9}$$

where k is the wavenumber, $\bar{r}$ is the vector relies to observation point (domain S), and $\bar{r}_1$ is the vector presents the source point (domain S_1).

Thereafter, it is steal to define the elements in the excitation vector V to determine the unknown coefficients i_n and surface current density. Those elements v_n are defined as

$$v_n = -\int\int_{S_1} \bar{f}_{b_n}(\bar{r}_1) \cdot \bar{E}^{inc}\, dS_1 \tag{3.10}$$

where $\bar{E}^{inc}$ is the incident fields vector, which can be plane wave, fields product by an antenna or a generator.

A very large number of electromagnetic problems, especially antenna problems, treated with the MoM are treated in the literature. In this chapter and next chapters, we studied printed structures on dielectric substrate. During the last few decades, several developed techniques for the analysis of printed antennas or metal printed on materials with different shapes have remained as an interesting subject of many researches. Actually, many commercial software are used in the analysis and design of planar metal printed structure and printed antennas such as Mentor Graphics' IE3D [5], Feko [45] and others based on a Mixed-Potential Integral Equation (MPIE) formulation and MoM [43, 174, 176–179]. The application of this technique leads to limited discretization to the metallization surfaces using the appropriate Green's functions [176].

3.2.4 MoM for Printed Structures, Multilayer Media

The method of moments solution of the IE has received high attention for electromagnetic modeling of microstrip structures (printed structures on layer medium). As introduced in previous section, the MoM entails the evaluation of the Green's functions and the appropriate choice basis functions, to obtain an accurate and efficient solution. The microstrip structures design become more complicated to analyze, such as the structures printed on multilayer substrate with different shapes. Multilayered media may be modelled with special Green's functions [180] devoted to the analysis the structure printed on a multiple lossy dielectric substrate. In this case, the formulation of the Green's function is tailored for 2D infinite substrate with finite thickness to handle each layer of the lossy dielectric material, and the discretization of the structure is located in the metallic surfaces not the dielectric substrates themselves. Based on this technique, the elements of

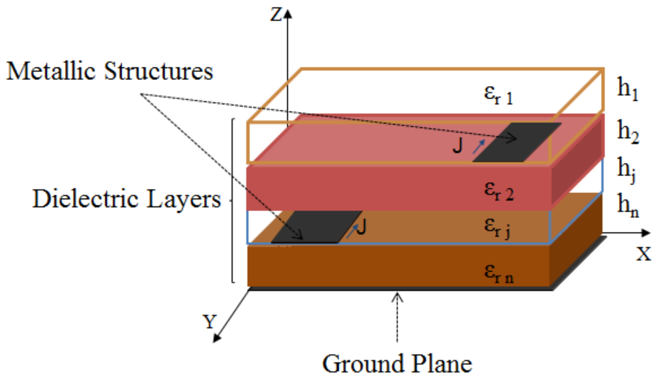

Figure 3.4: A multilayer medium with source and observation points in different layer.

the MoM matrix, which are defined in (3.8) for an object in free space, are written as [180] in the multiple layer case (see Fig. 3.4).

$$\begin{aligned} Z_{t,b} &= j\omega \iint_S \iint_{S_1} [\bar{f}_t(\bar{r}) \cdot \bar{f}_b(\bar{r}_1)\, G_a(|\bar{r}-\bar{r}_1|) \\ &\quad - \frac{1}{\omega^2} \nabla \cdot \bar{f}_t(\bar{r})\, \nabla_1 \cdot \bar{f}_b(\bar{r}_1)\, G_q(|\bar{r}-\bar{r}_1|)]\, dS_1\, dS \qquad (3.11) \end{aligned}$$

where G_a and G_q correspond to the two different scalar potentials. The scalar potentials $G_a(|\bar{r}-\bar{r}_1|)$ and $G_q(|\bar{r}-\bar{r}_1|)$ for current/charges can be written in space domain as [178, 179]

$$G_a(|\bar{r}-\bar{r}'|) = G_a(R) = G_a^{ext}(R) + G_a^{hom}(R) \qquad (3.12)$$

$$G_q(|\bar{r}-\bar{r}'|) = G_q(R) = G_q^{ext}(R) + G_q^{hom}(R) \qquad (3.13)$$

where G_a^{hom} and G_q^{hom} correspond to potentials computed in an effective homogeneous medium, with average relative permittivity of two media $(\epsilon_r^{av} = (\epsilon_{r_1} + \epsilon_{r_2})/2)$ [179], and substrate thickness h_n named medium n and other substrate layer above the metallic structure named medium j (see Fig. 3.4). The potentials G_a^{hom} and G_q^{hom} were defined as [164, 179]

$$G_a^{hom} = -\frac{k_0\, \eta_0}{2\, k_z^{hom}} \qquad (3.14)$$

$$G_q^{hom} = \frac{\eta_0}{k_0} \frac{1}{2\, \epsilon_r^{av}\, k_z^{hom}} \qquad (3.15)$$

for given free-space wavenumber k_0, wavenumber in homogeneous medium k_z^{hom} and wave impedance η_0.

The potentials G_a^{ext} and G_q^{ext} are provided in a one-dimensional table, where the average homogeneous medium component has been extracted, in order to get rid of the $1/R$ type singularity. G_a and G_q are tabulated versus horizontal distance R [179]. Then, the element of the MoM impedance matrix can be rewritten for the multiple layered substrate case as the sum of the contributions from the effective homogenous medium and the layered medium [164, 179]

$$\mathbf{Z} = \mathbf{Z}^{hom} + \mathbf{Z}^{ext} \tag{3.16}$$

where $\mathbf{Z}$ denotes the multiple layered medium case in the implemented lab's code, and $\mathbf{Z}^{hom}$ is the effective homogeneous medium impedance matrix where their elements are computed through the homogeneous Green's function which is obtained as follows using the code developed in the laboratory [164]

$$\begin{aligned} Z^{hom} \quad &= \quad \frac{1}{j\omega\epsilon}\int_S\int_{S_1} \left[(k^{hom})^2 \bar{f}_t(\bar{r}) \cdot \bar{f}_b(\bar{r}_1) - \left(\nabla \cdot \bar{f}_t(\bar{r})\right)\left(\nabla' \cdot \bar{f}_b(\bar{r}_1)\right)\right] \\ &\qquad G^{hom}(|\bar{r} - \bar{r}_1|)\, dS_1\, dS \end{aligned} \tag{3.17}$$

with

$$G^{hom}(R) = \frac{e^{-ik^{hom}R}}{4\pi R} \tag{3.18}$$

$\mathbf{Z}^{ext}$ is the layered medium matrix where their elements can be obtained from equation (3.11) by using the simple Green's function potentials G_a^{ext} and G_q^{ext} with extraction of the effective homogeneous medium.

More details on the MoM technique for the multilayered lossless medium case used to implement the code developed at the lab were discussed and provided on Shambhu's thesis [164], where the mathematic formulation provide the details on the Green's function for multilayered media are inspired from an internal note [179] and research carried out mainly in the nineteen [60, 177].

In this thesis, the lab code was modified to simulate printed structures on multilayered lossy dielectric substrates with dielectric constant ε and electric loss tangent *tanδ*. The simulated results carry out, in this chapter or the later ones, using the modified lab code with important number of integer and interpolation points, and a factor value of the deformed contour height equal to 0.005. The deformed contour is a contour integation parameter of parabolic type with a positive constant factor [181]. This factor should be less than 0.01 to produce smooth numerical results.

If a printed array is formed by different elements placed at chosen positions and printed in different layers, the MoM system of linear equations to be solve can be written as

$$\mathbf{Z}I = E_x \qquad \text{then} \qquad I = \mathbf{Z}^{-1}E_x \tag{3.19}$$

where $\mathbf{Z}$ is the MoM matrix consisting of sub-matrices presented the interactions between all structures printed in different dielectric layers. I is the vector of current coefficients to be solved in the array, and E_x consists of all excitation sources on the whole structure, a definition of the excitation source is explained below.

The results obtained after solving the system of equations were used to perform modal analyses of some printed structures. As presented in the next section, there are several methods termed as modal analysis approaches. They each provide a different physical insight into the resonant behavior of structures. In Section 3.3, we used the in-house MoM code to solve the system equations (3.19) and to carry out modal analyzis. First, we validate the implemented MoM code for a multiple lossy dielectric substrate with a comparison of the simulated results to those carried out using the IE3D software [5]. Later, the results obtained using the theory of characteristic modes (TCM) were compared with existing results in the literature. In the same section, we proposed other modal techniques in terms of eigenmodes analysis.

- **Excitation Source**

  The excitation vector can correspond to plane waves, fields radiated by another antenna or fields impressed by a generator. To simplify the analysis, we will use the delta-gap generator [163,164,175]. Here and in the following work, the excitation source used to compute the

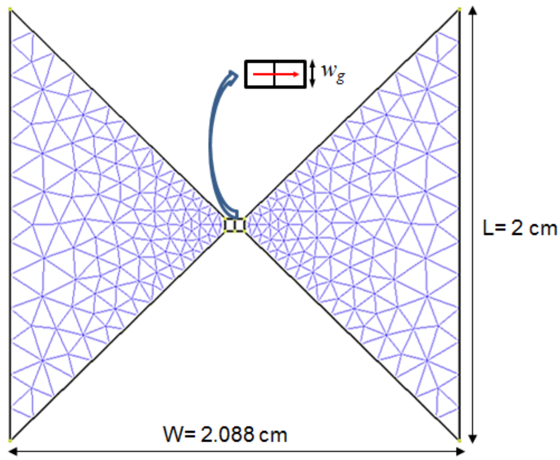

Figure 3.5: Discretized printed bowtie antenna considered for later result using the GMSH software [4]. The antenna is meshed with 599 RWG basis functions, one rooftop basis function for the delta-gap source, and two hybrid basis functions.

current coefficients using MoM techniques for the results hereafter are based on a delta-gap generator with a 50 Ω source impedance. The delta-gap generator is a source represented by a voltage discontinuity between two infinitely close conductors. In a delta-gap source, the feed is treated as if the impressed electric fields (E_x) existed only in the gap. Mathematically, the delta-gap source model can be calculated as:

$$E_x = -w_g V_0 \tag{3.20}$$

where w_g is the width of the gap and V_0 is the voltage applied to the gap. For all numerical simulation presented in this thesis, the source (delta-gap) is meshed by one rooftop basis function (see Fig. 3.5), and then the excitation vector has non-zero values only for the corresponding basis function.

- **Validation of the Multiple layered medium code** In this section, an initial validation of the implemented MoM code is described through a numerical simulations, which have been carried out for an array

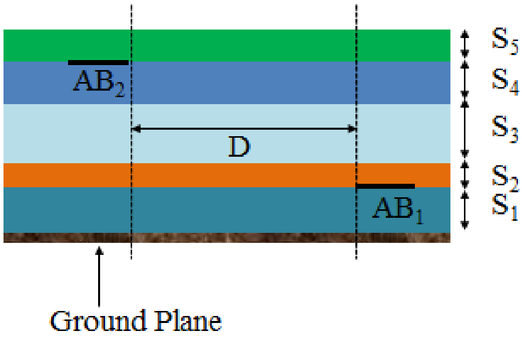

(a)

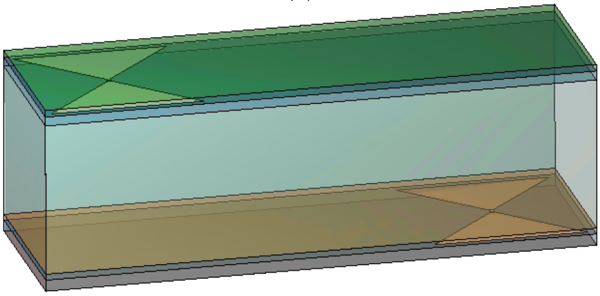

(b)

Figure 3.6: (a) Array for printed bowtie antenna (AB_1 and AB_2) on multiple dielectric substrates; S_1: FR4 ($\varepsilon_r = 4.3, \Delta\delta = 0.02$), S_2: duroid ($\varepsilon_r = 2.2, \Delta\delta = 0.0009$), S_3: air ($\varepsilon_r = 1$), S_4: rogers RO4003 ($\varepsilon_r = 3.55, \Delta\delta = 0.0027$), and S_5: duroid ($\varepsilon_r = 2.2, \Delta\delta = 0.0009$). (b) 3D-view of the array generated with commercial software IE3D [5]. The structure is terminated by a ground plane.

consisting of bowtie antennas (see Fig. 3.5) printed on different positions and dielectric layers. The array backed by a ground plane is presented in Fig. 3.6. The first bowtie antenna (AB_1) is printed between two dielectric substrates S_1 of substrate height $h_1 = 0.15$ cm and S_2 with thickness $h_2 = 0.0787$ cm. The second bowtie antenna (AB_2) is printed also between two dielectric substrates S_4 of thickness $h_4 = 0.12$ cm and S_5 of height $h_5 = 0.09$ cm , the relative permittivity and the loss tangent of every dielectric substrate are given in the caption of Fig. 3.6. The second and fourth layers are separated by an air gap of $h_3 = 2\ cm$ thickness. The bowtie antennas are placed at an horizontal distance D equal more than the free-space wavelength. Each antenna has $0.69\lambda_0 \times 0.66\lambda_0$ dimension, with λ_0 is the free-space wavelength at frequency equal to 10 GHz. Each antenna is excited with aforementioned delta-gap type of source at the port and has been discretized with 599 Rao-Wilton-Glisson (RWG) [169] elementary basis functions outside the delta-gap, as presented in Fig. 3.5. The antennas are meshed using the open source GMSH software [4] with the help of RWG, roof-top and hybrid elementary basis functions. The simulation was run with the help of the Matlab software [139] used to implement the MoM code and the commercial software IE3D [5] on a 64 bits Windows machine with an Intel Xeon CPU/ 2.4 GHz. Fig. 3.7 shows the plot of the simulated results for the real and imaginary parts of the antenna impedance Z_{11} and Z_{22}, and the mutual coupling impedance between the antennas for a high and low frequency range [8-12] GHz and [1-4] GHz, respectively. The IE3D simulations are carried out with a discretization of the array using 20 cells per wavelength considered at the simulation frequency 12 GHz and 0.1 automatic edge cells ratio. Using the MoM code or IE3D software, the infinite ground plane and substrate, and the loss dielectric are considered.

The results are computed for the antenna impedance and mutual coupling in two different frequency ranges, where the thickness of the first dielectric layer equal to $\lambda_0/80$ and $\lambda_0/20$ at low and high frequencies, respectively. The results obtained using the developed MoM code compare very well with the ones obtained with the commercial IE3D software. The small differences in the results are due to different meshing ways and port extension's definition in our code and software IE3D, and may be due to the integration method to obtain the MoM impedance matrix. This deference is noteworthy at high frequency because the scatterer is printed in a very thin lossy dielectric substrate. This comparison of impedance parameters for the array printed on multiple lossy dielectric substrates confirms the engineering reliability of the implemented MoM code.

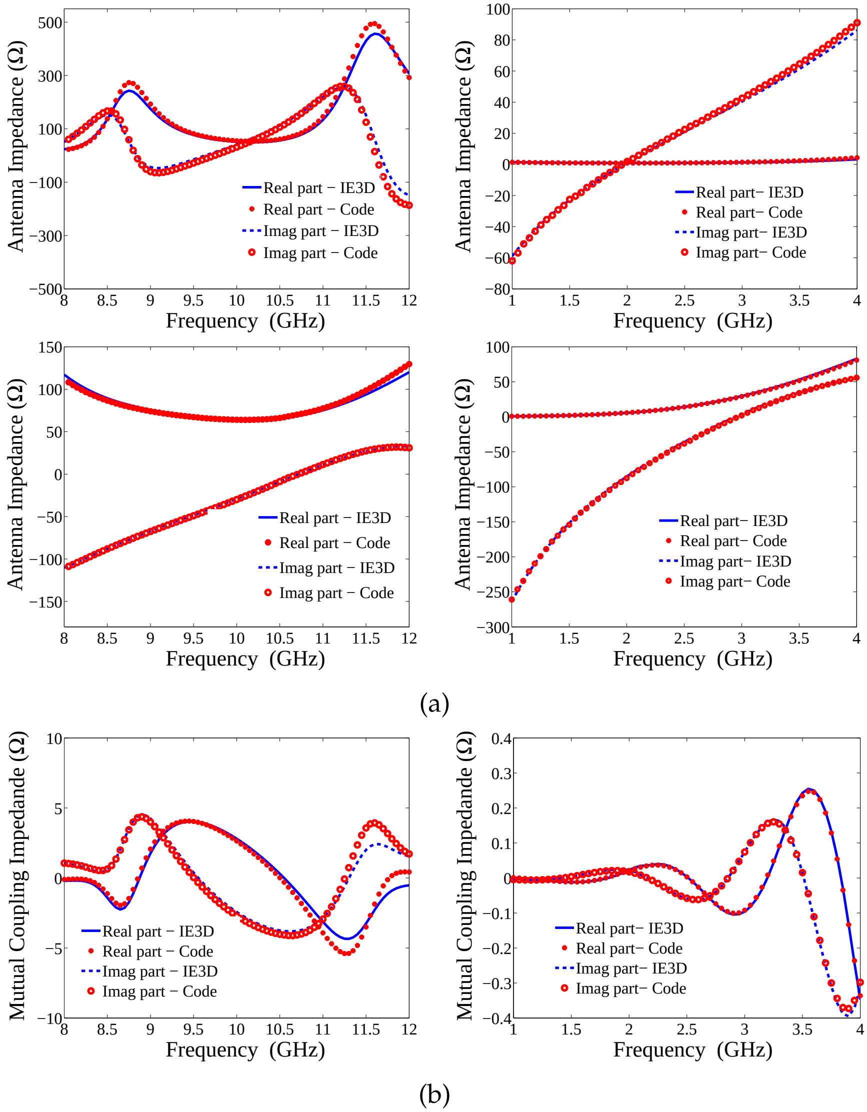

Figure 3.7: Real and imaginary parts of; (a) input antenna impedances (Z_{11} and Z_{22}), and (b) mutual coupling impedance Z_{12}. Left plots: high frequency range. Right plots: low frequency range with horizontal distance between two antennas $> \lambda_0$. At low frequency $\lambda_0 = 12\ cm$ and at high frequency $\lambda_0 = 3\ cm$.

3.3 Modal Analysis Techniques

A modal analysis method is used in general to calculate the modal currents over a conductive object or antennas (such as printed antennas), where those currents are presented by the eigenmodes of a structure. They depend only on the geometry of the structure and not to the excitation.

In this section, simulated results obtained from the combination of the developed MoM code and the modal analysis methods, were analyzed to study the induced current based on a set of eigenmodes on a simple structure such as a rectangular plate. The current distribution on the structure (or scatterer) is initially obtained by the solving of the linear MoM equation [35, 41]. An alternative modal analysis approach is used here to find a set of orthogonal currents which approximates the total current distribution on a structures using the characteristic mode theory [46] as a known modal theory, and others proposed eigenmodes solution methods, slightly simpler than TCM [70, 182]. In the following section we prove that the simulated total current distribution on the scatterer can be calculated using different eigenmode approaches (Fig. 3.8), while the proposed ones are obtained in a simpler way than the TCM. The proposed techniques allow one to generate a complete basis of modes and to express the exact total current density through a linear combination of the extracted eigenmodes. The advantages of our eigenmodes techniques were proved from the convergences of the eigenmode based on decompositions.

3.3.1 Theory of Characteristic Modes (TCM)

Characteristic modes are real current modes that can be computed numerically for conducting structures of arbitrary shape. Since characteristic modes form a set of orthogonal functions, they can be used to expand the total current on the surface of the structure [61]. The theory of characteristic modes has been applied to antenna shape synthesis [60] and chipless RFID tag design [26], and control of obstacle scattering by reactive loading [183]. However, at present, the characteristic modes theory has practically fallen

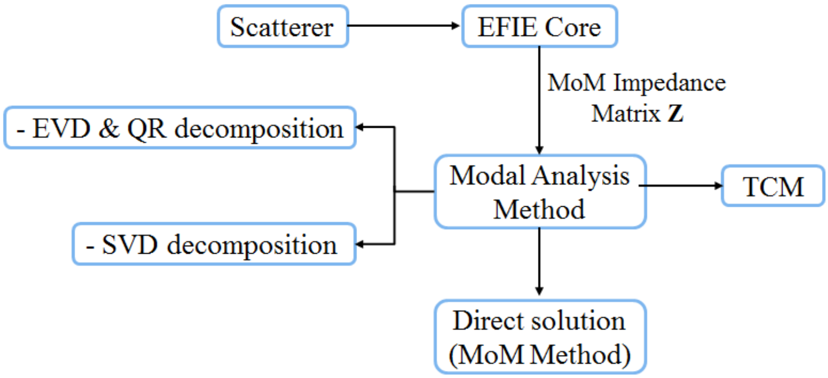

Figure 3.8: Solution for total current I, correspondence between direct MoM solution and modal superposition techniques.

into disuse, in spite of the fact that it leads to modal solutions, which are particularly useful in problems involving analysis, synthesis and optimization of antennas and scatterers [184–186]. Probably, the theory of characteristic modes was almost abandoned in the eighties, because of the amount of computation it required for the extraction of modes. Characteristic modes correspond to the eigen-vectors of a particular weighted eigen-value equation that involves the generalized impedance matrix of the body. Hence, if characteristic modes are to be obtained, the impedance matrix of the body should be calculated at every desired frequency by direct application of Method of Moments (MoM) [35]. Other methods are presented in next section to expand the total current based on a specific decomposition of the MoM impedance matrix. The theory of characteristic modes (TCM) was first developed by Garbacz in 1968 [59], and later refined by Harrington and Mautz in 1971 [61]. Garbacz obtained the modes of conducting bodies of arbitrary shape by diagonalizing the scattering matrix [59, 187]. Alternatively, Harrington and Mautz arrived at similar modes by diagonalizing the generalized impedance matrix of the body [61–63]. In this section, we illustrated the formulation of the TCM for conducting bodies in free space to expand the current distribution.

In the following subsection, a brief overview of the TCM formulation is given as developed in [61]. The characteristic modes for a rectangular plate, which was presented in several publications, such as [6,7], were recalculated using our MoM code.

3.3.1.1 Formulation of TCM using eigen-value Generation Problem

To calculate the characteristic modes for arbitrary structures, such as the rectangular plate shown in Fig. 3.10, the impedance Method of Moment (MoM) matrix of the shape should be generated. As explain in Section 3.2, the impedance MoM matrix $\mathbf{Z}$ is complex, and it can be written as

$$\mathbf{Z} = \mathbf{R} + j\mathbf{X} \tag{3.21}$$

where $\mathbf{R}$ is the real part and $\mathbf{X}$ is the imaginary part matrices of $\mathbf{Z}$. As explained in [62], to compute characteristic modes of a particular conducting body which can be obtained as the eigenmodes of the particular weighted eigen-value, which can be obtained from the generalized eigen-value equation using an eigen-value generation problem [188]. The eigen-value equation is reduced to matrix form using the Galerkin testing technique for the formulation of the MoM linear matrix equation [189], where the MoM matrix $\mathbf{Z}$ is linear symmetric and not Hermitian. Its real and imaginary parts ($\mathbf{R}$ and $\mathbf{X}$) are symmetric matrices. The generalized eigen-value equation

$$\mathbf{X}\, J_n = \lambda_n \,\mathbf{R}\, J_n \tag{3.22}$$

as described in [61] is used to obtain the eigen-vectors J_n (called characteristic mode or eigenmode) and eigen-values λ_n on the surface of a scatterer. A set of real characteristic currents J_n are defined by solving the equations (3.6) and (3.22) with standard algorithms [188]. More details about the theory of characteristic modes are presented in different recent papers as [6,7,46,48,73].

For the given rectangular plate structure in [7,46] of width $W = 4\ cm$ and length $L = 6\ cm$ discretized with 465 RWG basis functions, the first mode has the smallest eigen-value at the resonance frequency of 2.3 GHz, as introduced in [46]. The resonance behavior of the modes can also be inferred from a characteristic angle α_n. The phase lag between the tangential component of characteristic field (a field radiated from a characteristic

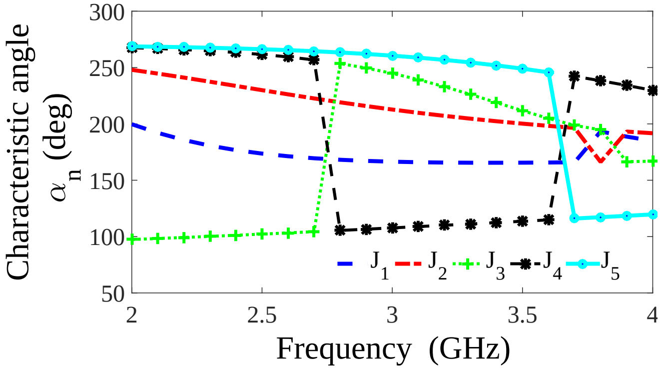

Figure 3.9: The characteristic angle curves associated to the eigenmodes J_n on the rectangular plate calculated from 2 GHz to 4GHz.

current) and the real characteristic mode defines the constant characteristic angle:

$$\alpha_n = 180^\circ - \tan^{-1} \lambda_n \tag{3.23}$$

The variation of α_n with frequency as presented in Fig. 3.9 provides information about the radiation or scattering of each mode [47]. The resonance behaviour of each characteristic mode can be extracted when the angle is equal to 180°, in this case the structure is maximally radiating.

The current distribution at the first resonance (f = 2.3 GHz) of the 5 first characteristic modes J_n are generated for the rectangular plate. The current distribution of each mode is shown in Fig. 3.10. Those distributions very similar to those found in [7, 46] again contribute to validating our MoM code, in this case all media are composed of vacuum.

From [7, 46], the total current obtained by the TCM (superposition of some characteristic modes) should be the same as the current distribution I obtained by inverting the MoM matrix using the equation (3.6); this method being referred to the direct MoM solution in the following sections. Using the TCM, the total current I can be written as

$$I = \mathbf{Z}^{-1} E_x = \sum_{n=1}^{N} \frac{J_n{}^T E_x}{1 + j\lambda_n} J_n \tag{3.24}$$

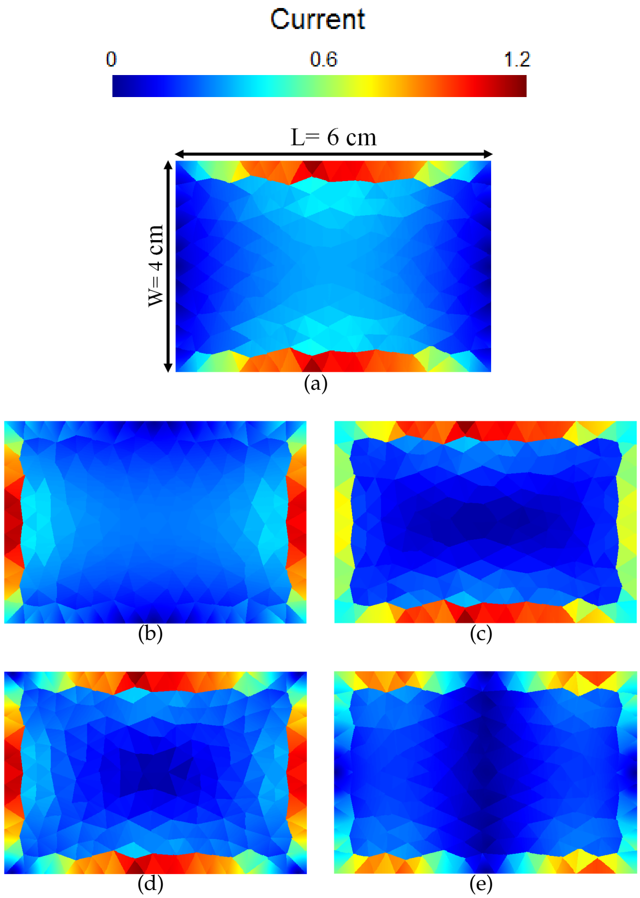

Figure 3.10: Current distribution at first resonance frequency (F= 2.3 GHz) of the first five characteristic modes ((a):J_1, (b): J_2, (c): J_3, (d): J_4, (e): J_5) of a rectangular scatterer of length L=6 cm and width W = 4 cm, resimulated after [6,7].

where J_n are the characteristic currents generated with their associated eigen-values λ_n by solving the generalized eigen-value problems, and E_x is the incident electric field (i.e presented as an incident plane wave or a gap source of an antenna). In this work, the excitation vector (E_x) on the scatterer excited from an antenna obtained as

$$E_x = \mathbf{Z}_{sd}^{-1} I_d \tag{3.25}$$

where $\mathbf{Z}_{sd}$ represents the antenna-scatterer mutual-MoM interactions, and I_d is the current vector on the antenna.

We use here a printed dipole antenna to produce the incident field; the dipole is located at a vertical distance equal to 33 cm. To generate the total current density I with a unit power [46] of each eigen-current radiation, the modes need to be normalized as follows to obtain the normalized eigen-currents $J_n^{'}$.

$$J_n^{'} = \frac{J_n}{\sqrt{J_n^T \mathbf{R} J_n}} \tag{3.26}$$

The total current density is obtained here from equation (3.24) to replace the characteristic modes J_n by the normalized eigen-currents $J_n^{'}$. TCM is used in the literature to analyze several antennas and scatterers with the purpose to determining their basic eigenmodes and their contribution to the total current distribution on the scatterer. However, the accuracy of the total current provided by a limited expansion of the characteristic modes has been rarely cheeked. It was demonstrated in [46] that the set of characteristic modes presents slow convergence when approximating the imaginary part of the input current on the wire antenna. Also, Capek showed in [190] that sum (3.24) is may be incomplete; however TCM produce an incomplete basis of the orthogonal eigen-currents. In the next sections, two other modal techniques are proposed to improve and solve the problem of slow convergence of the eigenmodes and potentially incomplete of basis orthogonal eigenmodes by following a simpler approach based on relatively basis mathematical algorithms to diagonalize the MoM impedance matrix.

3.3.2 EVD & QR - Eigenmodes Approach

Radiation from a microstrip patch antenna is estimated by solving the electric field integral equation (EFIE) in the form of the mixed-potential integral equation (MPIE) discretized with the MoM [35]. The MoM formulation for these problems solves the linear matrix equation (3.5) to extract a set of eigen-currents on the metallic structures and the total current density on the scatterer. In the previous section, we presented a modal method is the theory of characteristic modes based on generalized eigen-value decomposition, where the eigen-currents are real, following the separation of the real and imaginary parts of MoM impedance matrix (the eigen-currents should be normalized to generate the total surface currents). Also the characteristic modes are orthogonal assuming a specific scalar product described in [61].

In this section, a new modal technique is introduced based on eigen--values decomposition (EVD) [191] and QR factorization of the symmetric $N \times N$ MoM impedance matrix $\mathbf{Z}$. The objective is to solve the linear MoM equation $\mathbf{Z}\, I = E_x$ to extract the current distribution I of N unknown coefficients. The current is defined by a set of eigenmodes on the surface of the structure. To calculate eigenmodes using the EVD, the $\mathbf{Z}$ matrix is factorized as

$$\mathbf{Z} = \mathbf{X}\,\mathbf{\Lambda}\,\mathbf{X}^{-1} \tag{3.27}$$

where Λ and $\mathbf{X}$ represent, respectively, the eigen-values and eigen-vectors matrices. Hence, the current vector I can be represented as:

$$I = \mathbf{Z}^{-1}\, E_x = \mathbf{X}\,\mathbf{\Lambda}^{-1}\,\mathbf{X}^{-1}\, E_x \tag{3.28}$$

As explained before, when the Galerkin testing procedure is employed, the $\mathbf{Z}$ is a complex symmetrical matrix and not Hermitian, hence the columns of $\mathbf{X}$ are not orthogonal. In order to be able to describe the current in terms of orthogonal eigen-vectors, and to obtain a decomposition of $\mathbf{Z}$ with a diagonal matrix in the middle and orthogonal matrices at the extremes, we apply the QR factorization method to $\mathbf{X}$ and the equation (3.28) rewritten as

$$I = \mathbf{Q}\,\mathbf{R}\,\mathbf{\Lambda}^{-1}\,\mathbf{R}^{-1}\,\mathbf{Q}^{H}\, E_x \tag{3.29}$$

where the matrix$\mathbf{Q}$ is filled with an orthogonal set of column eigen-vectors and $\mathbf{R}$ is an upper triangular matrix. In practice, for small structures, $\mathbf{Q}$ is close to $\mathbf{X}$ and $\mathbf{R}$ is nearly an identity matrix. To simplify the mathematical formulation of the current I, a new matrix is defined as

$$\mathbf{W} = (\mathbf{R}\,\mathbf{\Lambda}^{-1}\,\mathbf{R}^{-1}\,\mathbf{Q}^{H})^{H} \tag{3.30}$$

where the columns of **W** and the orthogonal matrix **Q** represent the 'associated eigen-currents' and the eigenmodes on the surface on the structures, respectively. With those definitions, equation (3.29) can be rewritten for a selective excitation, in compact matrix form

$$I = \mathbf{Q}\,\mathbf{W}^H\,E_x \tag{3.31}$$

This indicates that the importance of a given eigenmodes (columns of **Q**)

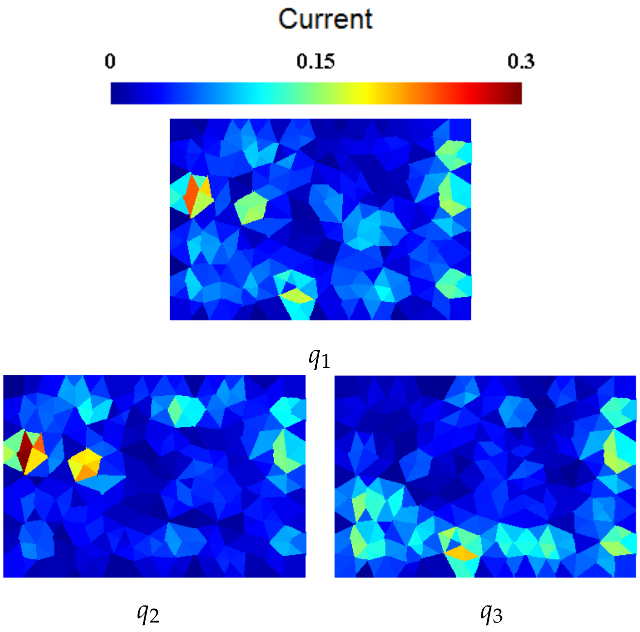

Figure 3.11: Current distribution at frequency 2.3 GHz of the three first eigenmodes on the rectangular scatterer located in the air.

depends on the projection of the corresponding column of W on the excitation E_x. A modal analysis of the example presented in previous section (rectangular plate) is generated based on the proposed EVD & QR- eigenmodes technique. The current distribution of first three eigenmodes q_i on the rectangular plate are presented in Fig. 3.11 at frequency 2.3 GHz which is not the resonance frequency of those eigenmodes.

In this section, the eigenmodes are extracted by using the proposed modal technique based on EVD decomposition for the diagonalization of MoM impedance matrix and QR-factorization for decomposition of the eigen-vectors matrix. Another modal technique is presented, in the next section, to simplify the EVD & QR-eigenmodes approach also to obtain orthogonal eigen-vectors. The eigenmodes technique is based on the singular value decomposition (SVD) to study the modes on a scatterer for its easier use. The compilation of the developed algorithm based on this method is faster than other eigenmodes techniques.

3.3.3 SVD - Eigenmodes Technique

In this section, another modal analysis method is discussed. The method is based on a matrix algebra technique called the Singular Value Decomposition (SVD) [192] of the MoM impedance matrix **Z**. This decomposition is capable to obtain an orthogonal set of eigenmodes which provide interesting insight physical since fields radiate by the orthogonal eigenmodes, they are also orthogonal to each other. An initial discussion of the SVD was presented in the Linpack Users' Guide [193]. The SVD is a standard matrix algebra technique for diagonalizing any matrix, especially the non--Hermitian matrices. It is the generalization of eigen-value analysis for Hermitian matrices to general matrices [191]. Although the algorithms implementing the SVD decomposition have existed for decades, recently the technique is rarely been applied to MoM problems. This is surprising in that, as we describe, the SVD is the appropriate technique for the diagonalization of MoM impedance matrix **Z**. It is the matrix that results from the finite dimensional equation (3.16) and it is used in both previous eigenmodes techniques. **Z** is complex symmetric and not purely Hermitian, hence, we almost certainly cannot diagonalize it through the TCM and the EVD & QR-technique involving a unitary matrix of eigen-vectors. However, using the SVD there are two different unitary matrices, and diagonal matrix that's contains classify singular values.

The goal of the modal technique proposed here is to describe the currents in terms of orthogonal eigen-vectors. In order to be able to obtain a decomposition of the MoM impedance matrix (**Z**) with a diagonal matrix in the middle and orthogonal matrices at the extremes, a factorization of **Z** matrix using a direct SVD decomposition of the matrix

$$\mathbf{Z} = \mathbf{U}\,\mathbf{\Sigma}\,\mathbf{V}^{H} \tag{3.32}$$

where $\mathbf{\Sigma}$ is a diagonal matrix whose diagonal elements consist of real and non-negligible singular values, **U** and **V** are orthogonal matrices (unitary matrices as its complex matrices) of singular vectors. The columns of **V** represent the eigenmodes. The current distribution of the first three eigenmodes on the rectangular plate, discussed in Section 3.3.1, correspond to the smallest singular values shown in Fig. 3.12 at frequency 2.3 GHz. In

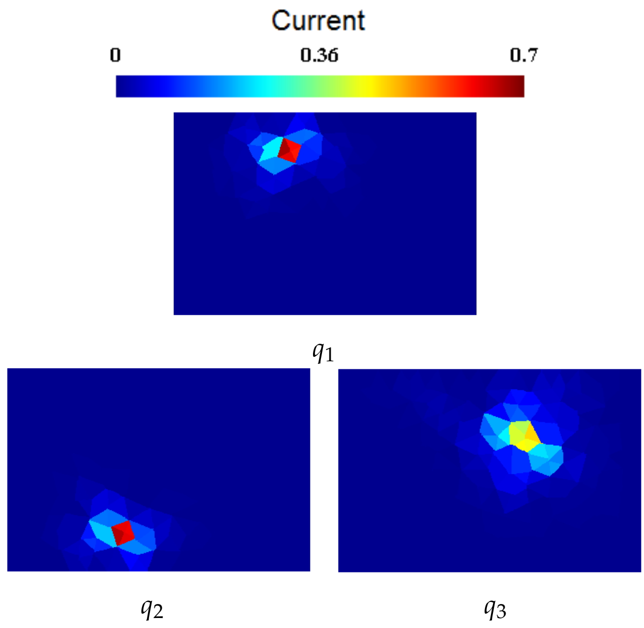

Figure 3.12: Current distribution at frequency 2.3 GHz of the first three eigenmodes expanded using SVD technique on the scatterer.

practice, for small structures, **U** is close to **V**. After applying the SVD decomposition, the current vector I can be represented as:

$$I = \mathbf{V}\,\mathbf{\Sigma}^{-1}\,\mathbf{U}^{H}\,E_x \tag{3.33}$$

where the product $\langle \mathbf{U}, E_x \rangle$ presents the coefficient of the incident field with respect to *associated eigen-vectors* (columns of $\mathbf{U}$).

The diagonalization problem of the MoM impedance matrix and the expansion of a set of orthogonal eigen-currents over a scatterer can be solved by referring to the TCM, proposed EVD & QR and SVD eigenmodes techniques. However, the set of orthogonal currents calculated using TCM approximates the total surface current on a structure while it can be regenerated with negligible residual currents from the eigenmodes superposition obtained by EVD & QR and SVD techniques because the basis of modes are numerically complete. In the next section, a validation of the proposed eigenmodes technique will be discussed through a comparison between the convergences of the different types of eigenmodes.

3.4 Convergences of Modal analysis methods

As we mentioned above and in [46], characteristic modes associated to a radiating structures do not model properly of the current on the scatterer. The problem of slow convergence of the set of characteristic modes exploited by TCM is still noteworthy and the basis of eigenmodes is numerically incomplete [190]. To illustrate this problem, the rectangular scatterer already studied in previous sections is going to be used to study the convergence of eigenmodes on the scatterer in two cases. First, the radiating structure and the antenna excitation are in air. Second, the system (scatterer and antenna excitation) is printed on infinite lossy dielectric substrate of relative permittivity $\epsilon = 4.3$ and loss tangent $\delta = 0.02$, backed by a ground plane. The system presented in Fig. 3.13 is studied in both cases considering near-field and far field excitations.

However, as comparisons are made between modal methods: TCM, proposed technique and direct MoM method. Indeed, when plotted in a linear scale the total current distribution obtained with a basis of modes found by one of the three different approaches cannot be distinguished. For that it is better to plot the residual surface current as shown in Fig. 3.14,

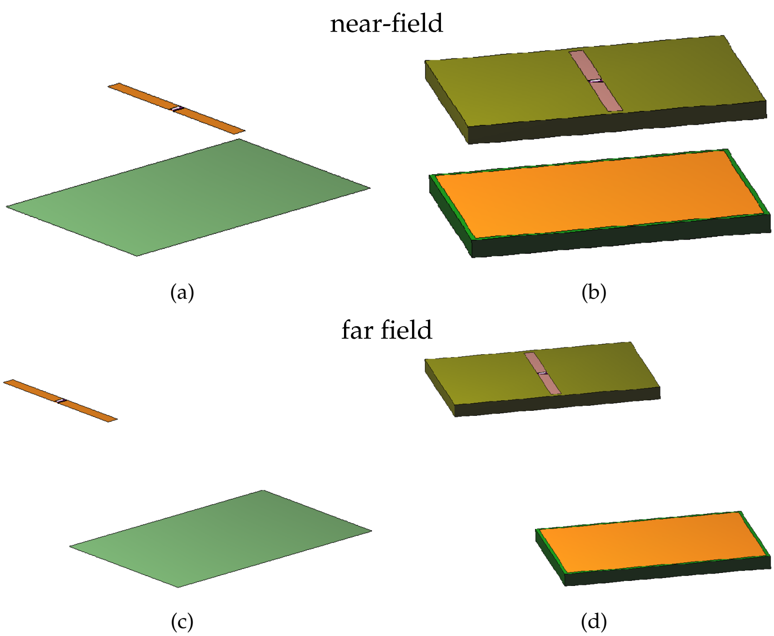

Figure 3.13: Systems studied. Left Pictures: Systems located in the air for (a) near-field and (c) far-field. Right Pictures: Systems printed on multi-layer lossy dielectric medium backup with ground plane for (b) near-field and (d) far-field.

where we plot the total current in free space rectangular plate which is calculated through the direct MoM method. Fig. 3.14 presents the residual current defined above using each modal analysis method for far-field excitation. Those results indicate that the set of orthogonal eigen-currents obtained by referring to the TCM technique just approximates (not precisely) the total surface current on the structure.

To exhibit the limitation of TCM and to study the other proposed modal technique, a comparison was presented through the Root Mean Square Error (RMSE) which is defined as $\| I_{res} \|_2 \ / \ \| I_{MoM} \|_2$ where I_{res} is a residual current calculated as $I_{MoM} - I_{tech}$. The total surface current I_{MoM} is treated directly as usually employed in the method of moments and I_{tech} is the total current expanded by the superposition of eigenmodes obtained from

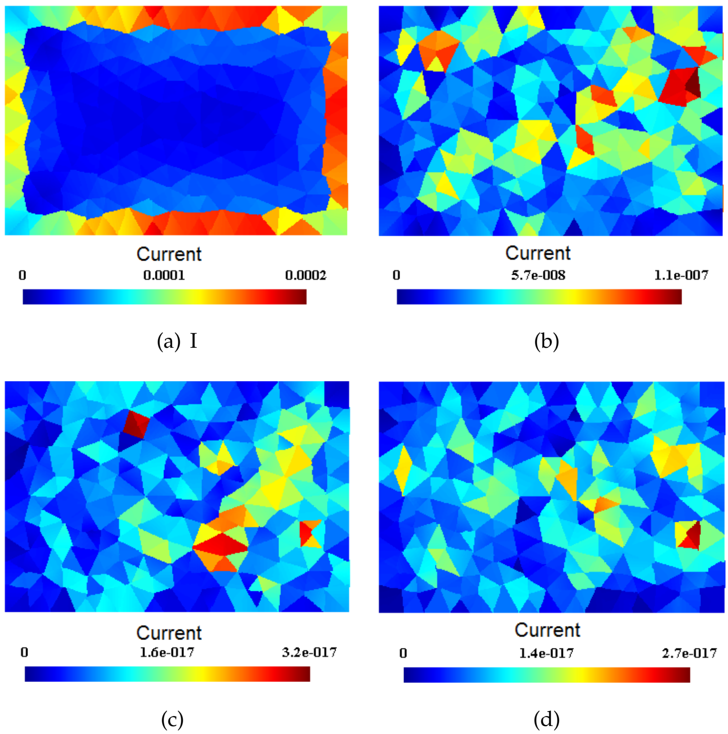

Figure 3.14: Top left Picture: Total current distribution on the rectangular scatterer at frequency 2.3 GHz. Residual current I_{res} using (b) TCM, (c) EVD & QR, and (d) SVD modal approach

application of modal analysis techniques discussed in Section 3.3. The relative error level will be given in (%) and the engineering accuracy will be achieved when the error level is less than 1 %, as compared to the reference solution obtained from the MoM method. The relative errors with respect to the MoM solution are shown in Figs. 3.15, 3.16, 3.17, and 3.18,

The results presented in those figures makes out the limitation of TCM technique, as a matter of fact the characteristic modes are unable to expand exactly the current peak exhibited by the linear MoM equation (3.19). This limitation is due the imaginary part of the current calculated by TCM which is very dependent to the position of the excitation source, not to the resonances of the scatterer [46]. It can be an explanation for the results re-

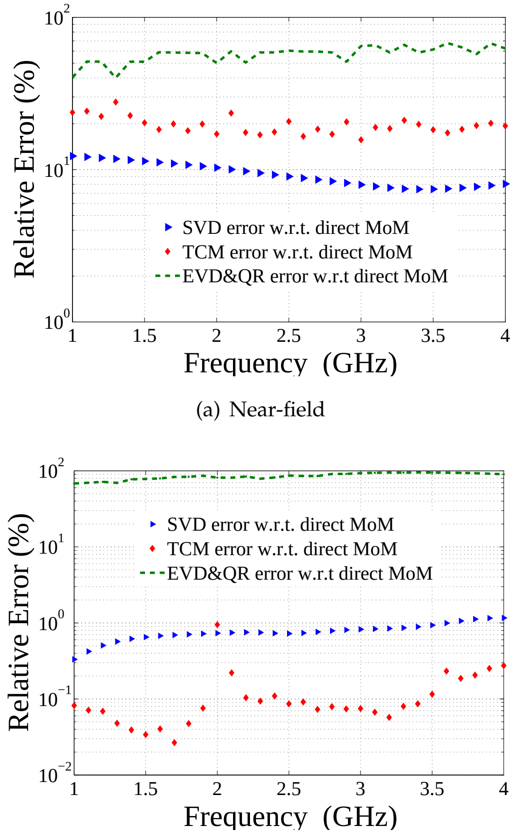

(a) Near-field

(b) Far field

Figure 3.15: Relative error (in %) with respect to the direct MoM solution in the total current distribution on the rectangular scatterer (see Fig. 3.13. (a) and (c)) for near-field and far field excitation. The errors obtained using 233 modes (half number of total modes) versus the frequency by TCM, SVD and EVD & QR-eigenmodes techniques.

lated to TCM error presented in Fig. 3.16. For relative errors less than 3.5 % at frequency 2.3 GHZ, all even modes are necessary in the expansion of the current in the near-fied and more than 10 modes are needed in far field excitation. Hence, the performance of the TCM method depends on the feeding arrangement. Contrary to what is defined the theory of character-

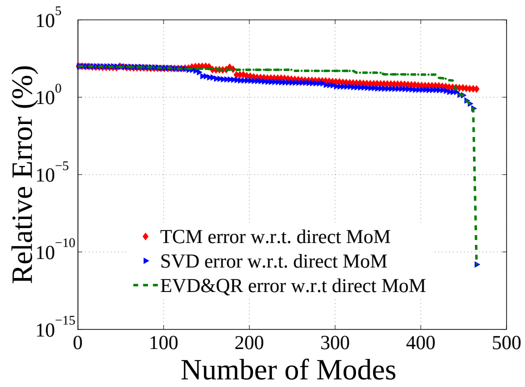

(a) Near-field

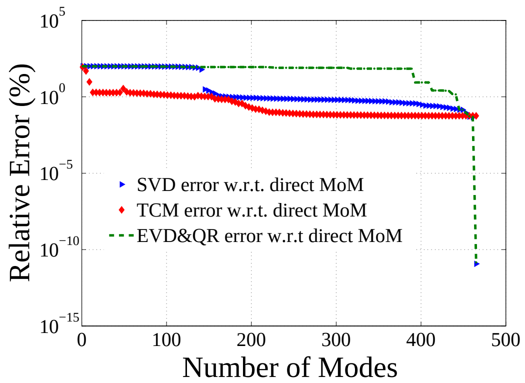

(b) Far field

Figure 3.16: Relative error (in %) with respect to the direct MoM solution in the total current distribution on the rectangular scatterer (see Fig. 3.13. (a) and (c)) for near-field and far field excitation. The errors obtained versus the number of modes (j_n, V_n and q_n) at frequency 2.3 GHz.

istic modes presents limitations over the dielectric substrate and ground plane. It is so clear in Fig. 3.17 that the relative error is around 10^2 % over the frequency range using 233 even modes. The TCM presents in Figs. 3.18 a very slow convergence of the series of characteristic modes at 2.3 GHz for the printed case, for both near or far field excitations. Moreover, the relative error decreases rapidly to be well below 10^{-15} % once the number of

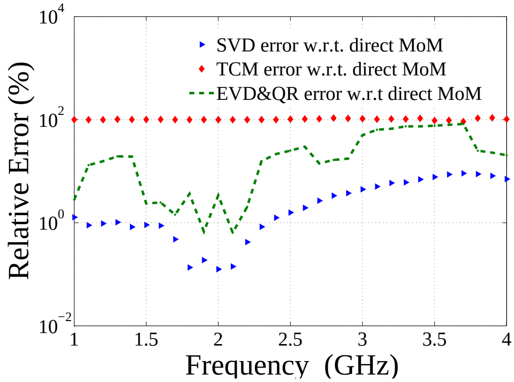

(a) Near-field

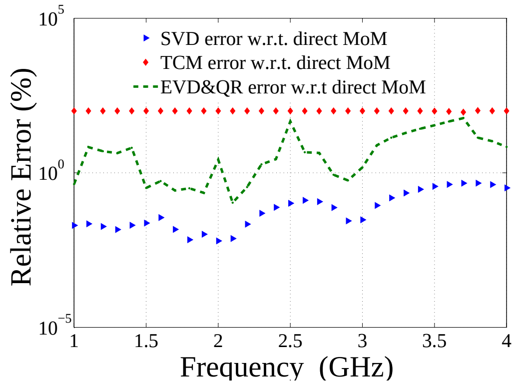

(b) Far field

Figure 3.17: Relative error (in %) using the TCM, SVD and EVD & QR--eigenmodes techniques with respect to the direct MoM solution in the total current distribution on the rectangular scatterer printed on a lossy dielectric substrate in near-field and far-field. The error is calculated versus frequency using 233 modes.

modes is almost total using EVD & QR or SVD-eigenmodes techniques in any system case. The EVD & QR-eigenmodes approach is not better than TCM in free space but it present a numerical complete basis to generate the total current. This proposed eigenmodes technique leads to a good convergence of the series of eigenmodes on the printed scatterer, and the

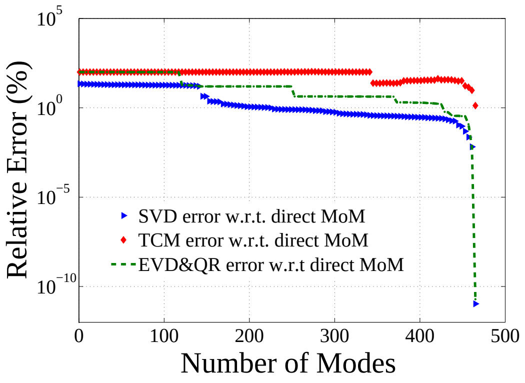

(a) Near-field

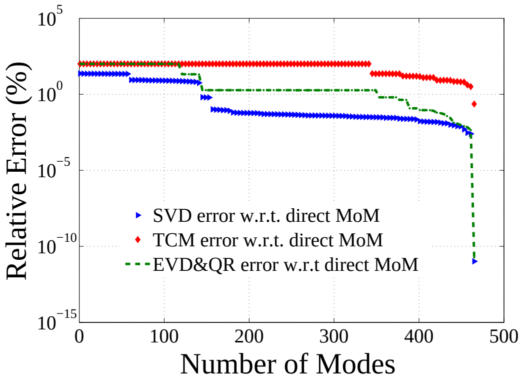

(b) Far field

Figure 3.18: Relative error (in %) using the TCM, SVD and EVD & QR-eigenmodes techniques with respect to the direct MoM solution in the total current distribution on the rectangular scatterer printed on a lossy dielectric substrate in near-field and far-field. The error is calculated versus the number of modes (j_n, V_n and q_n) at frequency 2.3 GHz.

basis is still complete. For relative errors equal to 1 % the use of EVD & QR--technique requires a high number of modes: 420 modes in the near-field and 350 modes in the far field, compared to the 465 modes on the scatterer. This shows how the use of this method does not lead to fast convergence.

Figs. 3.17 and 3.18 show the relative errors calculated using the TCM and the proposed eigenmodes techniques with respect to the total current obtained by direct MoM solution. This error is calculated in near and far field when the rectangular scatterer and the excitation antenna are printed on lossy dielectric substrates backed by a ground plane. Fig. 3.18 shows a rapid convergence toward the direct MoM solution, using the proposed eigenmodes techniques.

The proposed SVD-eigenmodes approach evaluates the total surface current as a sum of eigen-currents. The relative error is less than 0.4 % (see Fig. 3.17) for the proposed SVD-eigenmodes technique using a set of 233 orthogonal eigenmodes, along the range of frequency in printed case at near and far field. The relative error at 2.3 GHz is below 1 % for 200 modes on printed structure in near-field and more than 140 modes on system located in free space or printed on dielectric substrate in the far field, and the relative error decreases rapidly to remain below 0.05 % once the number of modes is greater than half of the total number of modes.

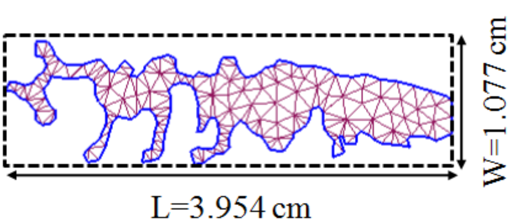

Figure 3.19: The irregular fractal jet-fluid structure.

The convergence of the modes is studied for another structure with complex geometry (see Fig. 3.19) printed on a lossy dielectric substrate backed by a ground plane, the structure discretized with 464 triangular RWG basis functions. Comparisons are made between modal methods: TCM, EVD & QR-eigenmodes approach, SVD eigenmode technique and direct MoM method.

The error is calculated in near-field versus frequency using 100 modes. After that, the relative error is obtained at frequency 3.4 GHz in functions of the number of basis functions. Figs. 3.20 and 3.21 shows the relative errors with respect to the MoM solution.

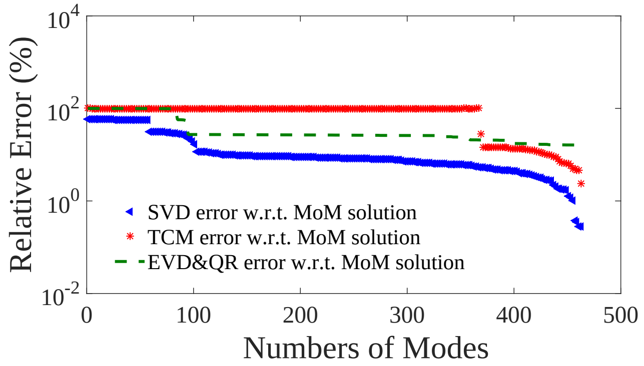

Figure 3.20: Relative error (in %) using the TCM, SVD and EVD & QR- - eigenmodes techniques with respect to the direct MoM solution in the total current distribution on the printed fractal jet-fluid scatterer in near-field. The error is calculated versus the number of modes (j_n, V_n and q_n) at frequency 3.4 GHz.

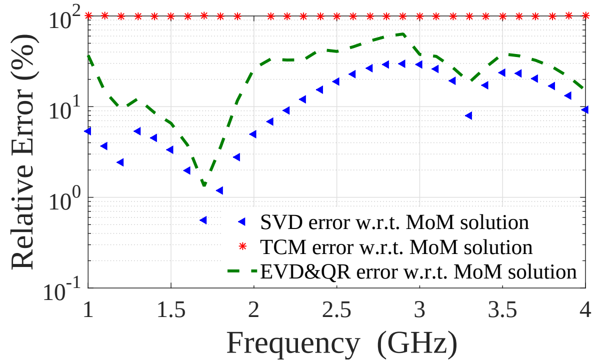

Figure 3.21: Relative error (in %) using the TCM and proposed eigenmodes techniques with respect to the MoM solution for the fractal jet-fluid rectangular scatterer printed on a lossy dielectric substrate with near-field excitation. The error is calculated versus frequency using 100 modes.

The TCM presents in Figs. 3.20 a very slow convergence of the series of characteristic modes at 3.4 GHz. For relative errors less than 3 % all even modes are necessary in the expansion of the current in the near-fied. It is presented in Fig. 3.21 and for the printed fractal jet-fluid scatterer that the relative error is still very close to 10^2 % over the frequency range using 100 even modes. Hence, the limitation of the theory of characteristic modes is demonstrated for the structures printed on a lossy dielectric substrate and backed by a ground plane.

Moreover, the relative error decreases rapidly to be well below 10^{-10} % once the number of modes is almost total using EVD & QR or SVD-eigenmodes techniques. For relative errors equal to 3 % the use of EVD & QR-technique requires all even modes, this shows the slow convergence of eigenmodes. Then this technique is not better than TCM.

Fig. 3.20 shows a rapid convergence toward the direct MoM solution, using the proposed SVD-eigenmodes techniques. The relative error at 3.4 GHz is below 10 % for more than 90 modes for system printed on dielectric substrate in the near-field. The relative error is very small (see Fig. 3.21) for the proposed SVD-eigenmodes technique using a set of 100 orthogonal eigenmodes along the range of frequency.

Those proposed eigenmodes technique leads to a good convergence of the series of eigenmodes on the printed scatterer. Therefore, the proposed method based on SVD decomposition can be viewed as a robust modal analysis method for the printed structure on lossy dielectric substrate with ground plane in the near/far field. We demonstrated a good convergence of the set of eigenmodes for printed structures. Hence, the SVD method can be a very useful tool for generating a special current on any object. Also, the current can be depending to the feeding position and the thickness of the substrate which separates the structure and the ground plane.

3.5 Conclusion

In this chapter, a Method of Moments formulation based on the Electric Field Integral Equation (EFIE) for the multilayered medium has been recalled to allow the extraction of the induced current distribution on the surface of a scatterer in free space or printed on lossy dielectric substrates backed by a ground plane. When, the elements of the impedance matrix are obtained by the convolution of the basis and testing functions through the multilayered medium Green's function. The convergence of computed Green's function was improved by extracting the effective homogeneous medium contribution from the layered medium Green's function. For the effective homogeneous lossy medium part, the existing code of the lab was modified and exploited. The results were validated with the ones obtained with the commercial IE3D software. An excellent agreement has been achieved, which confirms the engineering accuracy of the developed multilayered medium code. It should be noted that not all the validations are presented here and more comparisons with results obtained with IE3D will be provided in specific sections of the future chapters. In the last part, we presented different modal approaches to expand the total current distribution on the scatterer. The MoM impedance matrix is obtained from the developed code using the MoM for the multilayered lossy medium. To MoM code is used to compare different modal analysis methods to expand the total current distribution on a rectangular plate [6], which is studied as a perfectly conducting structure and as a printed patch.

The theory of characteristic modes is recently the famous technique for modal analysis. As mentioned in this chapter, the TCM technique is characterized by a slow convergence of the characteristic modes with incomplete basis modes, where is not simple to compile the characteristic modes and to extract the total current on the scatterer. The slow convergence of the characteristic modes is notable for the structure printed on a lossy dielectric substrate backed by a ground plane. In other hand, we proposed the EVD & QR-eigenmodes technique which looks more complicated to find the eigenmodes. In contrast, this proposed technique leads to the expansion of the total current with rapid convergence of eigenmodes. The SVD-

-eigenmodes technique is simple to implement and the convergence of the set of orthogonal eigenmodes is not really slow in the printed patch case.

The SVD approach will be used in the next chapters to perform the modal analysis of a scatterer printed on a lossy dielectric layer backed by a ground plane. This will be done in the next chapter in the context of chipless passive Radio Frequency Identification application and for other tags with special geometry in last chapter.

Selective Excitation of Chipless Passive RFID Tags using SVD-Eigenmode Approach

4

4.1 Introduction

The passive chipless RFID technology has received great research interest [21, 22], in last years, owing to its lower fabrication cost and smaller size [12, 194]. As mentioned in Chapters 1 and 2, the reader unit and the tag communicate via backscattering of electromagnetic waves [11] for the passive RFID systems at UHF frequencies. In fact, the chipless scatterer (i.e. tag) can be manufactured using materials such as plastic or conductive polymers [23,194]. These tags have been envisaged for various types of applications, such as automatic identification, where the natural resonance of the scatterer is exploited as the identifier [97, 153].

Chipless RFID systems are based on generating a unique radio-frequency signature from the tags, which in turn allows the use of cryptographic techniques [108,195] to prevent the falsification of tags. However, such an identification technique comes with two challenges: (i) the discrimination of the response of the tag w.r.t. that of the environment and (ii) the extraction of rich information resulting from the shape of the tag. Consequently, the identification performance of chipless passive tags heavily depends on the quality with which the signal can be extracted from the response of the background medium. Besides, new methods are needed to extract more information from the tag.

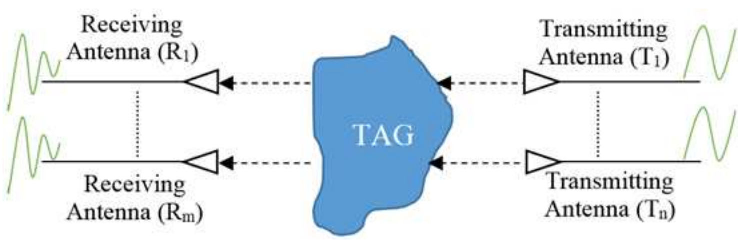

Figure 4.1: General Passive RFID System.

In this chapter, we propose a novel eigenmode analysis method to exploit the specific frequency response of a tag, which can for instance be printed on a thin lossy dielectric substrate backed by a ground plane. As shown in Fig. 4.1, the tag is illuminated by an antenna array, acting both as a transmitter and as a reader. When the reader corresponds to arrays, the multiplicity of the responses from the tag provides independent signatures for the same tag, allowing the user to better distinguish the tag from others, and to improve its independence from scattering by the environment. More precisely, this approach is based on the expansion of the induced current in terms of particular eigenmodes of the tag, obtained in the singular-value sense. During this process, the most significant eigenmodes are harnessed to exploit different frequency responses and to extract more information from the tag.

The numerical analysis of scatterers using eigenmode techniques has been presented in a plurality of works, such as the characteristic modes theory [153] defined first by Garbacz, Harrington and Mautz [59, 61, 62]. This theory was based on diagonalizing the scattering [59] and the generalized impedance [61, 62] matrix of the body. Other related works include that of Shen and Macphie [196], Stuart [197] and commercial Eigen-solvers, such as COMSOL [198] and HFSS [199]. Also, Eigen-solvers are an option in some Method of Moments (MoM) codes [200]. The eigenmodes are obtained in the frequency domain in the framework of the MoM formulation [26, 35] for dielectric and magnetic planar structures [6, 201]. Some research dealing with integral-equation methods describe how to determine the modes of many types of many radiation or scattering structures, such as transmission lines or cavities [47, 202]. Recently, the eigen-value decomposition of the MoM impedance matrix [70, 203] has been used to solve the problem of finding the eigenmodes of scatterer. A preliminary eigenmodes analysis based on the eigen-value decomposition and QR factorization of the MoM impedance matrix was presented in [70] to study some structures printed on a dielectric layer. The method presented in [70] ensured the orthogonality properties of eigenmodes using plane wave excitations. In the present work, a novel technique is proposed to study a passive chipless RFID tag printed on a thin lossy dielectric substrate. The current on the tag is mapped into a new set of eigenmodes, through the singular-value decomposition (SVD) [191] of the MoM impedance matrix of the scatterer. Besides, an antenna array is printed on a multilayered dielectric material acting as near-field sources (see Fig. 4.2). The array has several transmitters to excite the scatterer and to induce the currents on the metallic tag and also several receivers to analyse the scattered fields. The transmitters and receivers are made of especially designed printed dipoles.

The proposed analysis leads to a methodology for exciting specific eigenvectors, and to suppress the unwanted eigenmodes through near-field beamforming on transmit. Moreover, beamforming on receive allows further independence of the response from unwanted eigenmodes. The final goal is the exploitation of strong eigenmodes that may elevate the signal above the background response, while providing a highly characteristic signature.

In Section 4.2, the proposed eigenmodes formulation is described: the induced currents are described in terms of eigenmodes and it is explained how specific eigenmodes can be selected through beamforming on transmits and receives. The proposed passive chipless RFID system and the realized configuration are described in Section 4.3.1. The results obtained with the proposed method, as well as experimental validation, are presented in Section 4.3.2. Specific responses of the tag obtained by exploiting the multiple excitation and reception channels are presented in Section 4.3.3. Finally, conclusions and future work are drawn in Section 4.4.

4.2 Eigenmodes Analysis Methodology

The chipless passive RFID problem targeted in this work is intrinsically defined in the near-field and can be described through a set of orthogonal current distributions. This will be done through a new eigenmodes analysis based on classical singular-value decomposition (SVD) [191] of the Method-of-Moments (MoM) impedance matrix ($\mathbf{Z}$) of the printed tag, which fully characterizes its response to near-field excitations.

The proposed eigenmode approach is presented for the case of multiple excitations (Section 4.2.1) and for reception channels (Section 4.2.2). We explain how distinct responses associated with different eigenmodes of the tag can be extracted through a beamforming process on transmit and on receive.

4.2.1 Eigenmodes Analysis of the Tag

We start by describing the current distribution on the tag using an eigenmode decomposition in Section 4.2.1.1. Using this technique and multiple excitations, the study of the current distribution is presented in Section 4.2.1.2.

4.2.1.1 Eigenmodes and Total Current Distribution on the Tag

When the source antennas illuminate the printed scatterer (tag) as shown in Fig. 4.2, the current distribution on the tag can be obtained through the

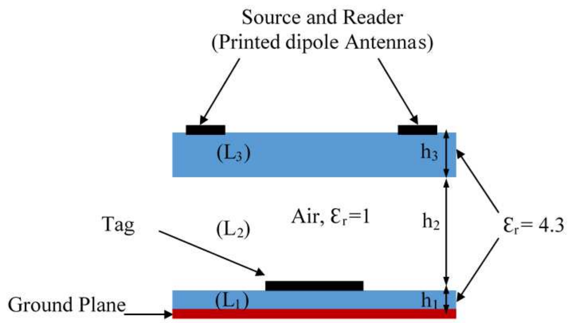

Figure 4.2: Chipless passive RFID system printed on a multilayer dielectric (FR4) substrate. L_1, L_2, and L_3 denote consecutive layers. h_1 = 0.16 cm, h_2 = 3 cm and h_3 = 0.32 cm. ε_r is the dielectric constant of the substrate.

MoM technique. The tag is discretized with Rao-Wilton-Glisson (RWG) basis functions [43, 169]. The MoM formulation allows the determination of the currents on the metallic structure as:

$$\mathbf{Z}_t \; I_t = E_t \tag{4.1}$$

where $\mathbf{Z}_t$ is the MoM impedance matrix of the tag and E_t is the excitation vector on the tag. E_t corresponds to the field from the source antennas, tested by basis functions on the scatterer. I_t is a vector containing unknown current coefficients on the tag. When the Galerkin testing procedure is employed, the resulting MoM impedance matrix $\mathbf{Z}_t$ is a symmetrical [204] but not purely Hermitian matrix. Hence, its eigen-values and eigen-vectors are complex and non-orthogonal. In order to be able to describe the currents in terms of orthogonal vectors, and to obtain a decomposition of $\mathbf{Z}_t$ with a diagonal matrix between orthogonal matrices, the SVD decomposition is used. The factorization of the $\mathbf{Z}_t$ matrix follows as:

$$\mathbf{Z}_t = \mathbf{U}\,\mathbf{\Sigma}\,\mathbf{V}^H, \; with \quad \mathbf{\Sigma} = diag\{\sigma_1, \sigma_2 ..., \sigma_n\} \tag{4.2}$$

where the diagonal elements of $\mathbf{\Sigma}$ consist of real singular values σ_j. $\mathbf{U}$ and $\mathbf{V}$ are orthogonal matrices. The columns of $\mathbf{V}$ represent the eigen-vectors of the tag, while the columns of $\mathbf{U}$ will be named *associated eigen-vectors*. In practice, for a small scatterer, $\mathbf{U}$ is close to $\mathbf{V}$. The columns of $\mathbf{V}$ and $\mathbf{U}$ are given in the ascending order of corresponding singular values.

The transmitting and receiving antennas can also be included in the analysis. The MoM system of equations is then characterized by a matrix of size $(NN_d + N_t) \times (NN_d + N_t)$. Here, N represents the number of source antennas (index d), each with N_d basis functions, while N_t is the number of basis functions used to represent the currents on the tag (index t). The full set of MoM equations can be expressed as:

$$\underbrace{\begin{bmatrix} \mathbf{Z}_t & \mathbf{Z}_{td_1} & \mathbf{Z}_{td_2} & \cdot\cdot & \mathbf{Z}_{td_N} \\ \mathbf{Z}_{d_1 t} & \mathbf{Z}_{d_1 d_1} & \mathbf{Z}_{d_1 d_2} & \cdot\cdot & \mathbf{Z}_{d_1 d_N} \\ \vdots & \vdots & \vdots & \vdots & \vdots \\ \mathbf{Z}_{d_N t} & \mathbf{Z}_{d_N d_1} & \mathbf{Z}_{d_N d_2} & \cdot\cdot & \mathbf{Z}_{d_N d_N} \end{bmatrix}}_{\mathbf{Z}_{tot}} \begin{bmatrix} I_t \\ I_{d_1} \\ \vdots \\ I_{d_N} \end{bmatrix} = \begin{bmatrix} 0 \\ E_{d_1} \\ \vdots \\ E_{d_N} \end{bmatrix} \tag{4.3}$$

where $\mathbf{Z}_t$ represents the self-MoM interactions matrix for the tag, $\mathbf{Z}_{d_j t}$ are the antenna-tag mutual-MoM interactions, and $\mathbf{Z}_{d_i d_j}$ are the antenna-antenna MoM interactions for i and j ranging from 1 to N. I_t is the current vector on the tag, I_{d_j} is the current vector on antenna d_j and E_{d_j} are the corresponding excitation vectors.

Let us momentarily assume[1] for analysis purposes that the currents on the antenna I_{d_j} are known as $I_d = \left[I_{d_1}^T \; I_{d_2}^T \; \cdots \; I_{d_N}^T \right]$. From the first block line in (4.3), the currents I_t on the scatterer are obtained from

$$\mathbf{Z}_t \; I_t = -\sum_{j=1}^{N} E_j^e \tag{4.4}$$

where E_j^e is the excitation vector on the scatterer excited from antenna j, obtained as:

$$E_j^e = \mathbf{Z}_{td_j} \; I_{d_j} \tag{4.5}$$

The surface current on the tag, I_t, is obtained using the MoM formulation (4.1), it can be defined by a summation over the source antennas d_j

$$I_t = \sum_{j=1}^{N} I_{tj} \tag{4.6}$$

[1]In Sections 4.2.1 and 4.3.3, the current on the patch will be obtained from currents on the dipoles, the latter being calculated in the absence of the patch. Appendix B provides details about this approximation.

The current I_{t_j} denotes the current distribution on the tag for each possible excitation E_j^e. After applying the SVD decomposition to $\mathbf{Z}_t$, the current I_{t_j} can be represented by a summation over the eigenmodes (columns of $\mathbf{V}$), in the form

$$\begin{aligned} I_{t_j} = (\mathbf{Z}_t)^{-1} E_j^e &= \mathbf{V}\,\mathbf{\Sigma}^{-1}\,\mathbf{U}^H E_j^e \\ &= \sum_{k=1}^{N_t} V_k \frac{1}{\sigma_k}\,({U_k}^H E_j^e) \end{aligned} \tag{4.7}$$

where N_t is the number of modes defined on the scatterer. In this work, multiple excitations are used to excite specific eigenmodes on the chipless passive RFID tag. The mathematical formulation exploited to obtain a specific total current on the tag is presented in the next section.

4.2.1.2 Surface Current on the Tag using Multiple Excitations

In this section, we demonstrate that the dominant eigenmodes can be selectively excited on the patch by using multiple excitations characterized each by a specific coefficient γ_j. This process assumes that the non-dominant eigenmodes (i.e. with large singular values σ_j) do not contribute significantly to the induced current I_t, and can be omitted.

By definition, the eigenmodes are not related to any kind of excitation; they just depend on the shape and size of the objects [6, 47]. In the previous section, the SVD decomposition on $\mathbf{Z}_t$ has been used to obtain the eigenmodes of the tag. They are ranked according to the increasing singular value. From the matrices $\mathbf{U}$ and $\mathbf{\Sigma}$, we define a matrix $\mathbf{W}$ where the columns of $\mathbf{W}$ represent the "associated eigen-currents" on the tag (t). $\mathbf{W}$ is defined as

$$\mathbf{W} = \mathbf{U}\,\mathbf{\Sigma}^{-1} \tag{4.8}$$

Following the classical SVD decomposition [191] representation, the eigenmodes in $\mathbf{V}$ and the eigen-currents in $\mathbf{U}$ are ordered according to the ascending order of singular values σ_j. Using the definitions (4.7) and (4.8), the total current distribution can be rewritten for any excitation in a compact matrix form:

$$I_{t_j} = \mathbf{V}\,\mathbf{W}^H\,E_j^e \tag{4.9}$$

This indicates that, for a given source dipole d_j, the importance of a given eigenmode is proportional to the projection of the corresponding "associated eigen-current" (column of $\mathbf{W}$) on the excitations described by vector E_j^e.

Let us define a matrix $\mathbf{E}^e$ of size $N_t \times N$ where each column of $\mathbf{E}^e$ corresponds to an excitation vector E_j^e. Writing (4.9) on a mode-by-mode basis for the N_t modes (which is equal to the number of basis functions used to discretize the tag) yields

$$I_{t_j} = \sum_{k=1}^{N_t} \alpha_{k\,j}\, V_k \tag{4.10}$$

$$\boldsymbol{\alpha} = \mathbf{W}^H\, \mathbf{E}^e \tag{4.11}$$

where the matrix $\boldsymbol{\alpha}$ of size $N_t \times N$ is the projection of the columns of $\mathbf{W}$ on the excitations $\mathbf{E}^e$.

If N transmitting antennas are used, we may be able to control N eigenmodes out of the N_t modes defined on the scatterer. To distinguish the N dominant eigenmodes from the others, (4.10) can be rewritten as

$$I_{t_j} = \sum_{k=1}^{N} \alpha_{kj}\, V_k + \sum_{k=N+1}^{N_t} \alpha_{kj}\, V_k \tag{4.12}$$

The first term in (4.12) contains only the eigenmodes to be controlled. If N excitations E_j^e (j = 1 to N) are exploited, we may control the desired eigenmodes by weighting the excitations E_j^e, and hence the port voltages represented by the specific coefficient γ_j of transmitting antennas. The control of eigenmodes is achieved by multiplying the different excitations E_j^e, and hence the currents I_{t_j}, by a specific coefficient γ_j. A desired eigenmode will be excited and the unwanted eigenmodes will be suppressed. From (4.12), a new eigen-current I_{tn} is then obtained from the following combination of modes:

$$\begin{aligned} I_{tn} &= \sum_{j=1}^{N} \gamma_j \left(\sum_{k=1}^{N} \alpha_{kj}\, V_k + \sum_{k=N+1}^{N_t} \alpha_{kj}\, V_k \right) \\ &= F + F_1 \end{aligned} \tag{4.13}$$

where

$$F = \sum_{k=1}^{N} \sum_{j=1}^{N} \gamma_j \, \alpha_{kj} \, V_k = \sum_{k=1}^{N} \mu_k \, V_k \tag{4.14}$$

such that

$$\boldsymbol{\alpha} \, \Gamma = \mu \tag{4.15}$$

where Γ is a vector containing the coefficients γ_j. If only the j^{th} dominant mode is selected, we have $\mu_k = 1$ for $k = j$ and $\mu_k = 0$ for $k \neq j$. Hence

$$\Gamma = (\boldsymbol{\alpha}^{-1})_j \tag{4.16}$$

The Γ corresponds to the j^{th} column of matrix $\boldsymbol{\alpha}^{-1}$. To summarize, the excitations γ (i.e. specific port voltages) allow the excitation of a desired eigenmode and the suppression of a number of unwanted eigenmodes, depending on the number of excitations. One can also excite any linear combination of the desired eigenmodes to obtain the corresponding excitation law Γ.

The neglected eigenmodes contribute to the corresponding residual current, written as

$$F_1 = \sum_{k=N+1}^{N_t} \sum_{j=1}^{N} \gamma_j \, \alpha_{kj} \, V_k \tag{4.17}$$

The residue F_1 is expected to be negligible compared to F, which will be verified in the upcoming example. We discuss the application of the eigenmode methodology via an illustrative example in the next section. Four excitations are used to expand the eigen-current on a chipless passive RFID tag using respective excitation coefficient γ, where a desired eigenmode (or combination of desired eigenmodes) is excited and the unwanted eigenmodes are suppressed.

4.2.1.3 System example

Consider a passive chipless RFID system (Fig. 4.3), where the elements of the system are printed on a multilayered dielectric medium (Fig. 4.2). The tag (scatterer) is a metallic square patch printed on a first dielectric layer (L_1) and the incident waves are obtained from dipole antennas printed on the top of the third dielectric layer (L_3), which are also considered as readers. The field and current on the scatterer are solved using a MoM code developed for multilayered substrates [205]. The proposed chipless passive RFID tag is examined in terms of eigenmodes for a thin lossy dielectric substrate. In this section, we illustrate through simulation results that the tag response can be made specific by independently exciting preselected eigenmodes using multiple excitations. The simulated results are

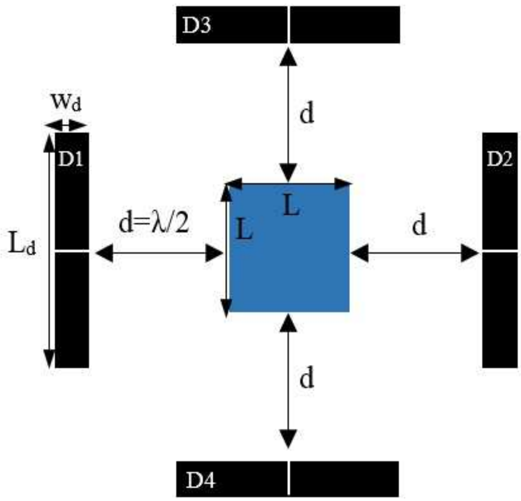

Figure 4.3: Top view of the proposed chipless passive RFID system printed on a multilayered dielectric substrate. L = 2.9 cm is the size of the square patch (printed on first layer), Length of dipoles L_d =3.9 cm (printed on third layer) and width of dipoles w_d = 0.3 cm, $\lambda = 12.29$ cm.

obtained using an in-house MoM code which implements the proposed methodology to analyze the eigenmodes of the scatterer. The tag is excited by four printed dipole antennas (D_1, D_2, D_3 and D_4) resonant at the highest RFID frequency, equal to 2.44 GHz. The tag and antennas are printed on a dielectric substrate of relative permittivity $\epsilon_r = 4.3$ and loss tangent $\delta = 0.02$. For simulation purposes, we consider an infinite dielectric substrate and an infinite ground plane.

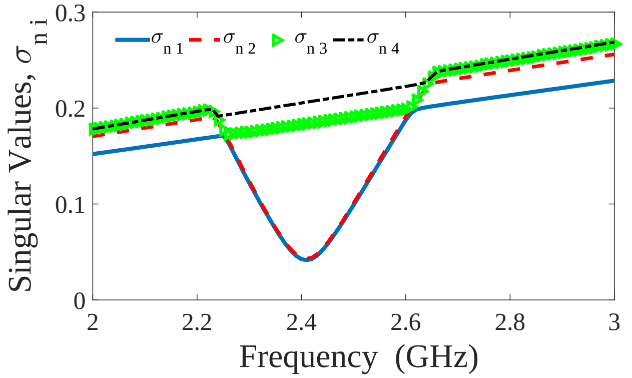

Figure 4.4: The singular values (σ) of the square scatter vs. frequency.

To determine whether a mode is at resonance, its associated singular value is checked to be close to zero. Fig. 4.4 presents the variation of singular values w.r.t. frequency for the first four eigenmodes of a printed tag having a size of 2.9 cm x 2.9 cm and meshed with 343 RWG basis functions [169]. It is observed that the singular values are positive and that some of them are at resonance (σ_i very small and close to zero) near a specific frequency.

From Fig. 4.4, it can be observed that eigenmodes σ_1 and σ_2 resonate at 2.41 GHz, revealing that the dominant eigenmodes are associated to σ_1 and σ_2. Hence, given (4.8) and (4.9), for a non-zero projection of the associated eigen-current W_j on the excitation E_j^e, the first and second eigenmodes are dominant; i.e. they correspond to high induced currents. Simulations have been carried out using a PC with 8 GB RAM and Intel Core i7 $-$ 2640M CPU @ 2.8 GHz. The simulation time required to calculate the singular values and eigenmodes of the tag at the resonant frequency (2.41 GHz) is 19 seconds. Hence, the whole process is computationally cheap. We also use four selective excitations to demonstrate the proposed eigenmode methodology. Every excitation vector is characterized by an excitation coefficient γ_j, which provides a specific amplitude to incident wave j. In this way, the desired combination of eigemodes is selected and the unwanted modes are suppressed. The current distributions of the first two dominant eigenmodes and a combination of them are shown in Table I. As illustrated, the current distribution of the residual eigenmodes has a much lower level than the current distribution of the desired eigenmode when four excitations were used. Therefore, the residual can be considered negligible, while the total current is very close to the desired eigenmode current.

In the next section, we present a near-field beamforming technique using multiple receivers, which allows one to control the sensitivity of the output signal to different eigenmodes.

4.2.2 Eigenmode Analysis for Multiple Receivers

The technique proposed before allows the transmitting antennas to collectively excite some desired eigenmodes and to suppress others not dealt with, through the choice of the amplitude of different incident waves. This was possible under the assumption that residual eigenmodes can be concealed.

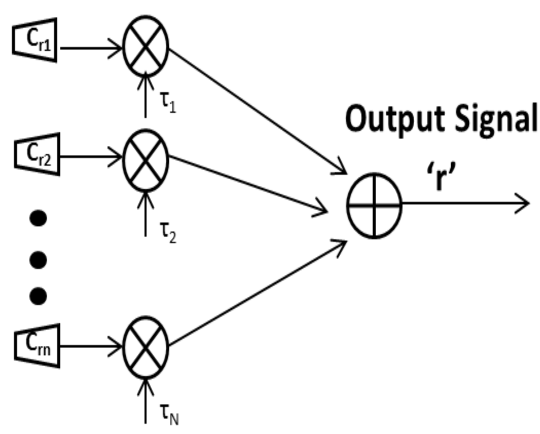

Figure 4.5: A general beamforming system in the receive case.

In this section, we extend the method to the multiple-receivers case, where the dominant eigenmodes are further selected by beamforming the

Table 4.1: current distribution of F, F_1 and I_{tn} at frequency 2.41 GHz.

	Desired Mode (F)	Residue (F_1)	I_{tn}
A) First eigenmode (3 excitations using dipoles; D_2, D_3 and D_4)	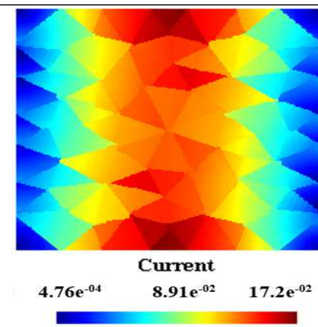	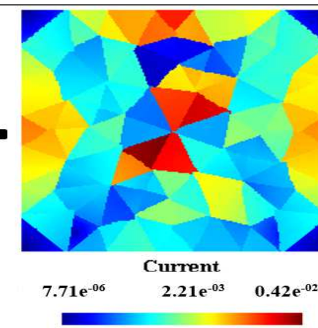	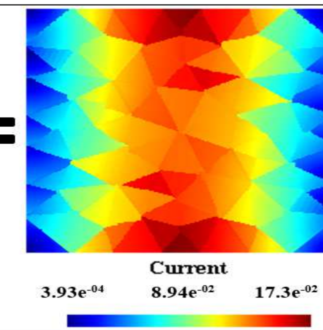
A_1) First eigenmode (2 excitations using dipoles; D_2 and D_4)	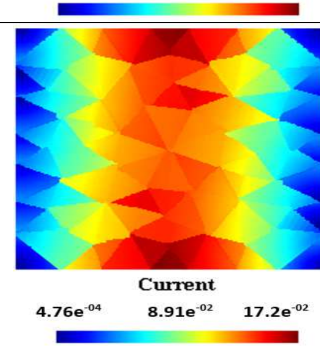	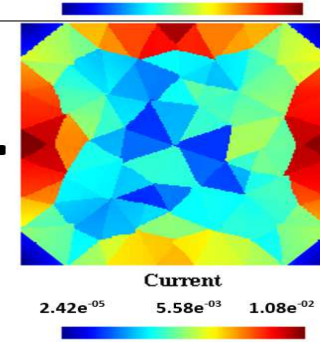	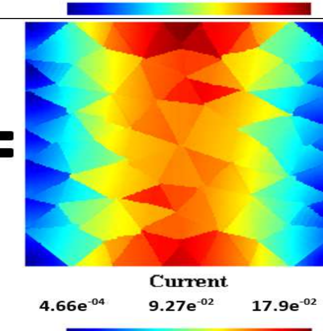

	Desired Mode (F)	Residue (F_1)	I_{tn}
B) Second eigenMode (3 excitations using dipoles; D_1, D_2 and D_3)	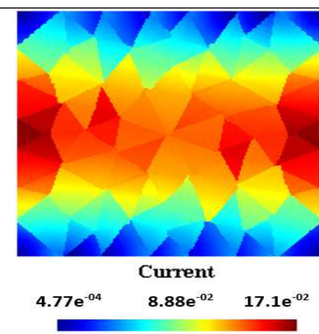	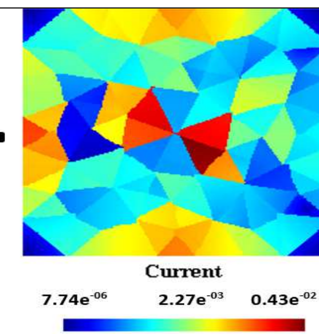	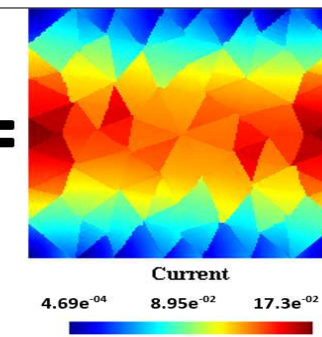
B_1) Second eigenMode (2 excitations using dipoles; D_1 and D_3)	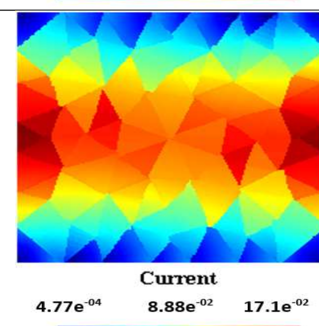	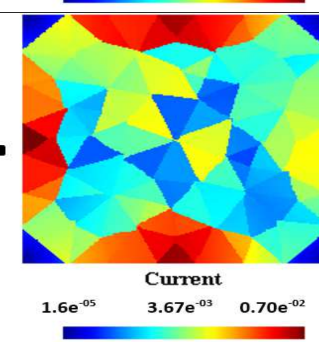	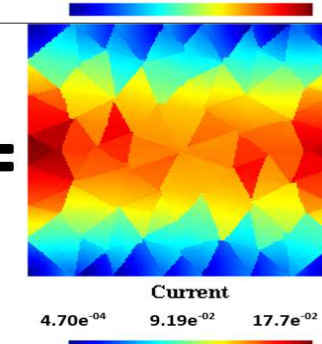

	Desired Mode (F)	Residue (F_1)	I_{tn}
C) Linear combination of first two eigenmodes (3 excitations using dipoles; D_1, D_2 and D_3)	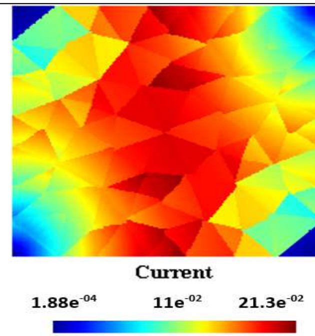	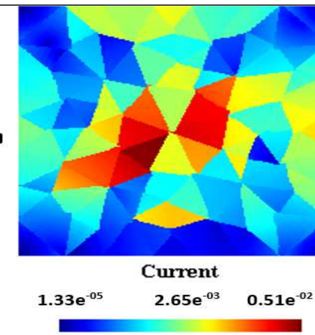	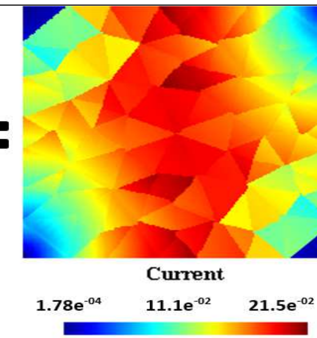
C_1) Linear combination of first two eigenmodes (2 excitations using dipoles; D_1 and D_4)	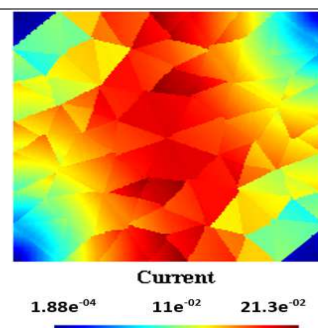	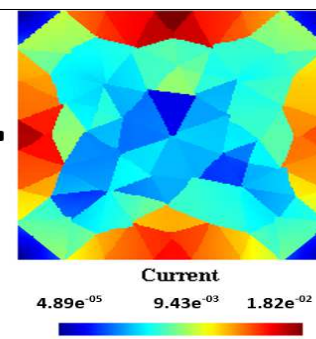	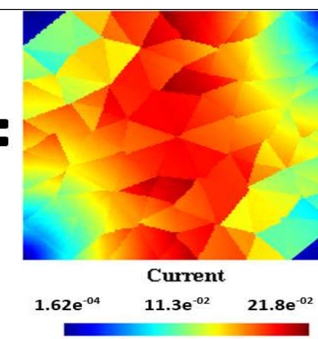

currents received from each receiving antenna, as depicted in Fig. 4.5. From the available dominant eigenmodes, with the extended approach, we extract the response which will be dependent only on the most significant mode. In this way, one can better distinguish the desired tag from the external environment. In other words, the received currents are linearly combined such that the output is only sensitive to the fields radiated by a specific eigenmode. It is then straightforward to extend that to a linear combination of eigenmodes. The other dominant eigenmodes have to be suppressed through the beamformer. This selection is achieved using a specific list of receiver coefficients multiplying the amplitudes of the received currents.

The signal C_{rn} from each element is multiplied with a weight τ_n^*, and the weighted signals are added together to form the output signal r, given by

$$r = \sum_{n=1}^{N} C_{rn}\, \tau_n^* = C_r^T\, T^* \tag{4.18}$$

where T represents the vector of complex weights τ, and C_r represents the received port currents, both of size $N \times 1$. It is worth mentioning here that the received currents can be linked with the current on the scatterer using the reciprocity theorem [206]. The received current [207] C_r is obtained as

$$C_r = \iint \vec{E}_j.\vec{J}\, dS \tag{4.19}$$

where $\vec{J}$ is the eigen-current on the scatterer and $\vec{E}_j$ is the electric field incident on the scatterer from the same antenna when it is transmitting with a unit voltage. Using the above relationship, the received port current related to an eigenmode C_m can be written as

$$C_m = (E_j^r)^T\, V_j \tag{4.20}$$

where V_j is a dominant eigenmode, and E_j^r is the scattered field, which is computed in exactly the same way as E_j^e in (4.5), considering that I_{dj} has been obtained with a source with a unit voltage. If the transmitting antennas are the same as the receiving ones, E_j^r is equal to E_j^e. The received currents on multiple receivers and associated to all the dominant eigenmodes can be written as

$$\mathbf{C} = (\mathbf{E}^r)^T\, \mathbf{V}_N \tag{4.21}$$

where $\mathbf{C}$ is a matrix of size $N \times N$ where each column of $\mathbf{C}$ corresponds to the received port currents C_m associated to a dominant eigenmode. $\mathbf{V}_N$ is the matrix containing the N dominant eigenmodes defined in (4.9) and used in (4.14). The columns of the matrix $\mathbf{E}^r$ are composed of the scattered field vectors E_j^r. Finally, following (4.18), the output signal of the beamformer is obtained by linearly combining the received currents obtained by the N receiving antennas by a specific receiver coefficients τ_n. Then, using the matrix $\mathbf{C}$ defined in (4.21), the response vector (R) related to dominant eigenmodes reads as:

$$R = \sum_{n=1}^{N} \tau_n^* \, (\mathbf{C}^T)_n = \mathbf{C}^T T^* \tag{4.22}$$

such that

$$T = (\mathbf{C}^H)^{-1} R^* \tag{4.23}$$

Suppose that the response R should be one for mode j and zero for other modes, then, similarly to what has been done on transmit, the vector T of receiver coefficients τ_n should be

$$T = ((\mathbf{C}^H)^{-1})_j \tag{4.24}$$

Hence, the vector T is the j^{th} column of matrix $(\mathbf{C}^H)^{-1}$ of size $N \times N$. Then the response depends on the selected desired eigenmode. Meanwhile, the unwanted eigenmodes are suppressed, as long as they are part of the N dominant eigenmodes. It is straightforward to select a linear combination of eigenmodes, by superposition of vectors T.

The eigenmodes approach presented before allows the excitation of a limited number of selected eigenmodes, via multiple excitations on the scatterer. Also, a similar selection of eigenmodes could be operated on receive where a desired eigenmode or combination of eigenmodes was filtered by suppressing the unwanted eigenmodes. In the next section, the proposed method is experimentally validated.

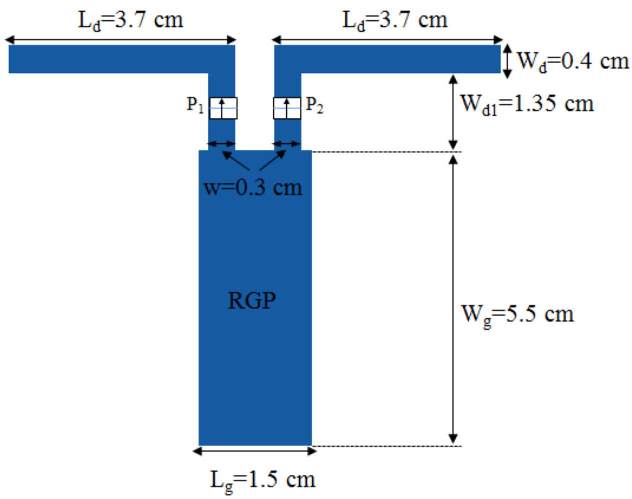

Figure 4.6: Printed dipole antenna with double feed point.

4.3 Experimental Setup and Results

In the previous section, we explained how a multi-antenna RFID system allows the extraction of responses that depend on specific eigenmodes. In this section, a possible implementation for such a system is described.

4.3.1 Experimental Setup

An initial validation is described, considering a very simple scatterer and just two antennas acting as transmitter and receiver. The scatterer is a square metallic patch with size L, as presented in Fig. 4.3. It is printed on the first layer L_1 with FR4 substrate (relative dielectric constant $\epsilon_r = 4.3$, loss tangent $\delta = 0.02$ and thickness, $h_1 = 0.32$ cm) backed by a ground plane (Fig. 4.2). The tag is excited by two printed dipoles placed at the distance of $d_1 \cong 15$ cm ($\geqslant \lambda + L$) and printed on layer L_3 (Fig. 4.7.a). Each dipole antenna has good matching within 2.4 GHz to 2.483 GHz (SHF band for RFID) as presented in next section. The first and third layers are separated by an air gap of 3 cm thickness. To be able to use the printed dipoles as the sources of excitations, the height of the dipoles above the ground plane is chosen in such a way that they can be matched [208]. Here, a new design (Fig. 4.6) for the printed dipole has been proposed using a finite rectangular metallic ground plane (RGP) of size $L_g \times W_g$ connected to the dipole. The dipoles are fed with two coaxial cables, where the outer conductor of each cable is connected to the ground plane. Each dipole has two ports to balance the antenna without using a balun circuit which may limit the bandwidth of the experiment. Simulations have been carried out using both the in-house MoM code and the commercial software IE3D [5]. Fig. 4.7.a shows the three-dimensional view of the prototype generated with the IE3D software, and the top view of the system. Dipole 1 is excited by the ports 1 and 2 and dipole 2 by ports 3 and 4, as presented in the bottom picture of Fig. 4.7.a. Fig. 4.7.b shows the realized prototype, with the substrate of dimension 31 cm $\times$ 21 cm.

In order to validate the numerical analysis of the array and passive tag, the scattering matrix (**S**) has been measured using a four-port vector network analyzer VNA PNA-X 26.5 GHz, in the anechoic chamber of the ICTEAM Institute. The calibration has been carried out at the end of a coaxial cable. The end of the cable has first been soldered to an SMA coaxial connector, whose output becomes the reference plane for calibration. However, later, the cable has been directly soldered to the source port of the printed dipole, as illustrated in Fig. 4.7.b. In this case, a small error in the phase of the extracted reflection coefficient data produces a large shift in the admittance parameters. We used the technique described in [209] to correct the phase shift and the effect of the SMA connector in measurement results.

The results presented in the next section relate to a preliminary validation of the developed MoM code by means of near-field beamforming on transmit and on receive, using two dipoles (each dipole excited by two ports), and the technique to correct the phase shift in measurement results. Next sections explain, both through simulation and measurement, how the responses from different eigenmodes can be extracted. An essential quantity for this operation corresponds to an admittance matrix of the system.

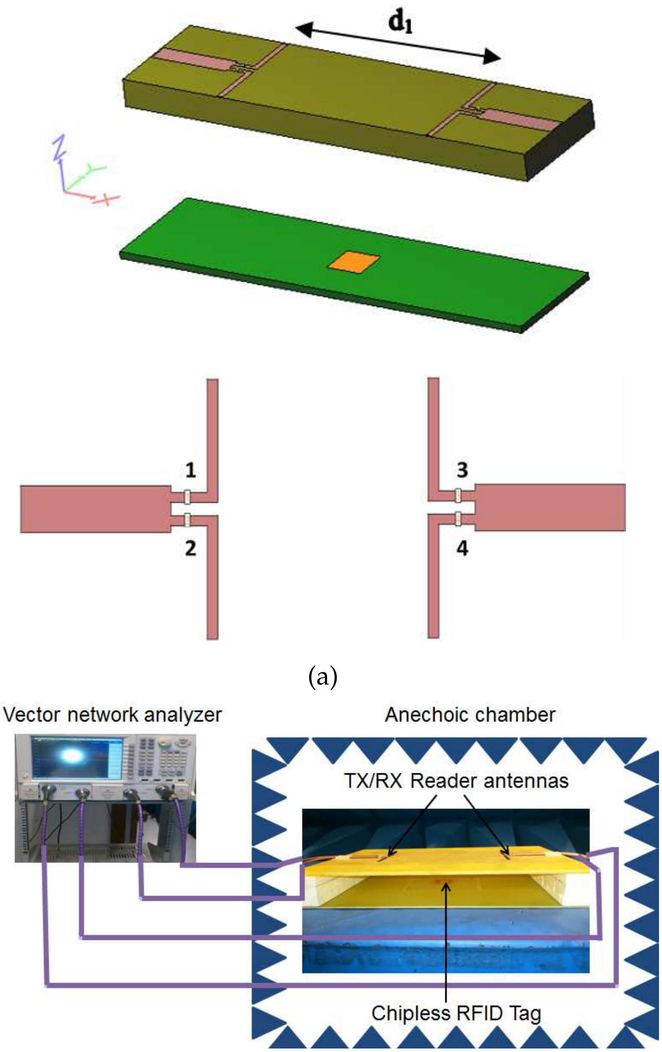

Figure 4.7: Prototype system design: (a) 3D and top view, and (b) chipless RFID tag experiment: block diagram and photograph.

4.3.2 Numerical Analysis and Experimental Results

As explained in Section 4.2, the transmitting array is excited by voltage sources and the received current is observed at the ports of the receiving array, which can correspond to the transmitting one. Hence, the admittance matrix representation of the system will be considered.

The admittance matrix of the system, represented as $\mathbf{Y}_s$, seen as a four-port network, can be obtained from the MoM matrix $\mathbf{Z}_{tot}$ detailed in (4.3). The four-port admittance matrix is found from the MoM admittance matrix ($\mathbf{Y}_{tot} = \mathbf{Z}_{tot}^{-1}$) by selecting the rows and columns with indices corresponding to the basis functions that overlap the delta-gap sources:

$$Y_s\,(i,j) = -w^2\, Y_{tot}\left(nbf_i, nbf_j\right) \tag{4.25}$$

where nbf_i and nbf_j are the indices of feed's basis functions, and w is the width of the feed basis functions, taken normal to current flow. The four-port admittance matrix $\mathbf{Y}_s$ is computed for two different cases: first, when the system includes the tag and, second, without the tag. In order to distinguish the effect of the tag, the difference between mutual admittances of the system, where the tag is printed, or not, has been computed. Given that the printed patch only represents a small scatterer, the difference step may enhance measurement noise or numerical inaccuracies. That difficulty represents a challenge inherent to passive chipless RFID technology. Besides, to avoid the use of balun circuits, each antenna has been fed with two coaxial transmission lines, it is necessary to characterize the symmetrical balanced antenna admittance. Details are recalled in Appendix B regarding the way to obtain the differential admittance matrix of system, represented as $\mathbf{Y}_d$, seen as a two-port network, from the four-ports admittance parameters.

Differential admittance parameters are obtained assuming a differential excitation of each dipole. The way in which those parameters are obtained from a system with two ports per dipole is recalled in Appendix B. The differential admittance parameters shown in Fig. 4.8; they have been obtained from simulation and measurement (after solving the problem of the phase shift and the SMA connector effect, as explained in Section 4.3.1) of the system in the presence of the scatterer.

The resonance of the antennas associated to different eigenmodes of the tag is extracted using the differential admittance matrix of the system.

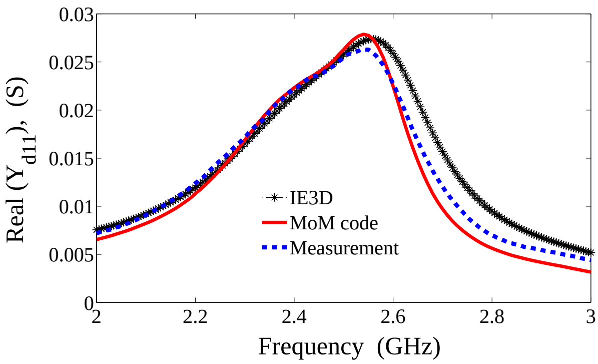

(a)

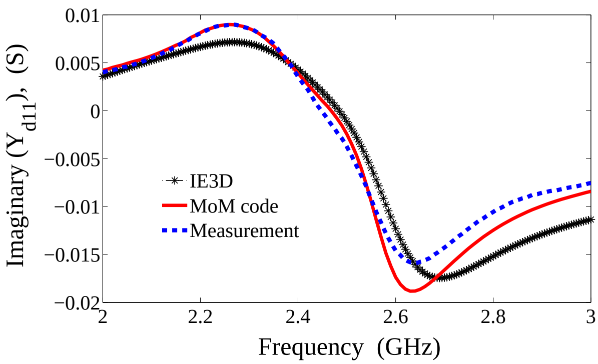

(b)

Fig. 4.9 presents the simulated return loss S_{11} using the developed code, where the full system is discretized with 969 RWG [169] basis functions, and IE3D. In the same figure, an experimental validation of the techniques presented above is shown. Fig. 4.9 shows that the resonant frequency of each printed dipole is at 2.44 GHz considering a return loss $|S_{11}| < 10$ dB in the presence of the patch and dipoles. One can see that the dipole antenna has a bandwidth (BW) that spans from 2.24 GHz to 2.59 GHz, which can cover the SHF band for RFID.

The resonance is well represented and those results validate the developed MoM-code for the chipless passive RFID system implemented for multilayered dielectrics media.

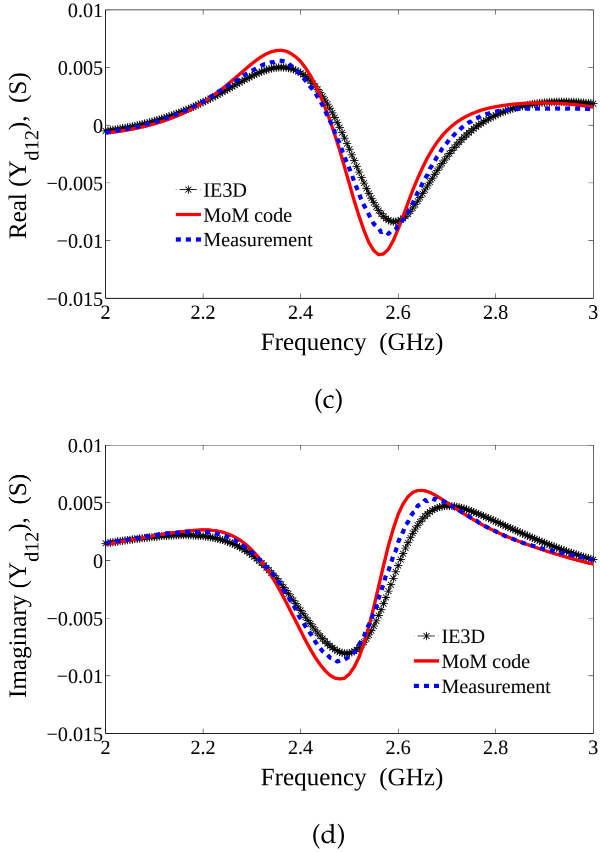

Figure 4.8: Comparison of differential admittance parameters $Y_{d_{ij}}$ after balancing of antennas and de-embedding of system, according to in-house MoM code, IE3D and measurement.

To distinguish the effect of the square patch inside the chipless passive RFID system, the difference between mutual differential admittance parameter, Y_d, in the presence of the tag, and Y_{dw}, in its absence, is calculated. This difference is termed hereafter as "additional" admittance. The comparison between simulation and measurement of this difference is presented in Fig. 4.10. Although one speaks about small differences between large values, this result compares relatively well with some discrepancies. These differences can be attributed to numerical errors and to the limited

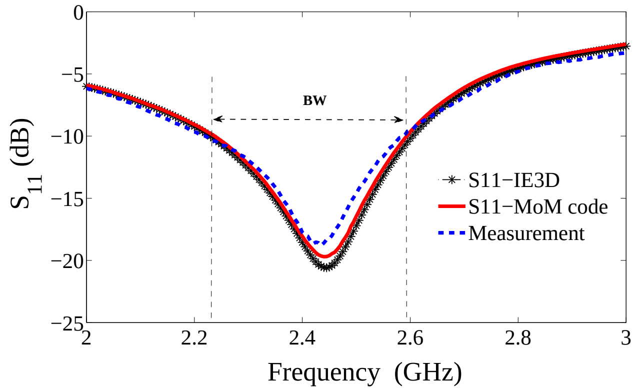

Figure 4.9: Reflection coefficient S_{11} for simulation (MoM-Code, IE3D) and measurement results.

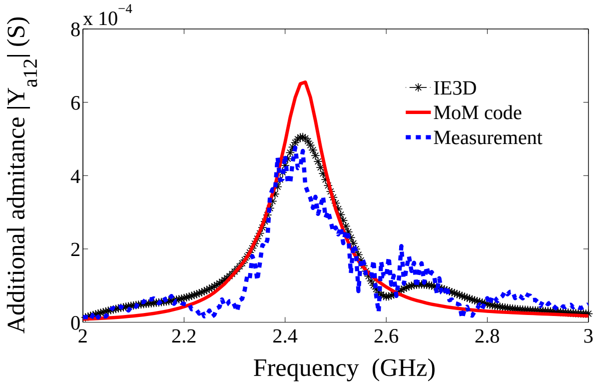

Figure 4.10: Comparison of the difference between mutual admittance (system with or without scatterer) using MoM-code, IE3D and Measurement.

accuracy of positioning of the different physical components. Moreover, the accuracy challenge is related to background subtraction recalled here, which is inherent to chipless passive RFID. From Fig. 4.10, we see that the tag has a clearly consistent signature. The same code is used below to extract the response associated to different eigenmodes of the tag.

4.3.3 System Responses

The response r of the proposed passive tag presented in Section 4.2 before background extraction (4.18), is characterized by the controlled excitation of specific dominant eigenmodes. As explained there, r is obtained by beamforming on transmit with voltage coefficients γ_j (4.16) and by combining the received currents with coefficients τ_n (4.24). The received port current (4.20) can be rewritten, in presence of the tag, as

$$C_m = \mathbf{Y}_d \, \Gamma_m \tag{4.26}$$

and in absence of the tag, as

$$C_{mw} = \mathbf{Y}_{dw} \, \Gamma_m \tag{4.27}$$

where Γ_m is the vector containing the voltage coefficients associated to the selected mode. From (4.18), (4.26) and (4.27), the response of the tag after background subtraction, represented as r^e, is obtained as

$$r^e = T^H \left(C_m - C_{mw} \right) = T^H \, \mathbf{Y}_a \, \Gamma_m \tag{4.28}$$

where $\mathbf{Y}_a$ is the difference between the differential admittance matrix $\mathbf{Y}_d$ (in presence of tag) and $\mathbf{Y}_{dw}$ (in absence tag):

$$\mathbf{Y}_a = \mathbf{Y}_d - \mathbf{Y}_{dw} \tag{4.29}$$

This matrix describes the effect of the patch on the N-port system (background extraction). That is why we name that matrix below as "additional" admittance matrix $\mathbf{Y}_a$. As shown in Appendix B, assuming that the primary currents on the dipoles are not impacted by the presence of the patch ("backward" interaction neglected), the "additional" admittance matrix $\mathbf{Y}_a$ can be approximated as

$$\mathbf{Y}_a = \mathbf{E}^{r\,T} \, \mathbf{Y}_t^{-1} \, \mathbf{E}^e \tag{4.30}$$

where $\mathbf{E}^r$ and $\mathbf{E}^e$ are the scattered and incident field matrices, respectively. Here, $\mathbf{E}^r$ is equal to $\mathbf{E}^e$ since the same antennas are used on transmit and on receive, and they are obtained from (4.5). $\mathbf{Y}_t = \mathbf{Z}_t^{-1}$ ($\mathbf{Z}_t$ has been defined in (4.1)) represents the tag (t) self-interactions. The response r^e has been obtained through the "additional" admittance matrix $\mathbf{Y}_a$ obtained from the approximation (4.30) for the in-house MoM code, and from (4.28) for IE3D and measurements. As explained in Section 4.2, the specific coefficients γ_j and τ_n allow the selection on transmit and receive of specific eigenmodes, which should lead to distinct frequency responses.

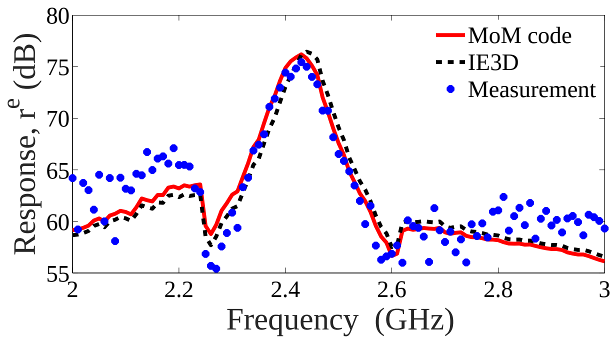

(a)

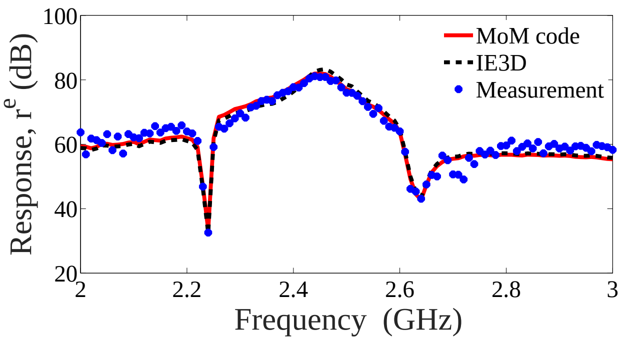

(b)

Figure 4.11: Comparison of the response r^e using MoM code, IE3D and Measurement, related to the selected modes; (a) first eigenmode and (b) second eigenmode.

The response r^e versus frequency f related to the wanted modes of the tag is studied over a wide frequency band, using the formulation (4.28).

Fig. 4.11 presents a comparison for the response r^e obtained with the developed MoM code, the commercial IE3D software and measurements. Fig. 4.11.a shows the response r^e when the first mode is selected, while the second one is suppressed. Similarly, the response related to the second mode is presented in Fig. 4.11.b. The responses r^e compare well when the first eigenmode is considered and the second one is suppressed (Fig. 4.11.a), i.e $r^e(f)$ are similar for simulations (in-house MoM code and IE3D) and measurements over the frequency band where the antenna is matched with a $S_{11} < -10$ dB (2.24 to 2.59 GHz, see Fig. 4.9). For the second eigenmode (Fig. 4.11.b), while shapes are similar inside the band for the in-house MoM code, IE3D and measurements, the absolute levels of the responses obtained from simulations and measurements match within small differences. Those differences are mainly due to the challenge of background subtraction which amounts to take the difference between large and close matrices, to obtain the "additional" admittance matrices $\mathbf{Y}_a$. Also, this difference stems from the discretization of the structure carried out differently in our MoM code and with the IE3D software, as well as from the inaccuracy associated to the soldering of the feeds. The two frequency responses of the tag inside the proposed chipless passive RFID system are very distinct, and they are clearly different over the frequency band, when the first dominant eigenmode or the second dominant eigenmode is excited (Figs. 4.11.a and 4.11.b, respectively). The difference between the responses is visible, also inside the SHF band (2.4 GHz to 2.483 GHz) for RFID. Fig. 4.11 shows discontinuities in the responses of the tag, which are attributed to the swapping between dominant modes at specific frequencies and the next. This means that the index of a given mode, which reflects the ranking of its singular value, can change at specific frequencies.

The proposed method has been demonstrated on another example, a rectangular patch. The size of the tag is 2.4 $\times$ 2.9 cm, discretized with 234 triangular RWG basis functions. The simulations, using the in house MoM code and IE3D, have been carried out from 2 GHz to 3 GHz.

The first eigenmode on the rectangular tag is the dominant eigenmode inside the frequency band 2.27 - 2.69 GHz, noting that the importance of a dominant eigenmode results from its singular value σ_j. Inside and out-

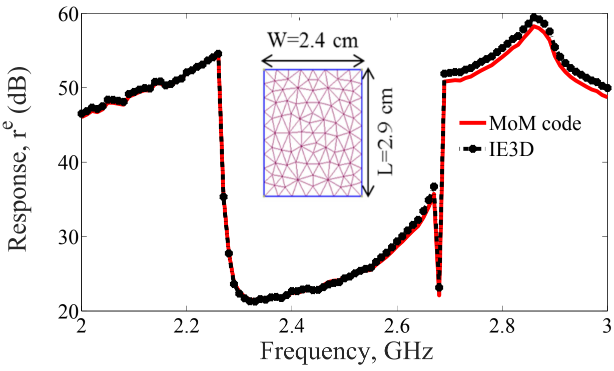

(a)

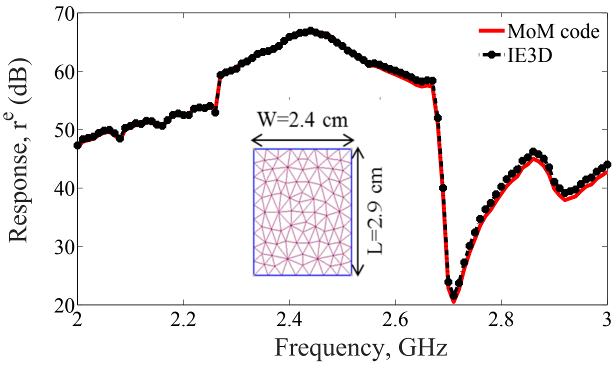

(b)

Figure 4.12: Comparison of the response *r* of the rectangular tag using MoM code and IE3D related to the selected modes, (a) first eigenmode (the dominant), and (b) second eigenmode.

side that band, the first eigenmode (with the smallest singular value) corresponds to a fundamentally different current distribution. Fig. 4.12.a shows a first sudden change, at 2.26 GHz, in the response for the first selected eigenmode, arising from the appearance of a new first dominant mode with the smallest singular value. A second change at frequency 2.67 GHz is shown in Figs. 4.12.a and b, resulting from the switching between the two dominant eigenmodes index, and the first mode becoming cross-polar to the excitation. The unstable modes versus frequency is a popular problem in modal analysis [210, 211]. The responses from the rectangular tag are very distinct from each other (Figs. 4.12.a and b), they can be also clearly distinguished from the square's response.

4.3.4 Alignment of Tag

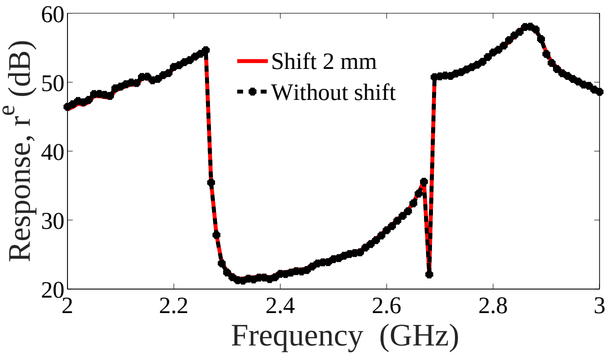

(a)

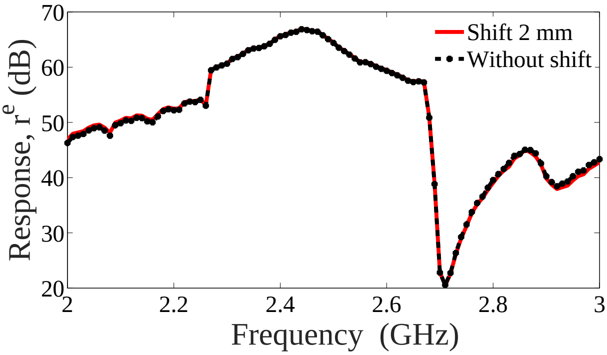

(b)

Figure 4.13: Comparison between responses of the tag without and with offset of 2 mm in X direction. a) Response related to first dominant eigenmode, and b) Response of the tag associated to second eigenmode.

We explain above that the computed responses of a tag (using our methodology) are based on the choice of the excitation coefficients and receiver coefficients. Also, the alignment has an effect on the response of the tag.

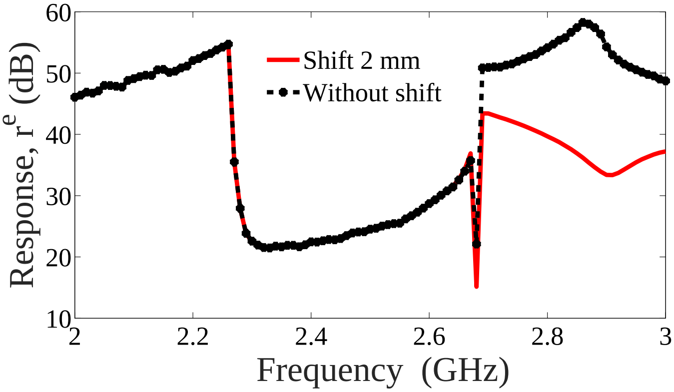

(a)

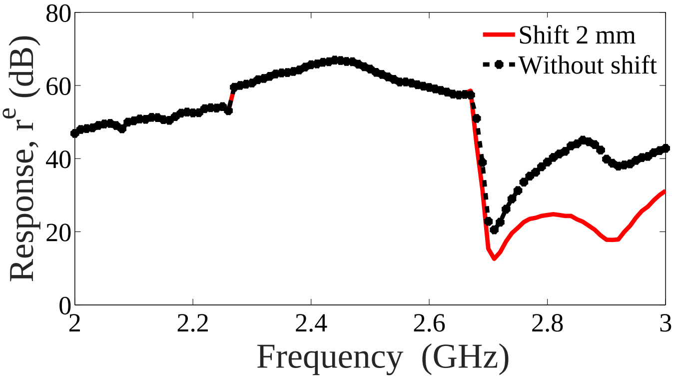

(b)

Figure 4.14: Comparison between responses of the tag without and with offset of 2 mm in Y direction. (a) Response related to first dominant eigenmode, and (b) Response of the tag associated to second eigenmode.

To quantify this, a simulation, using the developed code, has been carried out for frequency band 2-3 GHz.

Figs. 4.13 and Figs. 4.14 present a comparison between the responses from the rectangular tag presented in Fig. 4.12 and the responses when the alignment is slightly offset by 2 mm ($\approx \frac{\lambda}{62}$) in X (Figs. 4.13) and Y (Figs. 4.14) directions. We believe that it is easy to align the tags with 2 mm. Figs. 4.13.a and 4.14.a present the responses related to the dominant eigenmode, when the second one is suppressed. Figs. 4.13.b and 4.14.b show the frequency responses r^e from the tag when the second mode is selected. The responses compare well when the alignment is offset in X direction (Fig. 4.13). Fig. 4.14) shows a change in the frequency responses above 2.7 GHz, when the tag is shifted in the Y direction. We verified that this results from the swapping between modes and the position of the voltage sources. Inside the SHF band for RFID (i.e. between 2.4 and 2.483 GHz), the responses from the tag essentially remain independent from the alignment of the tag for a shift smaller than $\frac{\lambda}{25}$ (close to 5 mm) in X and Y directions.

Nevertheless, the alignment remains an important criterion while studying a chipless passive RFID. Therefore, we may propose a solution to this problem in future work, where the measurements could be carried out with slightly different offsets, as the tag is passing by.

4.4 Conclusion

An eigenmode approach has been proposed to analyze a chipless passive RFID tag printed on a thin dielectric layer. It allows the selection of specific eigenmodes of the scatterer using transmit and receive beamformers, which in turn enables the extraction of the specific signatures associated with the dominant eigenmodes. These frequency responses provide independent signatures for the same scatterer, allowing the user to better distinguish it from other scatterers, and to improve the independence from the environment.

First, the eigenmodes of the tag have been studied through the SVD decomposition of the MoM impedance matrix of the scatterer. Then, the eigenmodes are classified according to their increasing singular values. The projection process of incident waves on the "associated eigen-currents" are studied to allow the extraction of specific modes of the tag and the suppression of unwanted ones, both on transmit and receive. This has been carried out through the definition of specific beamforming coefficients for the transmitting and receiving arrays placed in the near-field. It was produced from selecting the modes to be excited based on their singular values, and from a study of their projections on the excitations. This methodology has been validated through the study of a chipless passive RFID tag using an in-house MoM code, the IE3D software and a prototype. In all cases, the effect of the scatterer has been studied from the "additional" mutual impedance matrix, obtained after background extraction. The proposed eigenmode approach allows the production of responses associated with each eigenmode separately. The responses of the tag have been studied based on both simulations and measurements and they have clearly distinct frequency responses. Responses from different tags are also clearly distinct.

This work will be extended through the use of a larger number of excitation/receivers to select other specific eigenmodes, as well as considering a wide variety of shapes for the scatterer. Tracking algorithms to improve the stability of eigenmodes versus frequency will also be investigated.

Extended SVD−Eigenmode Approach for Selective Excitation of Scatterers with Complex Structures

5

5.1 Introduction

A design methodology for chipless RFID tags is proposed in the Chapter 2. The proposed tags can be used to secure the system by considering a special tag based on a natural complex geometry. A particular electromagnetic response is extracted from the printed antenna based on the complex irregular shape. Then, the patch can be used such as a chipless RFID tag, which is difficult to produce or to duplicate (cloning) thanks to the complex form. On the other hand, Chapter 4 proposed the eigenmodes analysis method based on the SVD decomposition to exploit particular frequency responses from a printed chipless passive RFID tag on a thin lossy dielectric substrates backed by a ground plane. The proposed eigenmodes technique leads to the extraction of a unique signature of the tag. In the present chapter, we extend the SVD-eigenmodes technique proposed in the Chapter 4 using a new definition of the eigenmodes of the scatterer based on a new scalar product able to better represent the interaction between physical currents. The modified SVD-eigenmodes method implemented here contributes to answering the challenge related to the discrimination of the scatterer's response with respect to that of the environment and the extraction of specific information resulting from specific shapes for the scatterer. The modification of the technique is critical to extending the SVD-eigenmodes approach to more complex structures such as the irregular fractal shape. This extension of the approach described below can also be a solution for the limitations presented in the previous chapter. Indeed, the numerical results presented in the previous chapters are strongly affected by the discretization of the structure and by the instability of modes versus the frequency band. The effect of the structure's mesh on the results is studied, and the Gram matrix [71] associated to the Rao Wilton Glisson (RWG) [169] basis functions is included in the calculation.

This chapter is organized as follows. In Section 5.2, we start with the proposed reformulation of the SVD-eigenmodes method based on a new definition of the eigenmodes, using an alternative diagonalization of the MoM impedance matrix $\mathbf{Z}_s$ of the scatterer. The factorization of $\mathbf{Z}_s$ is obtained in the form of an SVD decomposition for which the right and left matrices are orthogonal with a new inner product that involves the Gram matrix. As we will see, the validation results confirm the engineering accuracy of the implemented extended approach. Numerical examples that exploit the frequency responses from some scatterers with different shapes (simple and fractal) are presented in Section 5.3, using the arrays presented in the Chapter 4, where transmitters and receivers are placed in the near-field. On the other hand, we proved that the responses of the scatterers associated to the selective eigenmodes are clearly distinct using a larger number of excitations and receivers to select other specific eigenmodes.

5.2 Gram-SVD-Eigenmodes Approach

In order to understand the fundamental physical behavior of the radiating structures, several advanced modal techniques are presented in this thesis. The SVD-eigenmodes approach is the easiest and probably the most useful modal representation, as demonstrated in the Chapter 3, to exploit the current distribution on the surface of a scatterer printed on a lossy dielectric substrate backed by a ground plane considering near-field excitations. In the following section, we extended the SVD-eigenmodes formulation to include a better physical definition of the scalar product between the currents. Based on that scalar product, the orthogonality between a pair of continuous current distribution will be better enforced, given a specific discretization of the surface. This will involve a Gram matrix named here **G**. It is a matrix with entries that are inner products between basis functions and is invertible.

The physical orthogonality between the surface current densities $\bar{J}_i$ is obtained by setting to zero the following scalar product

$$S_p = \int_S \bar{J}_i^* \, \bar{J}_j dS \tag{5.1}$$

As explained in the Chapter 3, the surface current density $\bar{J}_i$ on the surface of a scatterer is defined as

$$\bar{J}_{i/j} = \sum_{n=1}^{N} x_{i/j\,n} \, \bar{f}_{b\,n} \tag{5.2}$$

where $x_{i\,n}$ and $x_{j\,n}$ are the unknown current coefficients (see Section 3.2.3) and $\bar{f}_{b\,n}$ is a vector basis function. Using equation (5.2), the scalar product (5.1) can re-written as

$$S_p = \iint_S \sum_{n=1}^{N} \sum_{m=1}^{N} x_{i\,n}^* \, \bar{f}_{b\,n}^* \, x_{j\,m} \, \bar{f}_{b\,m} dS \tag{5.3}$$

Then

$$S_p = \sum_{n=1}^{N} \sum_{m=1}^{N} x_{i\,n}^* \, x_{j\,m} \iint_S \bar{f}_{b\,n}^* \, \bar{f}_{b\,m} dS \tag{5.4}$$

where N is the number of vector basis functions.

The current vector I usually contains all coefficients $x_{i\,n}$ to determine an approximation for electric current density $\bar{J}_i$ with a projection orthogonality equation. We propose here to construct the corresponding Gram matrix $\mathbf{G}$. Its elements $G_{n,m}$ are obtained by evaluating the inner products between the $n-th$ vector basis function with the $m-th$ basis vector in accordance with the ordered set of basis functions:

$$\mathbf{G}_{n\,m} = \int\!\!\int_S \bar{f}^*_{b\,n}\,\bar{f}_{b\,m} dS \quad \text{then} \quad G_{nm} =< \bar{f}_{b\,n}, \bar{f}_{b\,m} > \tag{5.5}$$

where $\mathbf{G}$ is a real symmetric and positive semi-definite matrix. From definitions (5.1) and (5.5), the scalar product between the surface current densities $\bar{J}_i$ is approximated as

$$S_p \cong {x_i}^H \mathbf{G}\, x_j \tag{5.6}$$

then the physical orthogonality between the current densities is obtained by setting to zero the scalar product ${x_i}^H \mathbf{G}\, x_j$.

Assuming a complex dimensional Hilbert space [212], it can directly be appreciated by realizing that $\mathbf{G}$ in this space can be written as the product of a matrix with its Hermitian conjugate using the Cholesky factorization [192]:

$$\mathbf{G} = \mathbf{A}^H\,\mathbf{A} \tag{5.7}$$

equivalent to the orthogonality condition:

$$(\mathbf{A}^{-1})^H\,\mathbf{G}\,\mathbf{A}^{-1} = \mathbf{I} \tag{5.8}$$

where $\mathbf{A}$ is an upper triangular matrix with positive diagonal elements and $\mathbf{I}$ denotes the unit matrix. In the previous chapter, the current distribution I_s on the scatterer for an excitation E^e is represented in the following form, after applying the SVD decomposition to the MoM impedance matrix $\mathbf{Z}_s$ of the scatterer

$$I_s = (\mathbf{Z}_s)^{-1}\,E^e = \mathbf{V}\,\Sigma^{-1}\,\mathbf{U}^H\,E^e \tag{5.9}$$

Then, the current I_s can be represented using the scalar product $\langle \mathbf{P}, \mathbf{P} \rangle = \mathbf{P}^H\,\mathbf{P} = \mathbf{I}$ with $\mathbf{P}$ is a matrix, in the form

$$\langle \mathbf{V}, I_s \rangle = \Sigma^{-1}\,\langle \mathbf{U},\, E^e \rangle \tag{5.10}$$

The reformulation of SVD-eigenmodes approach consists of basis transformation of $\mathbf{Z}_s$ matrix through a new diagonalization method. To this end, the eigenmodes of a structure and the *associated eigen-vectors* are redefined according to a scalar product based on the well-conditioned Gram matrix, which we will name G-orthogonality, written as

$$\langle \mathbf{P}, \mathbf{P} \rangle_G = \mathbf{P}^H \, \mathbf{G} \, \mathbf{P} = \mathbf{I}. \tag{5.11}$$

This section gives another representation of I_s according to the proposed inner product (5.11). Hence I_s can be re-written as

$$\langle \mathbf{V}_n, I_s \rangle_G = \Sigma_n^{-1} \, \langle \mathbf{U}_n, \, E^e \rangle_G \tag{5.12}$$

where $\mathbf{U}_n$ and $\mathbf{V}_n$ are new orthogonal matrices according to the new scalar product (5.11), and $\mathbf{\Sigma}_n$ is a diagonal matrix. Those matrices were defined by a new diagonalization process of the $\mathbf{Z}_s$ matrix, which is presented in the following part of this section.

5.2.1 Diagonalization process of MoM impedance matrix

In this section, we would like to solve the MoM system of equations (5.9) with I_s directly decomposed into eigenmodes V_n satisfying the following orthogonality: $\mathbf{V}_n^H \, \mathbf{G} \, \mathbf{V}_n = \mathbf{I}$.

A first attempt consists of performing an SVD-Type decomposition of $\mathbf{Z}_s$ with U and V matrices orthogonal according the new scalar product (5.11) but this did not lead to a result directly providing the coefficients of I_s in the $\mathbf{V}$ basis. This is why the initial problem (5.9) has been replaced by an equivalent one in the form:

$$\mathbf{Z}_s \, I_s = \mathbf{S}_n \, \mathbf{G} \, I_s = E^e \qquad \text{i.e. with} \qquad \mathbf{S}_n = \mathbf{Z}_s \, \mathbf{G}^{-1} \tag{5.13}$$

Then, the matrix $\mathbf{S}_n$ is decomposed into

$$\mathbf{S}_n = \mathbf{U}_n \, \mathbf{\Sigma}_n \, \mathbf{V}_n^H \tag{5.14}$$

with $\mathbf{V}_n$ and $\mathbf{U}_n$ satisfying the G-orthogonality. From (5.13), we observe that the new problem entails a direct projection of I_s onto the new eigen-

modes defined by the columns of the matrix $\mathbf{V}_n$ through the $\mathbf{V}_n^H\, \mathbf{G}\, I_s$ operation.
Hence, from (5.13) and (5.14), the new system of equations becomes

$$\mathbf{U}_n\, y = E^e \tag{5.15}$$

with

$$y = \mathbf{\Sigma}_n\, \mathbf{V}_n^H\, \mathbf{G}\, I_s \tag{5.16}$$

Multiplying the left and right sides of equation (5.15) by $\mathbf{U}_n^H\, \mathbf{G}$, we obtain

$$y = \mathbf{U}_n^H\, \mathbf{G}\, E^e \tag{5.17}$$

Besides, it can be easily verified from (5.16) that

$$I_s = \mathbf{V}_n\, \mathbf{\Sigma}_n^{-1}\, y \tag{5.18}$$

is an acceptable solution.

Hence, the current I_s can be represented for any excitation in a compact matrix form

$$I_s = \mathbf{V}_n\, \mathbf{\Sigma_n^{-1}}\, \mathbf{U}_n^H\, \mathbf{G}\, E^e \tag{5.19}$$

which can be explicitly expressed in terms of the eigenmodes (columns of $\mathbf{V}_n$) based on the newly defined scalar product (5.11):

$$I_s = \sum_{k=1}^{N_s} V_{n\,k}\, \frac{1}{\sigma_{n\,k}}\, \langle U_{n\,k}, E^e \rangle_G \tag{5.20}$$

where N_s is the number of modes defined on the scatterer. Similar to the SVD-eigenmodes approach, this method allows us to define the coefficient that depends on the incident field with respect to the *associated eigen-vectors* $U_{n\,k}$ from the scalar product $\langle U_{n\,k}, E^e \rangle_G$. To implement decomposition (5.20), one has to answer an important remaining question: how can we perform decomposition (5.14), keeping in mind that $\mathbf{V}_n$ and $\mathbf{U}_n$ must be orthogonal with respect to a new scalar product ?

The modification of the SVD-eigenmodes approach based on the determination of an alternative decomposition to SVD of the matrix $\mathbf{S}_n$ w.r.t. to the inner product (5.11). In the remainder of this section, we present a methodology to define the diagonal matrix Σ_n and the orthogonal matrices $\mathbf{V}_n$ and $\mathbf{U}_n$. As a first step, let us multiply the left hand side of equation (5.14) by the matrix $\mathbf{A}$ and the other side by $\mathbf{A}^H$ using the definition (5.7).

$$\mathbf{A}\,\mathbf{S}_n\,\mathbf{A}^H = \mathbf{A}\,\mathbf{U}_n\,\mathbf{\Sigma}_n\,\mathbf{V}_n^H\,\mathbf{A}^H \tag{5.21}$$

where the left expression corresponds to a matrix $\mathbf{D}$ of same size as the MoM impedance matrix $\mathbf{Z}_s$. We propose to factorize $\mathbf{D}$ using the traditional SVD decomposition

$$\mathbf{D} = \mathbf{U}_D\,\mathbf{\Sigma}_D\,\mathbf{V}_D^H \tag{5.22}$$

where $\mathbf{\Sigma}_D$ is a diagonal matrix that contains real singular values σ_{Dj}. $\mathbf{U}_D$ and $\mathbf{V}_D$ are orthogonal matrices. The columns of $\mathbf{V}_D$ and $\mathbf{U}_D$ are given in the ascending order of corresponding singular values. Comparing equations (5.14) and (5.22), we obtain

$$\mathbf{U}_D = \mathbf{A}\,\mathbf{U}_n \tag{5.23}$$

$$\mathbf{V}_D = \mathbf{A}\,\mathbf{V}_n \tag{5.24}$$

$$\text{and} \qquad \mathbf{\Sigma}_n = \mathbf{\Sigma}_D \tag{5.25}$$

It can then be verified [1] that $\mathbf{U}_n$ and $\mathbf{V}_n$ are orthogonal matrices with respect to the newly defined scalar product (5.11);

$$\mathbf{U}_n^H\,\mathbf{G}\,\mathbf{U}_n = \mathbf{I} \tag{5.26}$$

$$\text{and} \qquad \mathbf{V}_n^H\,\mathbf{G}\,\mathbf{V}_n = \mathbf{I} \tag{5.27}$$

To conclude, in order to better satisfy the orthogonality of continuous function, a new scalar product between vectors of coefficients has been defined, making use of the Gram matrix. This supposes a new way to factorize the MoM impedance matrix, given by (5.21) where $\mathbf{A}$ defined by (5.7). Then, a simple expression for the currents is given by (5.20).

[1] We note that $\mathbf{U}_n^H\,\mathbf{G}\,\mathbf{U}_n = \mathbf{U}_D^H\,(\mathbf{A}^{-1})^H\,\mathbf{G}\,\mathbf{A}^{-1}\,\mathbf{U}_D$ then $\mathbf{U}_n^H\,\mathbf{G}\,\mathbf{U}_n = \mathbf{U}_D^H\,\mathbf{U}_D = \mathbf{I}$

Interpretations

In this section, we more explain the numerical method proposed above with the help of Professor Paul Van Dooren. Based on the initial problem

$$\mathbf{Z}_s \, I_s = E^e \tag{5.28}$$

and by correlating the excitation and current vectors with the matrix $\mathbf{A}$ we define a new excitation vector E_D^e as $\mathbf{A}\, E^e$ and a new vector $I_D = \mathbf{A}\, I_s$ containing unknown current coefficients on the scatterer. Consequently, an equivalent MoM system of equations is obtained

$$\mathbf{A}\, I_s = \mathbf{A}\, \mathbf{Z}_s^{-1}\, \mathbf{A}^{-1}\, \mathbf{A}\, E^e \tag{5.29}$$

where the matrix $\mathbf{A}$ is obtained from Cholesky factorization of the Gram matrix. Equation (5.29) can be re-written as

$$\mathbf{D}\, I_D = E_D^e \tag{5.30}$$

where $\mathbf{D}$ is a matrix defined as $\mathbf{A}\, \mathbf{Z}_s\, \mathbf{A}^{-1}$.

Using the SVD decomposition, we can diagonalize the matrix $\mathbf{D}$ and obtain the current distribution I_D. The matrix $\mathbf{D}$ is the same matrix defined by (5.22) since

$$\mathbf{D} = \mathbf{A}\, \mathbf{Z}_s\, \mathbf{A}^{-1} = \mathbf{A}\, \mathbf{S}_n\, \mathbf{A}^H \qquad \text{with} \qquad \mathbf{Z}_s = \mathbf{S}_n\, \mathbf{G} \tag{5.31}$$

From (5.30)and (5.31), we can note that the equivalent initial problem is

$$\mathbf{S}_n\, \mathbf{G}\, I_s = E^e \tag{5.32}$$

5.2.2 Influence of the scatterers' discretization

The impact of the structure's discretization on the simulation results using the implemented code has been analyzed. We made the simulation of the square scatterer presented in the Chapter 4 (see Fig. 5.1) and the scatterer based on the irregular jet-fluid geometry printed on a lossy dielectric

Number of Basis Functions	$\|\|I_1{}^H \times I_2\|\|$	$\|\|I_1{}^H \times \mathbf{G} \times I_2\|\|$
Square structure		
m1: 288	$5\ 10^{-3}$	$2.52\ 10^{-4}$
m2: 343	$6.5\ 10^{-3}$	$2.71\ 10^{-4}$
Relative Error (%)	30	7.6
Natural jet-fluid structure		
m1: 464	$3.16\ 10^{-4}$	$1.97\ 10^{-6}$
m2: 531	$3.45\ 10^{-4}$	$1.92\ 10^{-6}$
Relative Error (%)	9.18	2.54

Table 5.1: Relative Error (in %) of the orthogonality between two current densities, using different inner products ($\langle I_1, I_2\rangle$, and $\langle I_1, I_2\rangle_G$) versus the number of basis functions of the scatterer printed on a lossy dielectric substrate (square and natural jet-fluid geometries).

substrate FR4. The natural jet-fluid structure studied as an antenna in the Chapter 2 (see Fig. 5.9). The total current distribution I_i on the scatterer is compiled using (5.20). The orthogonality between two currents distribution will be calculated in two ways. First according to the approximated inner product $\langle I_i, I_j\rangle$ and then using the inner product based on the Gram matrix (5.11).

The relative error level is defined as $||P_{m1} - P_{m2}||/||P_{m1}||$ where P_{m1} and P_{m2} are the scalar product between two total surface currents in case of two different meshes $m1$ and $m2$ of the structures; the first is the square scatterer at frequency 2.41 GHz. The second is the jet-fluid scatterer (Fig. 5.9) at frequency 3.32 GHz. The relative error is given in percent.

The effect of the discretization of the scatterer was studied using a developed Matlab code (Gram-MoM code). We report the results for regular and irregular geometries. Table 5.1 shows that the results appear to be highly dependent on the discretization density when the Gram matrix is not used in the simulation. The relative error obtained after the use of the proposed product (5.6) is the smallest value in both scatterers. The dependence of results is compared to derive the Gram matrix effect. We show that the use of the defined scalar product based on the Gram matrix in the simulation leads to a weaker effect of the discretization density on the simulated results.

The SVD-eigenmodes approach proposed in the previous chapter is based on the diagonalization of the MoM impedance matrix using the SVD decomposition. In this section, a new method is presented to diagonalize of the MoM impedance matrix with an alternative to the SVD decomposition. This alternative decomposition leads to orthogonal eigenmodes and *associated eigen-vectors* with respect to the proposed scalar product based on the Gram matrix. The SVD-eigenmodes technique is reformulated by including the proposed methodology, as explained in Section 5.2.1, and the proposed eigenmodes method named in this chapter as a Gram-SVD-technique.

The next sections present numerical results simulated using the MoM code developed in the previous chapter for multiple antennas and including the G-methodology. The Gram-SVD-eigenmodes method has been first implemented for some structures with simple geometries. The technique then extends to complex structures based on fractal geometries and larger arrays used as transmitting and receiving antennas.

5.3 Numerical examples

In this section, numerical results are presented for the technique described in the previous section. The Gram-SVD-eigenmodes approach is applied to the printed system studied in the previous chapter for an array consisting of two printed dipole antennas. We extend the number of excitations/receivers to four printed dipole antennas and compile the frequency responses from a scatterer related to the first four selective eigenmodes. The validation of the technique is presented here using a scatterer based on simple structures, as those proposed in the previous chapter (square and rectangular tag) and triangular shapes. We revealed that the modified SVD-eigenmodes can be applied to complex structures: a complex natural oval leaf and an irregular fractal jet-fluid geometries (see Chapter 2). The advantages of the reformulated modal analysis and the possibility to employ more than two modes to exploit the signature of a scatterer will be presented through a demonstration of our efforts based on a numerical analysis of different examples.

5.3.1 Scatterers with Simple Geometries

In the previous section, we presented a new methodology to diagonalize the MoM Impedance matrix based on a special scalar product to obtain orthogonal matrix and a good projection of the *associated eigen-vectors* on the excitation. Here, a numerical validation of the Gram-SVD-technique is described, considering a simple scatterer and the printed system with two antennas acting as transmitter and receiver, as also considered in the Chapter 4.

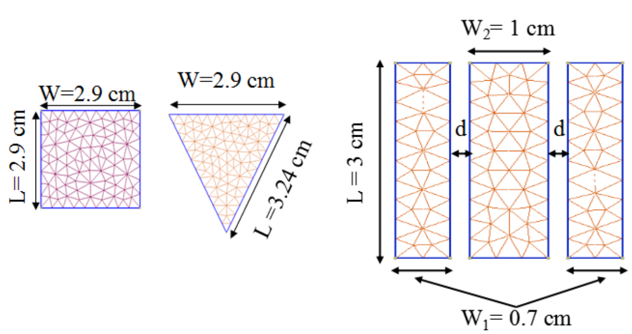

Figure 5.1: Scatterers based on different planar simple geometries; square, triangular, and multi-scatterer structures.

Let us demonstrate the technique on three examples of different simple structures. First is a 2.9×2.9 cm square discretized with 343 triangular RWG elements. Second is a multi-resonator scatterer based on separate parallel conductive strips discretized with 233 RWG basis functions. The horizontal distance between rectangular conductive strips is equal to

$d = 0.25\ cm$. The last scatterer with simple geometry is a triangle, its dimensions are shown in Fig. 5.1 and it discretized with 349 triangle RWG basis functions.

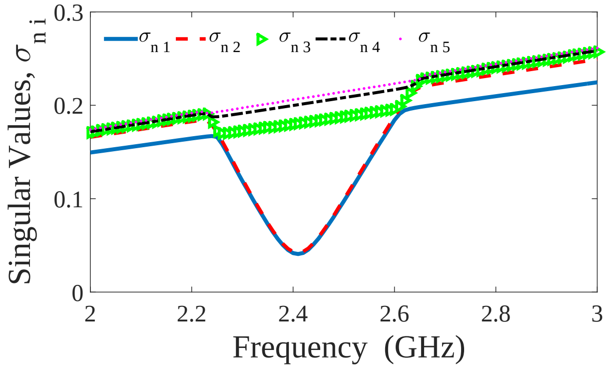

Figure 5.2: The singular values ($\sigma_{n\,i}$) of the square scatterer versus frequency.

In general, the easiest way to consider that a mode on the scatterer is resonant, it consists of selecting the frequency at which one finds the smallest singular values. Fig. 5.2 presents the variation of singular values σ_{ni} versus the frequency for the first five eigenmodes of the printed square scatterer. Using the methodology presented above, we observed that the first two eigenmodes are at resonance ($\sigma_{n\,i}$ very small and close to zero) similar to those obtained using the traditional SVD-eigenmodes technique, with singular values at resonance are more near to zero. The dominant eigenmodes are associated to the smallest singular values, which correspond to high induced currents. From Fig. 5.2, it can be noted that eigenmodes $V_{n\,1}$ and $V_{n\,2}$ resonate at 2.41 GHz, and the eigenmode $V_{n\,3}$ resonate near the frequency 2.26 GHz.

The extracted responses versus frequency related to the first two dominant eigenmodes of the square scatterer are calculated for the frequency band 2-3 GHz with 10 MHz steps based on the Gram-modified methodology. A comparison between the responses r^e obtained from the devel-

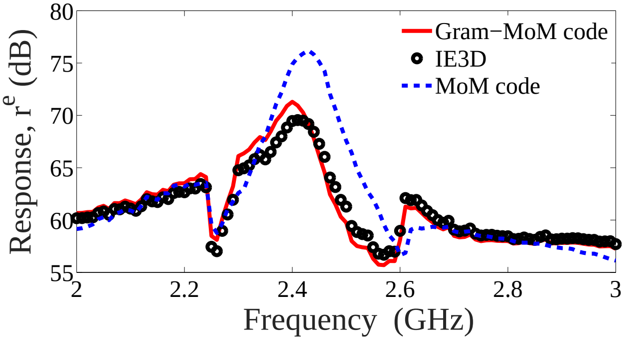

(a)

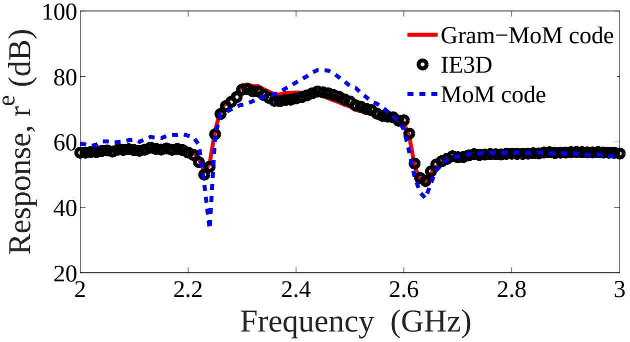

(b)

Figure 5.3: Comparison of the responses r^e from a square scatterer using the Gram-MoM code and the IE3D software related to the dominant modes; (a) first eigenmode and (b) second eigenmode.

oped MoM code including the methodology proposed in second section (Gram-MoM code) and the IE3D software are presented. Fig. 5.3 shows the responses when the first mode is selected while the second eigenmode is suppressed (Fig. 5.3.a). Similarly, Fig. 5.3.b shows the response related to the second mode. The responses resulting from the Gram-MoM code and IE3D compare well over the frequency band. The responses related to the first two dominant modes are clearly distinct, when the first or the second wanted eigenmodes are excited. Using the Gram-SVD-eigenmodes technique, we can observe that the frequency responses of the tag are smoother and the dominant eigenmodes are more stable versus frequency, compared to those presented in the previous chapter.

5.3.1.1 Multi-scatterer chipless tag

The response from a scatterer comprising three separate parallel conductive strips (see Fig. 5.1) is presented for the selective eigenmodes in this section. The system consists of the printed array of two antennas acting as a reader in the near-filed. The multi-scatterer tag is used to validate the proposed eigenmodes method and to study the skin effect on the simulated results and the frequency responses of the tag.

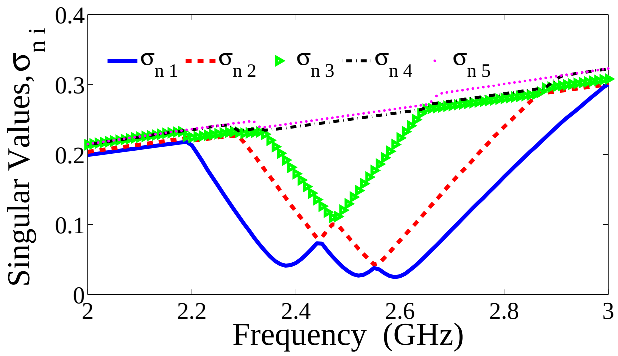

Figure 5.4: The singular values ($\sigma_{n\,i}$) of the multi-resonator tag versus frequency.

Fig. 5.4 allows one to determine the resonance of the eigenmodes of the scatterer through the variation of the associated singular values to the eigenmodes with respect to frequency. From Fig. 5.4, it can be observed that the first eigenmode $V_{n\,1}$ of the multi-scatterer tag is the dominant eigenmode over the whole frequency band [2-3] GHz. The first eigenmode resonates at three different frequencies, 2.38, 2.52, and 2.59 GHz where the associated singular value is close to zero. Also, the second eigenmode $V_{n\,2}$ resonates at the frequencies of 2.44 GHz and 2.56 GHz. The third eigenmode resonates at a frequency of 2.47 GHz.

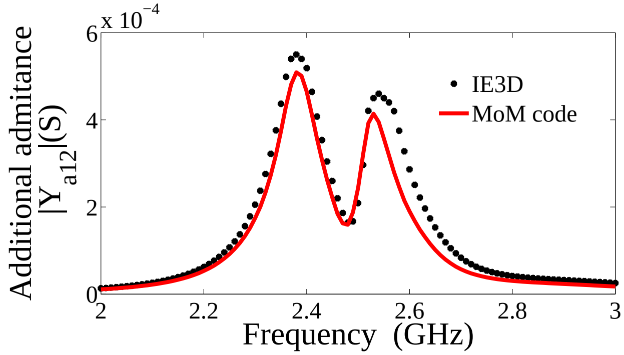

Figure 5.5: Comparison of the difference between mutual admittance (System with or without multi-resonator scatterer) using Gram-MoM code and IE3D.

The influence of the scatterer inside the system is distinct through the calculation of the "additional" mutual admittance ($Y_{a\,12}$). As defined in the previous chapter, the matrix $\mathbf{Y}_a$ is the difference between the mutual differential admittance matrix , in the presence of the scatterer, and in its absence. The comparison of $Y_{a\,12}$ carried out with simulation using the implemented Gram-MoM code and the IE3D software is presented in Fig. 5.5. The results compare well with slight discrepancies, which can be attributed to numerical errors and to the discretization of the structure. From Fig. 5.5, we can conclude that the multi-scatterer tag has a consistent signature.

The frequency responses from the multi-scatterer structure associated to the first two eigenmodes are extracted using the code based on the reformulated eigenmodes technique presented in the Section 5.2. Fig. 5.6 presents the frequency responses when the first or the second eigenmode is selected and the other is suppressed. We see that the responses are very distinct from each other and we can distinguish them from the responses from the square tag (Fig. 5.3).

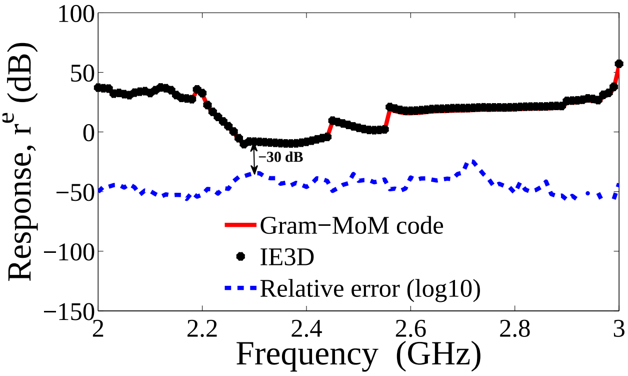

(a)

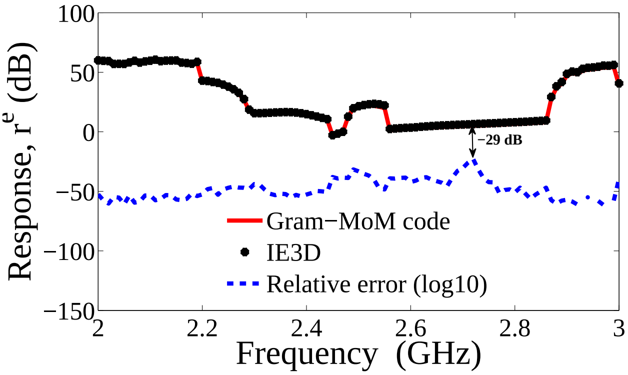

(b)

Figure 5.6: Comparison of the responses r^e from a multi-resonator scatterer using the Gram-MoM code and the IE3D software related to the selected modes; (a) first eigenmode and (b) second eigenmode. (- -) Relative error (dB) using the IE3D software with respect to the response related to the selected mode with thickness of conducting tag equal to $h_{c1} \cong 17\ \mu m$.

5.3.1.2 Effects of metallization thickness on the response from chipless tags

As shown above the frequency responses rely on the scatterer's shape and the selective dominant mode. Also, as explained in previous chapter, the alignment of the tag has an effect on the frequency responses of the tag with respect to the voltage sources position. Besides, the thickness of the conductor has not a marked effect on the responses from the tag. To quantify this, a simulation using the IE3D software has been carried out in [2-3] GHZ frequency band. To study the influence of the thickness of the conducting structure on the responses from the scatterer, the "additional" admittance matrix is calculated using the IE3D software for two different thicknesses of the scattarer.

In this thesis, we considered copper (the electric parameters of the copper: $\sigma = 5.8\ 10^6\ S/m$ and $\mu = \mu_0$) metal for the printed chipless RFID tag and the printed array. The frequency responses $r^e_{h_{c1}}$ from the multi--scatterer is simulated of referent thickness $h_{c1} \cong 11.5\ \delta_{dt} = 17\ \mu m$ where δ_{dt} is the skin depth thickness of conducting structures [213]. The skin depth is equal to $\sqrt{2/(\omega\ \mu\ \sigma)} = 1.47 \mu m$ at 2 GHZ where ω is the radian frequency , μ the permeability of the metal, and σ is the conductivity. The system is simulated for two other thicknesses: $h_{c2} = 2\ \mu m$ and $h_{c3} = 0.5\ h_{c1} \cong 0.7\ \mu m$. The responses from the multi-scatterer tag associated to the selective eigenmodes are obtained based on the admittance matrix simulated using the IE3D software for different thicknesses of the metal.

The relative error levels are shown in plots Figs. 5.6 and 5.7 is calculated as $10\ log_{10}\ (||r^e_{h_{c1}} - r^e_{h_{ci}}||/|r^e_{h_{c1}}||)$ where $r^e_{h_{c1}}$ is the frequency responses from the tag of the referent thickness h_{c1} and $r^e_{h_{ci}}$ is the responses of the metallization thickness h_{c2} or h_{c3} for the scatterer and for the printed array. The relative error is given in dB. Fig. 5.6 present the relative error levels when the responses from the tag simulated for thicknesses h_{c1} and h_{c2}. As can been seen from Figs. 5.6. (a) and (b), the error level in the computation results is below -30 dB for the frequency response associated to the first selected eigenmode and the second eigenmode is suppressed. The error level is below -29 dB for the response related to the second eigenmode. It should be noted that error levels are good given the magnitude of reference signature. From Figs. 5.6. (a) and (b), we can note that the accuracy in the computation of the results (for the metallization thickness h_{c1} and thin thickness h_{c3}) is still relatively good with error levels below -14 dB. From those plots, we can validate that the skin depth thickness of the conducting structures does not have a significant influence on the responses from the tag.

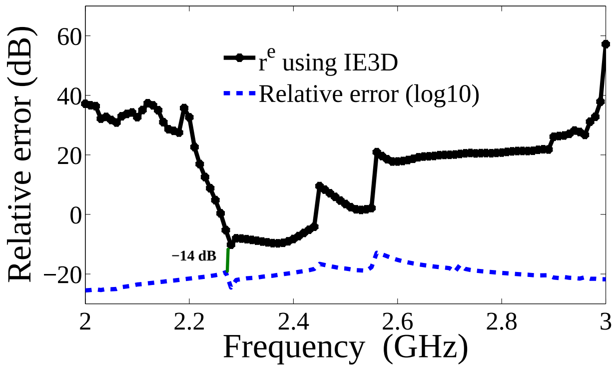

(a)

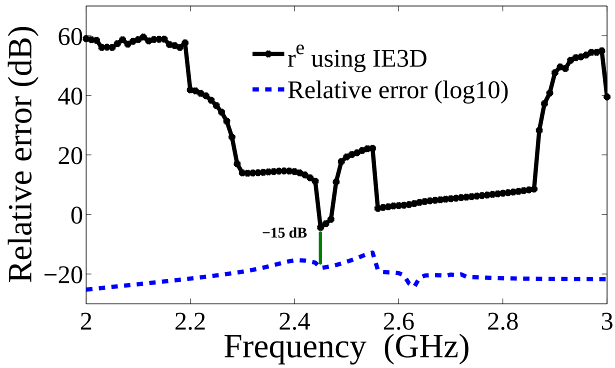

(b)

Figure 5.7: response related to the selected mode $r^e_{h_{c1}}$ using the IE3D software. Relative error (dB) with respect to the response $r^e_{h_{c3}}$ from the tag with $h_{c3} = 0.5\,\delta_{dt}$.

In next sections, the eigenmodes method based on the alternative decomposition to SVD decomposition is used to extract the frequency signature of a scatterer with a natural fractal geometries using a larger array acting as a reader.

5.3.2 Scatterers based on Irregular Natural Shapes

The SVD-eigenmodes method is extended by using a new process for matrix diagonalization based on a special inner product. Here, we show that the Gram-SVD-eigenmodes approach can be implemented considering any shape of printed scatterer on a lossy dielectric substrate (FR4). The response from a scatterer with complex irregular shapes is presented for the selective eigenmodes, the printed system consisting of two antennas is used as before.

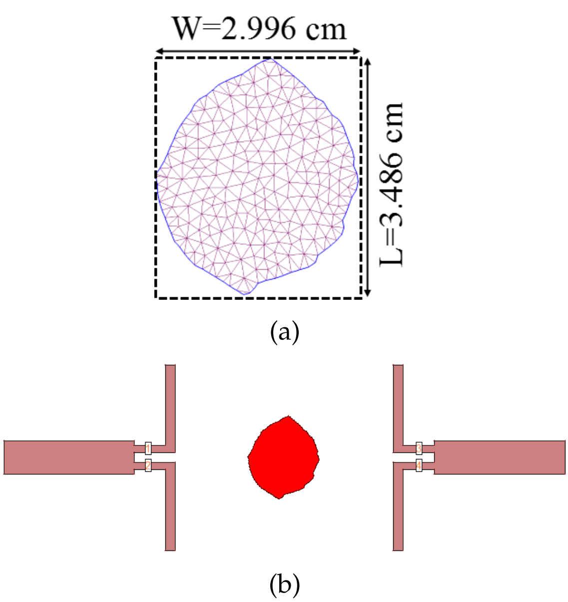

Figure 5.8: Top view of the System printed on a multilayered lossy dielectric (FR4) substrate with a scatterer based on a natural oval leaf shape.

The Gram-SVD-eigenmodes technique has been validated through two examples for scatterers formed by irregular natural geometries; the first one is an oval leaf geometry which is obtained from a young quaking aspen leaf. The second scatterer is based on a more complex structure, which is the irregular natural jet-fluid presented in the Chapter 2. This shape is

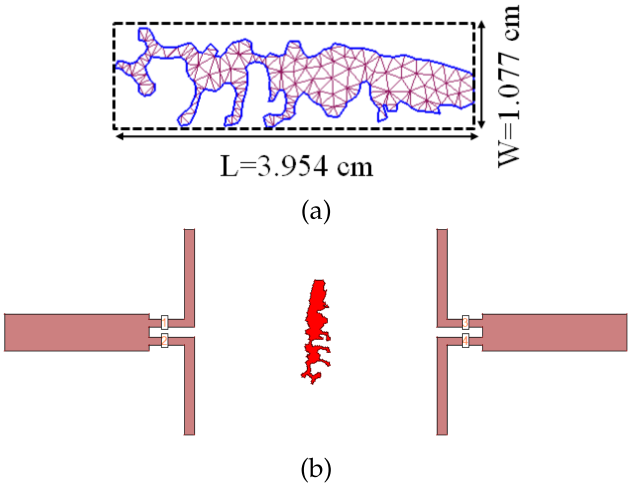

Figure 5.9: Top view of the System printed on a multilayered lossy dielectric (FR4) substrate with the complex jet-fluid structure.

obtained from a liquid jet issuing from an injector. The length and width of the radiating patch are defined as the dimensions of the smallest rectangle containing the complex irregular image. The oval leaf of dimension equal to 2.996×3.486 cm was printed on an infinite lossy dielectric substrate FR4 with relative permittivity $\epsilon_r = 4.3$, loss tangent $\delta = 0.02$ and thickness equal to 0.16 cm and backed by an infinite ground plane (see Fig. 5.8). Later, the oval leaf structure was replaced by the jet-fluid scatterer of dimension 3.954×1.077 cm (see Fig. 5.9); both scatterers are located at a distance around $d = \lambda/2$ from the antennas. The oval leaf structure has been discretized with the help of 530 RWG basis functions and the jet-fluid has been meshed with 464 RWG basis functions, the associated singular values are calculated over the frequency band 2-4 GHz for the oval leaf scatterer and 3-5 GHz for the jet-fluid patch.

To determine the resonance of the first five eigenmodes of the printed oval leaf and jet-fluid scatterer, their associated singular values are checked to be close to zero. Figs. 5.10 and 5.11 present the variation of the singular values corresponding to the first five eigenmodes with respect to frequency. From Fig. 5.10, it can be observed that the eigenmode V_{n1} of

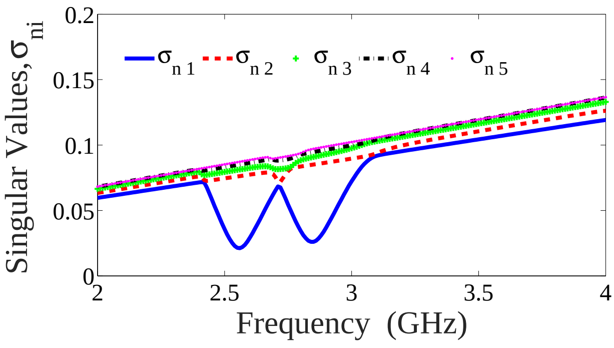

Figure 5.10: The singular value (σ) of the oval leaf scatterer versus frequency.

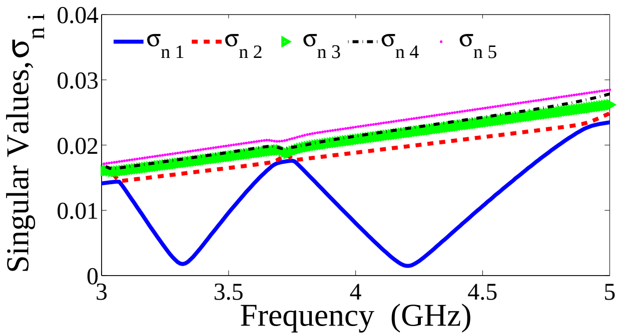

Figure 5.11: Singular values (σ_n) of the jet-fluid structure versus frequency.

the oval leaf scatterer is the dominant eigenmodes over the whole frequency band. The eigenmodes $V_{n\,1}$, resonates at two different frequencies (2.56 GHz and 2.85 GHz). We can note also that eigenmodes $V_{n\,2}$ and $V_{n\,3}$ resonate at 2.72 GHz. The singular values associated to the first five eigenmodes of the jet-fluid patch are plotted as a function of frequency in Fig. 5.11. From this plot, the multi-resonant behavior of certain modes, such as the first eigenmode of the scatterer, is evident. The eigenmode $V_{n\,1}$ is the dominant mode over the frequency band 3-5 GHz, $V_{n\,1}$ resonate at 3.32 GHz and 4.21 GHZ. The multi-resonant behavior is the characteristic of the natural jet-fluid structure as discussed in the Chapter 2.

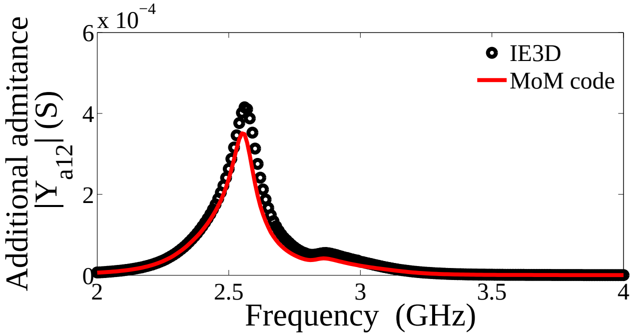

(a)

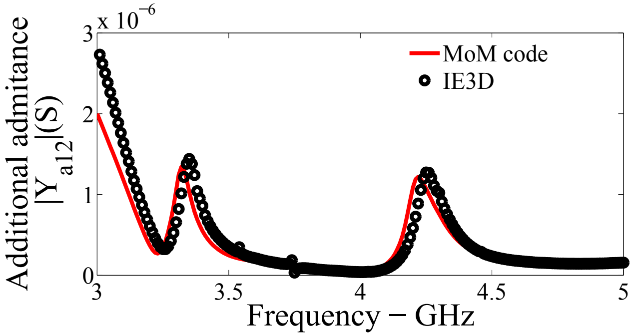

(b)

Figure 5.12: Comparison of the difference between mutual admittance (System with or without (a) oval leaf scatterer or (b) jet-fluid scatterer) using Gram-MoM code and IE3D.

In order to distinguish the effect of the complex scatterer inside the chipless passive system, the "additional" mutual admittance ($Y_{a\,12}$) is calculated. The matrix $\mathbf{Y}_a$ is defined in previous section, it is the difference between the mutual differential admittance matrix , in the presence of the scatterer, and in its absence. The comparison of $Y_{a\,12}$ carried out with simulation using the Gram-MoM code and the IE3D software is presented in Fig. 5.12. Those results compare well with minor discrepancies, which can be attributed to numerical errors and the discretization of the structures carried out differently in our code and with the IE3D software. Fig. 5.12 demonstrate that the scatterer′s discretization density has not a high influence on the simulated results even for complex structures.

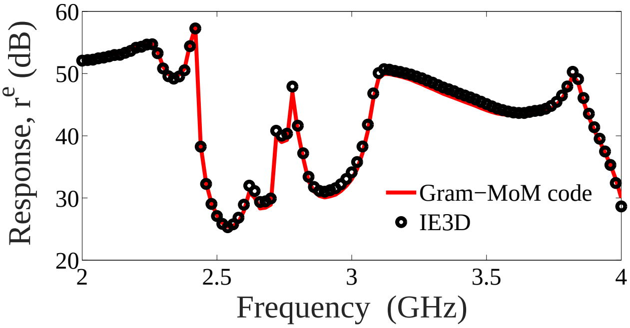

(a)

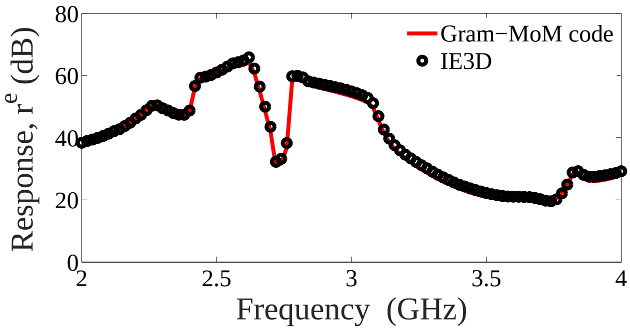

(b)

Figure 5.13: Comparison of the responses r^e from an oval leaf scatterer using the Gram-MoM code and the IE3D software related to the selected modes; (a) first eigenmode and (b) second eigenmode.

The code based on the Gram-SVD-eigenmodes technique is used to extract the frequency responses associated to the first two eigenmodes of the complex natural structures. Figs. 5.13 and 5.14 present the frequency responses when the first or the second eigenmode is selected and the other is suppressed. The responses from the oval leaf scatterer are very distinct from each other (Fig. 5.13. a and b). Similarly to the frequency responses

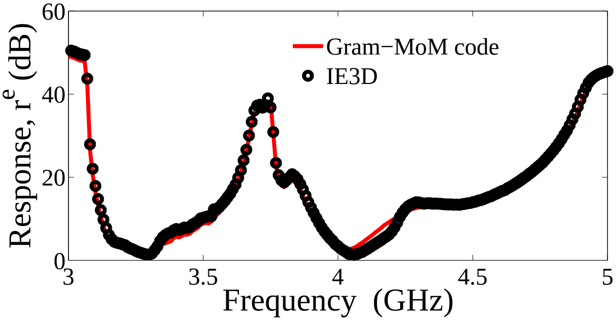

(a)

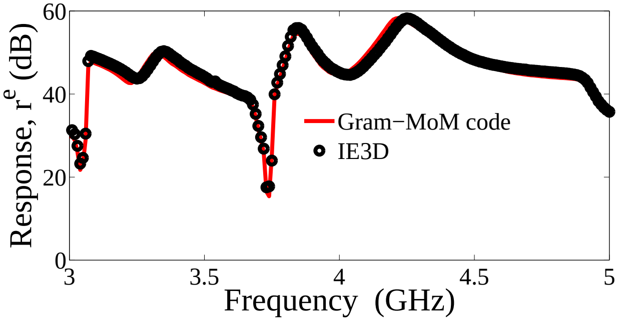

(b)

Figure 5.14: Comparison of the responses r^e from the jet-fluid scatterer using the Gram-MoM code and the IE3D software related to the selected modes; (a) first and (b) second eigenmodes.

from the jet-fluid scatterer (Fig. 5.14. a and b). We can clearly distinguish the jet-fluid's response from the oval leaf's responses or the responses from any other structure.

The simulated results presented in this section demonstrate that the complex fractal structures can contain richer information than for the structures based on simple shape. The frequency responses from scatterers with different shapes are discontinuous versus the frequency, resulting from the switching between the dominant eigenmodes (see Chapter 4, Section 4.3.3).

5.3.3 Selective excitation of eigenmodes using a larger array

The eigenmodes technique based on the Gram matrix is extended in this section through the use of an array consisting of transmitters and receivers with more antennas.

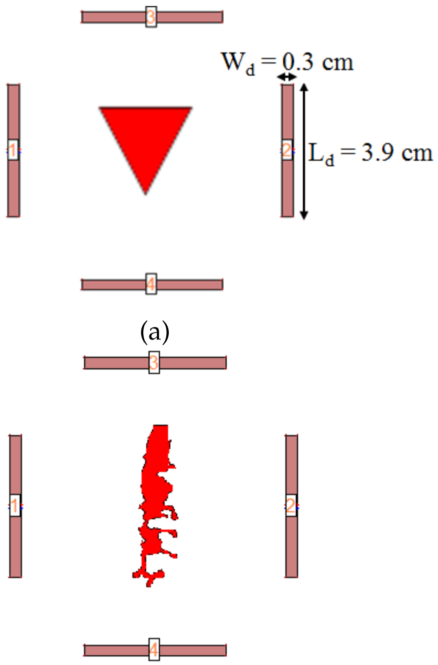

(b)

Figure 5.15: System based on four antennas with (a) triangular scatterer and (b) natural jet-fluid patch.

The analyzed array consists of 4 dipole antennas distributed on a square surface, as shown in Fig. 5.15. Each antenna of width W_d = 0.3 cm and length L_d = 3.9 cm has been discretized with the help of 90 RWG and one RWG-rectangular hybrid elementary basis functions. A delta-gap generator is placed in the middle of the antenna and the dipole used to excite the structure. The array is printed on the first layer with a lossy dielectric substrate (FR4) of thickness equal to 0.32 cm. We note that each dipole is resonant at a frequency of 2.43 GHz. The radiating elements chosen for this system correspond to the scatterers presented in the previous section with simple geometry and complex natural shape. The scatterers studied here are the triangular and jet-fluid structures shown in Fig. 5.15; the distance between the scatterer and the dipole antenna is close to $\lambda/2$.

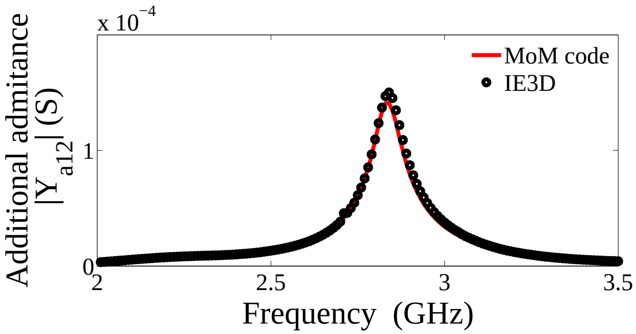

(a)

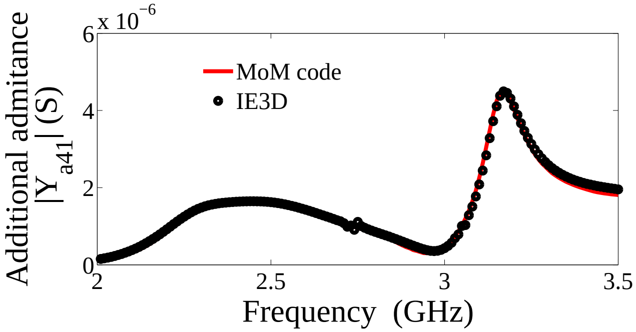

(b)

Figure 5.16: Comparison of the difference between mutual admittance when the array consists of 4 antennas using MoM code and IE3D.

A consistent signature of the scatterer appears for the "additional" admittance parameters, which are calculated here from the difference between the admittance parameters in the presence and absence of the scatterer (see Chapter 4, Section 4.3.3). Fig. 5.16 presents the "additional" admittance parameters Y_{a12} and Y_{a41}, where the simulated results, obtained with our implementation and with the commercial software, compare very well. Those results confirm the effect of the triangular scatterer inside the system comprising a large array. The larger number of excitations and receivers allows the selection of other specific (dominant) eigenmodes. In this case, the frequency responses r^e from the triangular and jet-fluid scatterers are extracted using the metrics proposed in the Chapter 4/ Section 4.3.3.

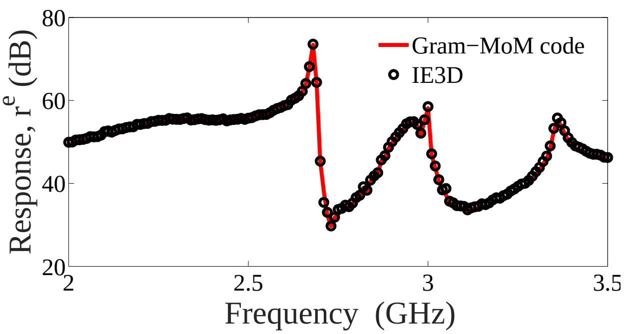

(a)

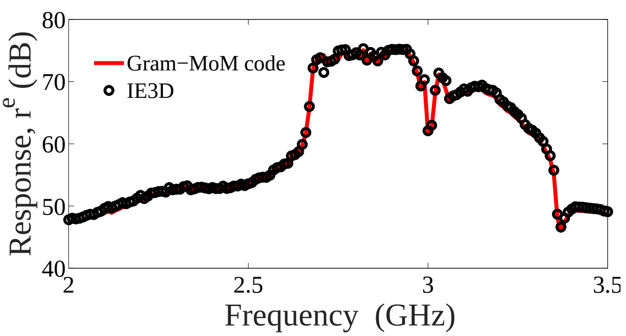

(b)

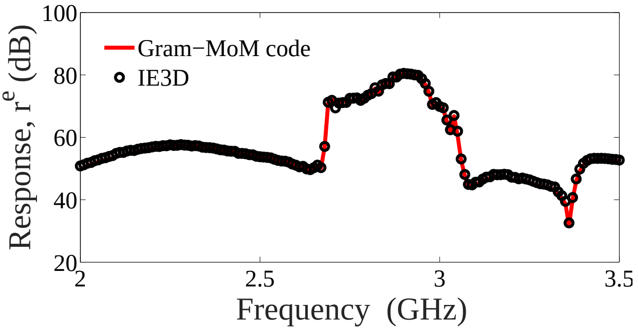

(c)

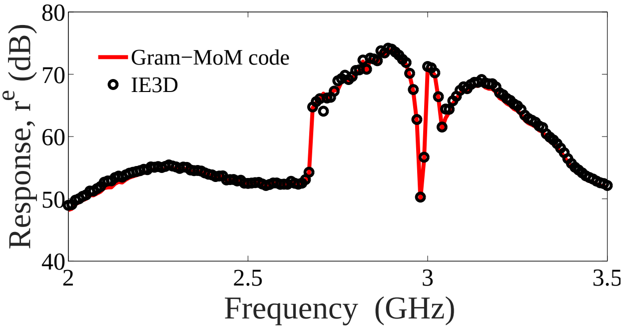

(d)

Figure 5.17: Comparison of the responses r^e of the triangle structure using the Gram-MoM code and the IE3D software related to the selected modes; (a) dominant eigenmode and (b, c, and d) second, 3rd and 4th eigenmodes.

Figs. 5.17 and 5.18 present the responses related to the first four eigenmodes, when one dominant eigenmode is excited and the three other eigenmodes are suppressed. For each structure, the responses are very distinct and they depend on to the wanted eigenmodes. The results presented in this chapter allow us to improve the independence of any scatterer's signature from the environment. Also, we can note that each scatterer presents a unique frequency response related to an eigenmode. The eigenmodes approach proposed in this thesis is finally verified on selected antennas candidate with different shape of the scatterer, which are simulated both with an in-house tool and using commercial software.

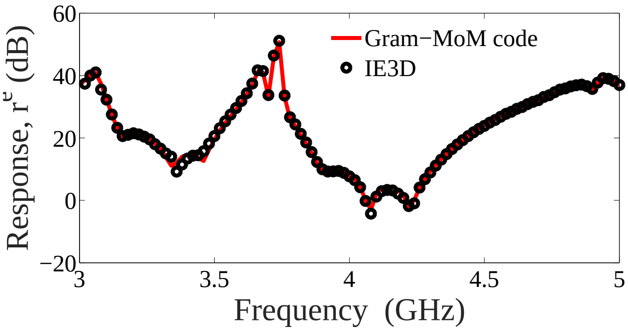
Gram−MoM code
IE3D
Response, r^e (dB)
Frequency (GHz)
60
40
20
0
−20
3
3.5
4
4.5
5

(a)

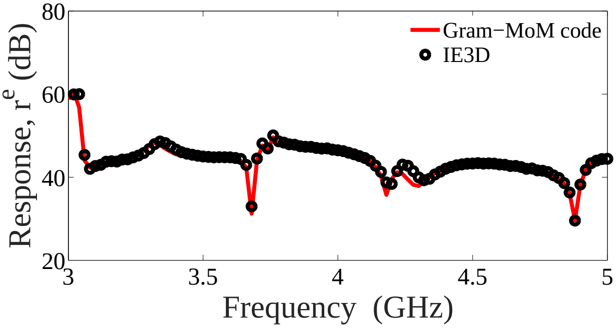
Gram−MoM code
IE3D
Response, r^e (dB)
Frequency (GHz)
80
60
40
20
3
3.5
4
4.5
5

(b)

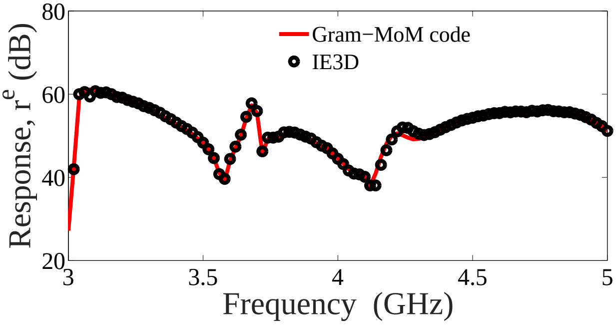
Gram−MoM code
IE3D
Response, r^e (dB)
Frequency (GHz)
80
60
40
20
3
3.5
4
4.5
5

(c)

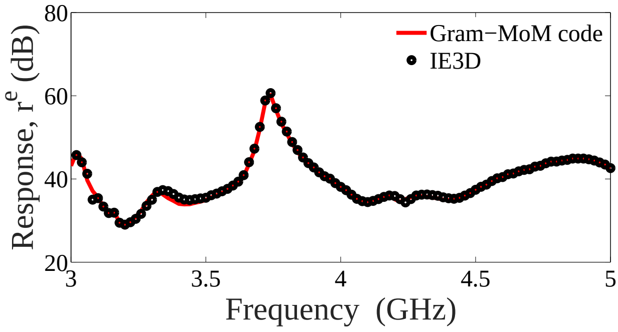

(d)

Figure 5.18: Comparison of the responses r^e of the jet-fluid structure using the Gram-MoM code and the IE3D software related to the selected modes; (a) dominant eigenmode and (b, c, and d) second, 3rd and 4th eigenmodes.

The results as the singular values, "additional" admittance, and the frequency responses of the square, the rectangular, the triangle, and the oval leaf scatterers using the reader consist of an array of two or four dipoles are also simulated using the implemented Gram-MoM code and the IE3D software.

5.4 Conclusion

The eigenmodes approach has been proposed in a previous chapter to analyze a radiating structure printed on a thin lossy dielectric layer. The proposed technique allows the selection of particular eigenmodes of the scatterer using multiple transmit and receive antennas, which in turn enables the extraction of the unique signature associated with the wanted dominant eigenmode. In the previous chapter, the frequency responses of a tag provide independent signatures for the same scatterer, and the easiest way to distinguish it from other scatterers.

Using the eigenmodes technique proposed in this chapter, the eigenmodes of the tag have been generated through the alternative to SVD decomposition of the MoM impedance matrix of the scatterer based on a specific inner product that uses the Gram matrix between basis functions. The inclusion of this matrix allows the minimization of the influence of the scatterer's discretization density on the obtained surface currents orthogonality, and a little more on the stability of the dominant eigenmodes of the scatterers versus frequency. Then, the newly defined eigenmodes are used with the SVD-eigenmodes technique for multiple excitations to extract the responses from the scatterer.

This methodology has been validated through the study of scatterers with different shapes, simple and complex natural geometries, using the implemented Gram-MoM code and the IE3D software. The proposed technique is extended to a larger number of transmitting and receiving antennas to be able to select other dominant eigenmodes which may contain/ reveal more information. In all cases, the effect of the scatterer has been studied from the "additional" mutual impedance matrix, obtained after background extraction. The proposed eigenmode approach allows the production of responses associated with each eigenmode separately. The responses of the tag have been studied using the developed Gram-MoM code and the IE3D software. The frequency responses are related to the dominant eigenmodes of the tag and those responses are very different. Responses from tags with a wide variety of shapes are also clearly distinct. The responses of tags obtained using the Gram-SVD-eigenmodes approach are almost similar to those obtained using the SVD-eigenmodes technique proposed in the Chapter 4.

The problem of the instability of the modes versus frequency has still been observed when using the modified eigenmodes technique. Tracking algorithms [214,215] to improve the stability of eigenmodes versus frequency should be further investigated.

Conclusion and Future Scope

6

6.1 Conclusion

Radio-Frequency Identifications (RFID) technology is the current trend. It is receiving an important attention in various sectors, related to the identification and/or authentication of objects or persons without physical contact. The passive RFID technology is based on the variation of the tag's response. The tag (or scatterers) comprises an antenna terminated by a chip which can be switched between two terminations (short circuit and open circuit). The reader powers the chip, in which case the chip should not have a battery. However, those chips remain relatively expensive and the range over which the circuit of tag can be powered is limited. Nowadays, the use of the passive chipless RFID systems is growing. Although different chipless RFID tags are implemented in many engineering applications due to their relatively low fabrication cost and small size, while good performance is maintained. In this perspective, the chipless RFID tags design comes with important challenges: the extraction of sufficiently rich information resulting from the shape of the tag and the avoidance of strong interference from the environment of the tag.

The passive chipless RFID system studied in this thesis is comprised of a chipless RFID tag and multiple associated readers. Tags with read-write capability can be the target of falsification of tag content (such as the availability, the identity or the information details of goods or people), or of unauthorized modification of the tag data. This doctoral research has therefore mainly been focused on the synthesis of the electromagnetic signature of chipless RFID tags. The main goal of this thesis consists of ensuring that as much information as possible is encoded in the shape of the tag. A specialized hardware (transmitting and receiving array acting as a reader) provides full access to the information, while specific efforts are made to discriminate the response of the scatterer from that of the environment.

In this thesis, a design of a chipless RFID tag antenna with irregular fractal shape is proposed to minimize the falsification or the counterfeiting of chipless RFID tags. In Chapter 2, we have studied the electromagnetic behavior of an antenna printed on a lossy dielectric substrate (Duroïd) backed by a ground plane. The structure is based on a complex natural geometry obtained from a liquid jet-fluid. First, we have designed and simulated the antenna using the commercial Ansoft-HFSS software. The numerical analysis of the antenna has mainly revealed the multiple resonances of the structure. Second, this multiband behavior has been investigated in order to design a chipless RFID tag with a unique electromagnetic signature. It is possible to use the printed tag for security of the chipless RFID system or for access control because it is not easy to emulate or produce a new tag as a duplicate of the original one (cloning) with the complex fractal shape. The main contribution of this thesis is the analysis of the response of chipless passive RFID tags, for the super-high-frequency (SHF) band, near 2.4GHz, using a proposed eigenmodes technique for near-field operation, based on the singular values decomposition (SVD). The method relies on the method of moments, which is often used to obtain the currents induced on printed structures. Those currents are decomposed into basis functions and the associated coefficients result from the solution of a linear system of equations, characterized by a matrix named the "impedance matrix". Then, the SVD decomposition is used to obtain a diagonalization of the MoM impedance matrix and to extract the eigenmodes on the scatterer. To check the accuracy of our proposed eigenmodes approach, we compared our results with those obtained with other methods, such as the theory of characteristic modes and a proposed eigenmodes technique based on the combination of the eigenvalue decomposition (EVD) and the QR algorithm. The eigenmodes technique presented in Chapter 4 is used to control the current distribution on a printed scatterer, such as a chipless RFID tag.

The eigenmodes approach based on the SVD decomposition is proposed to enrich the information that can be extracted from the tag. The method consists of exciting or revealing specific current distributions (or "eigenmodes") on the scatterer printed on a thin lossy dielectric substrate (FR4) backed by a ground plane, and exploiting specific frequency responses of a tag considering an antenna array acting as a set of near-field sources. The array has several transmitters to excite the scatterer and to induce the currents on the metallic tag and also several receivers to analyze the scattered fields. A beamforming process is also used on receive to realize a selective sensitivity to the selected eigenmodes. The beamforming weights used on transmit and receive hence allow the production of a signature associated to each dominant eigenmode. In Chapter 4, the eigenmodes method is implemented for two scatterers with different shapes using a reader comprising an array of two printed antennas on a multiple lossy dielectric substrate. The presented experimental results highlight the multiplicity of responses that can be generated with a given tag. This multiplicity provides independent signatures for the same tag, allowing the user to better distinguish the tag from others, and to improve its independence from scattering by the environment. It is possible to apply this Gram-SVD-eigenmodes technique for secure banknote applications.

An extension of the proposed eigenmodes analysis method is presented to obtain a unique signature for the scatterer with a variety of shapes, as well as considering a larger number of transmitting and receiving antennas. In Chapter 5, the eigenmodes method is modified based on another diagonalization of the MoM impedance matrix with respect to a special inner product. The inner product involves the Gram matrix between the basis functions defined on the tag. This product allows more accurate estimation of the scalar product between two physical current descriptions on the tag. In turn, the use of the Gram matrix allows one to minimize the effect of the variation of the structures' discretization. To a large extent, this solves the problem of practically all modal analysis methods that rely on a specific meshing of the structure and hence are not stable versus frequency. This work has been extended through the use of a larger number of excitations and receivers to control a plurality of wanted eigenmodes of the scatterer, which more fully exploits the natural response of the scatterer's shape.

6.2 Future Scope

We first suggest possible improvements to each contribution of the thesis and we propose some interesting paths for further research. A chipless RFID tag design is proposed based on the complex fractal geometry, then the reproduction of this tag is difficult. Such a tag can be used in security applications when it is embedded into an opaque medium.

An electromagnetic analysis of chipless RFID tags related to eigenmodes has been presented in this thesis. An eigenmodes technique is proposed to exploit multiple responses from the tag. The resulting frequency responses provide independent signatures for the same tag, allowing the user to better distinguish the tag from others, and to improve its independence from scattering by the environment. In this case, it is necessary to define a method to exploit the enriched information from the scatterer in presence of the environment's noise and to determine the effect's level of this noise on the frequency responses from the tag. Also, the discrimination of a tag from other with almost the same shape needs to be defined with respect to a difference threshold.

The proposed eigenmodes method based on SVD decomposition can be extended by proposed tracking algorithms to stabilize the eigenmodes of a structure versus the frequency based on the projection of the "associated" eigenmodes on the excitations.

The eigenmodes methods proposed in this thesis, can be used to numerically analyze radiating structures containing intrinsically rich geometrical information, such as the young quaking aspen leaf shapes or the jet-fluid geometries, as shown in Fig. 6.1. Those structures will be analyzed using the code developed in this thesis, as well as commercial software, for identifications applications. The simulated results can be validated through a comparison with results obtained from the measurement of a printed system consisting of printed scatterer with unique shapes and larger arrays.

The proposed eigenmode methods based on an alternative to the SVD decomposition could also be exploited in the field of MIMO (Multiple Input Multiple Output) communications in both near and far fields. Finally, in order to make the tag more flexible, we think about using an invisible tag keeping a specific response of the tag, especially by combining the complex shape of the tag and the developed eigenmodes approach. The invisible chipless RFID tag can be produced by embedding the scatterer into an opaque substrate or packaging such as paper or film in order to secure the passive chipless RFID system.

(a)

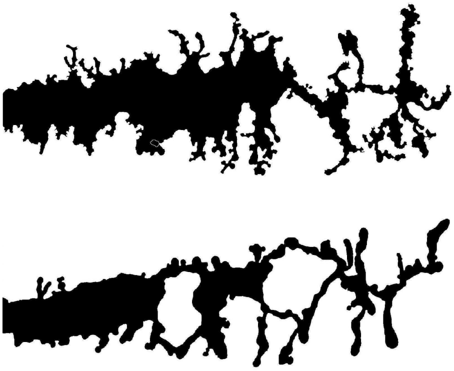

(b)

Figure 6.1: (a) Prototypes of the studied antennas printed on a lossy dielectric substrate (Duroïd) backed by a ground plane based on natural fractal image (young quaking aspen leaf [8]), and (b) others jet-fluid geometries.

Background Fractal concept

A

In this appendix, the goal is to give a brief overview on the fractal geometries and to explain the image processing used to obtain the natural fractal image used in Chapter 2 from a liquid jet-fluid injector.

A.1 Fractal Geometries

A fractal is a rough or fragmented shape that can be subdivided in multiple portions, each of which has the same geometry as the shape with a reduced-size. Fractal geometries are generally self-similar and independent of scale. They describe many real-world objects, such as clouds, mountains, turbulence, and coastlines. Those shapes correspond to complex geometry. The term fractal was invented by the French mathematician B.B. Mandelbrot [120] during 1970's after his revolutionary research on several naturally occurring irregular and fragmented geometries not contained within the area of conventional Euclidian geometry [120]. Mandelbrot included a definition of fractal dimension (of a geometric object) when he first talked about the concept of fractal in 1977. Fractal concept has found applications in geography, biology, and engineering [216,217]. Fractal concept in engineering has been used in the design of antennas, frequency selective surfaces, and the image processing [217]. Some examples of fractal geometry are given in Fig. A.1.

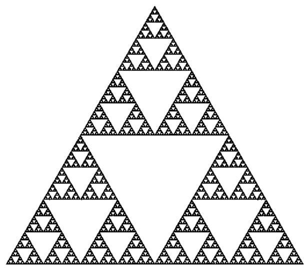

Sierpinski gasket

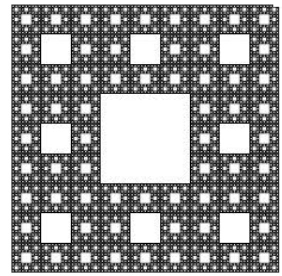

Sierpinski carpet

Branched tree [218]

Figure A.1: Examples of fractal geometries.

Regarding antennas, several fractal antennas geometries have been introduced and analyzed. Fractal antennas can be classified into two groups: deterministic and random structures. Deterministic structures [121–124, 219, 220], for which the self-similarity property can be described easily by a scaling power law, were widely studied in the last decades, and much deterministic geometry have proved to enhance the antenna performances [221]: Sierpinski monopole for multi-frequency operation [123], Koch monopole for miniaturization, Koch island patch for high directivity [220], and so forth. Besides, other fractal antennas groups are random/irregular fractal antennas, which require more complex mathematical laws to be represented and characterized by natural complex geometries. The complex fractal antennas are still largely unknown and their applications are few

[126, 128–133].

A.2 Obtaining The Natural Irregular Fractal Image

The image used in Chapter 2 is one of a liquid jet issuing from an injector. Being free of any parietal constraint, liquid jets injected in a gaseous atmosphere experience an atomization process. Perturbations appear and grow on the liquid gas interface until disintegration into individual liquid fragments occurs. When the perturbations are initiated by the liquid jet turbulence, the shape of the liquid system before breakup shows fractal characteristics [74, 138]. The liquid jet considered here was produced by a low injection pressure triple-disk injector. Details on the experimental setup can be found in [74]. This injector produces a 2D liquid sheet subjected to deformation initiated by the liquid turbulence. The liquid is heptane and the injection pressure is equal to 0.05 MPa. The mean velocity of the jet is 7.5 m/s. Shadow graph images of the jet issuing from the injector are performed. To freeze the jet, a light source (Nano-twin Flash System, HSPS) with a short flash duration ($\approx$ 11 ns) is used. This light source plays the role of the shutter. The camera is a Fuji Digital Camera (FinePix S1 Pro) which has a high number of pixels (3040$\times$2016). The optical arrangement allowed covering a physical field of 10.5$\times$7 mm^2. The corresponding spatial resolution is 3.5 μm/pixel. Fig. A.2.(a) shows the image of the liquid jet issuing from the nozzle. Image analyzing tools were applied to produce a two gray levels image where the liquid appears in black on a white background and to isolate the continuous jet, that is, part of the liquid system in connection with the nozzle (detached drops and ligaments are eliminated). The resulting image shows the shadow of the continuous jet (Fig. A.2.(b)). The textural fractal dimension of the top part of the jet is equal to 1.1 and the structural fractal dimension of the bottom part is equal to 1.43.

(a)

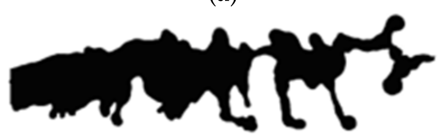

(b)

Figure A.2: Image of the jet of heptane issuing from a triple-disk injector; (a) initial image and (b) shadow of the continuous jet.

This image processing is proposed by Professor Christophe Dumouchel from CORIA, INSA Rouen, France. He provides some natural fractal geometries using this technique. The image used in Chapter 2 is one among the produced shapes.

De-embeding and Proof of equation

B

B.1 De-embeding

In [222, 223], a method is presented to characterize the impedance of an antenna of two ports, and to obtain the differential impedance. We re-

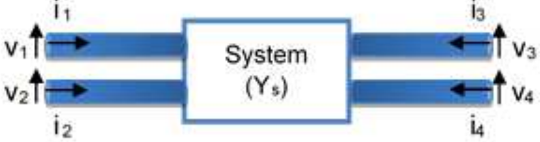

Figure B.1: The schematic for computing the differential system admittance.

formulated this method for the extension to four ports, as shown in Fig. B.1, based on admittance parameters. The differential admittance matrix follows as:

$$I_d = \mathbf{Y}_d \, V_d \tag{B.1}$$

where the above equation (B.1) is re-formulated by introducing the new matrix $\mathbf{A}$ ($2N \times N$), N is the number of antennas. The elements of $\mathbf{A}$ are equal to either "1", "-1", or "0". The matrix is used to select the voltage and current parameters at each port. The differential voltage and current are written as

$$V_d = \begin{bmatrix} V_a \\ V_b \end{bmatrix} = \begin{bmatrix} v_1 - v_2 \\ v_3 - v_4 \end{bmatrix} = \mathbf{A}^T\, V_s \tag{B.2}$$

and

$$I_d = \begin{bmatrix} I_a \\ I_b \end{bmatrix} = \begin{bmatrix} i_1 - i_2 \\ i_3 - i_4 \end{bmatrix} = \mathbf{A}^T\, I_s \tag{B.3}$$

Based on the admittance system matrix $\mathbf{Y}_s$, the constitutive equation of a linear 4-ports network can be presented in matrix form as

$$I_s = \mathbf{Y}_s\, V_s \tag{B.4}$$

then

$$I_d = \mathbf{A}^T\, \mathbf{Y}_s\, V_s \tag{B.5}$$

For the symmetrical balanced antennas and by using the previous equations (B.1) to (B.5), the differential admittance parameters of this system can be defined as

$$\mathbf{Y}_d\, \mathbf{A}^T\, V_s = \mathbf{A}^T\, \mathbf{Y}_s\, V_s \tag{B.6}$$

then

$$\mathbf{Y}_d = \frac{1}{2}\mathbf{A}^T\, \mathbf{Z}_s\, \mathbf{A} \tag{B.7}$$

B.2 Proof of equations (4.28)

The formulation explain how the "additional" (i.e. standing for the effect of the patch) differential admittance matrix can be approximated. It is obtained, in practice, by re-formulating equations (4.14) and (4.22), such that the presence of transmitting and receiving antennas is included in good approximation. Equation (4.3) providing the MoM system of equations can be rewritten as

$$\begin{bmatrix} \mathbf{Z}_t & \mathbf{Z}_{td} \\ \mathbf{Z}_{dt} & \mathbf{Z}_d \end{bmatrix} \begin{bmatrix} I_t \\ I_d \end{bmatrix} = \begin{bmatrix} E_t \\ E_d \end{bmatrix} \tag{B.8}$$

where $\mathbf{Z}_t$ represents the tag (t) self interactions, $\mathbf{Z}_{td}$ or $\mathbf{Z}_{dt}$ are the blocs with antenna-tag interactions, and $\mathbf{Z}_d$ is a bloc containing antenna-antenna interactions. I_t represents a current vector on the tag and I_d is a current vector on the antennas. E_t is the excitation vector on the scatterer, which is a null vector, since the tag is indirectly excited through the fields from the antennas (E_d), as defined in Section 4.2.1. From (B.8), the values of I_d in the presence of all objects (other antennas and scatterer) follows as

$$I_d = \mathbf{Z}_d^{-1} \left[E_d - \mathbf{Z}_{dt} \, I_t \right] \tag{B.9}$$

Assuming that the backward interaction between scatterer and antennas is negligible, the matrix $\mathbf{Z}_{dt}$ neglected in a first instance. Then, the primary currents on the dipole read

$$I_d = \mathbf{Z}_d^{-1} \, E_d \tag{B.10}$$

From (B.8) and (B.10), I_t can be written as

$$I_t = -\mathbf{Z}_t^{-1} \, \mathbf{Z}_{td} \, \mathbf{Z}_d^{-1} \, E_d \tag{B.11}$$

Using (B.9) and (B.11), the current vector I_d corrected for the presence of the tag, can be re-formulated as

$$I_d = \mathbf{Z}_d^{-1} \left[1 + \mathbf{Z}_{dt} \, \mathbf{Z}_t^{-1} \, \mathbf{Z}_{td} \, \mathbf{Z}_d^{-1} \right] \, E_d \tag{B.12}$$

from which we obtain the "additional" current, due to the tag, as

$$\Delta I_d = \mathbf{Z}_d^{-1} \, \mathbf{Z}_{dt} \, \mathbf{Z}_t^{-1} \, \mathbf{Z}_{td} \, \mathbf{Z}_d^{-1} \, E_d \tag{B.13}$$

E_d can be written from the vector of excitations at each port, named Γ in Section 4.2.1, with the help of a "selection" matrix $\mathbf{S}_c$:

$$E_d = \mathbf{S}_c \, \Gamma \tag{B.14}$$

where, $\mathbf{S}_c$ is a $(N_d \times N)$ matrix, N is the number of antennas, and N_d is the number of basis functions used to represent the antennas. $\mathbf{S}_c$ contains zeros, except for entries associated to ports, which are equal to $-w/2$ or $w/2$ at the indices of feed basis functions, where w is the width of the basis function that overlaps the feed point. Then

$$\Delta I_d = \mathbf{Z}_d^{-1} \, \mathbf{Z}_{dt} \, \mathbf{Z}_t^{-1} \, \mathbf{Z}_{td} \, \mathbf{Z}_d^{-1} \, \mathbf{S}_c \, \Gamma \tag{B.15}$$

The port currents of dipoles, I_{prt}, follow as

$$I_{prt} = \mathbf{S}_c^T \, \Delta I_d \tag{B.16}$$

Recalling (4.4) and (4.5), we have

$$\mathbf{E}^e = \mathbf{Z}_{td} \, \mathbf{Z}_d^{-1} \, \mathbf{S}_c \tag{B.17}$$

and

$$\mathbf{E}^{r\,T} = \mathbf{S}_c^T \, \mathbf{Z}_d^{-1} \, \mathbf{Z}_{dt} \tag{B.18}$$

The port current then becomes

$$I_{prt} = \mathbf{E}^{r\,T} \, \mathbf{Z}_t^{-1} \, \mathbf{E}^e \, \Gamma \tag{B.19}$$

The matrix, which relates the "additional" (i.e. after background subtraction) port current to the port voltage, named the "additional" admittance matrix $\mathbf{Y}_a$ then results as

$$\mathbf{Y}_a = \mathbf{E}^{r\,T} \, \mathbf{Z}_t^{-1} \, \mathbf{E}^e \tag{B.20}$$

Then, the ports current of dipoles follows as

$$I_{prt} = \mathbf{Y}_a \, \Gamma \tag{B.21}$$

where $\mathbf{Y}_a$ is obtained from the difference between the differential admittance matrix $\mathbf{Y}_d$ (presence of tag) using (B.7) in Appendix A and without $\mathbf{Y}_{dw}$ (differential admittance for system without tag). This matrix provides the currents based on background extraction. It is calculated as

$$\mathbf{Y}_a = \mathbf{Y}_d - \mathbf{Y}_{dw} \tag{B.22}$$

From equation (4.18) and (4.22), and using (B.21) and (B.22), the response r follows as:

$$r = T^H \, I_{prt} = T^H \, \mathbf{Y}_a \, \Gamma \tag{B.23}$$

List of Publications

C

Journal Papers

[J1] ***D.Oueslati***, *S. N. Jha, C. Craeye, H.Rmili and T.Aguili*, "**Selective Excitation of Chipless Passive RFID Tags Using an SVD-Eigenmode Approach.**", In preparation to submit.

[J2] ***D.Oueslati***, *H.Rmili, M. SHEIKH, C.Dumouchel, J.M.Floch and T.Aguili*, "**Investigation of the Radiation Behavior of a Bio-inspired Irregular-fractal Printed Antenna.**", Submitted In Electromagnetics Research (PIER) Letters.

[J3] *H.Rmili*, ***D. Oueslati***, *L. Laadhr and M. SHEIKH*, "**Design of a chipless RFID tags based on natural fractal.**", Microwave and Optical Technology Letters, vol.58, n.1, Jan. 2016..

[J4] *L. Laadhr, M. Zarouan*, ***D. Oueslati***, *J.M. Floch and H.Rmili*, "**Investigation on Cellular-Automata Irregular Fractal Ultra-Wideband Slot-Antennas.**", Microwave and Optical Technology Letters, vol.57, n.11, Nov. 2015.

[J5] ***D.Oueslati***, *H.Rmili, R.Mittra, M. SHEIKH, J.M.Floch and T.Aguili*, "**Investigation of a Fractal Antenna based on a Natural Tree-Leaf geometry.**", In Preparation to submit in IEEE Antennas and Wireless Propagation

Letters.

Conference Papers

[C1] ***D. Oueslati***, *S. N. Jha, H. Rmili, C. Craeye*, “**Passive RFID Systems: Eigen-Mode Analysis.**”, 7th European Conference of Antenna and Propagation (EuCAP2013), pp.3208-3212, 8-12 April 2013, Gothenburg, Sweden.

[C2] *L.Laadhr, M.Zarouan,* ***D. Oueslati*** *and H. Rmili*, “**Numerical Analysis of a Cellular-Automata Irregular-Fractal Wideband Antenna.**”, 13th Mediterranean Microwave Symposium (MMS 2013), 2-5 Sep. 2013, Saida, Lebanon.

[C3] *M. Halouani,* ***D. Oueslati****, L. Laadhr and H. Rmili*, “**Design Approach of Fractal Antenna for Passive Dual UHF Band RFID Tag.**”, 13th Mediterranean Microwave Symposium (MMS 2013), 2-5 Sep. 2013, Saida, Lebanon.

[C4] ***D. Oueslati****, H. Rmili, C.Dumouchel and J.M.Floch*, “**Numerical Analysis of Radiation Properties of 2D-Irregular Fractal-jet Printed Antenna.**”, 8th European Conference of Antenna and Propagation (EuCAP2014), 6-11 April 2014, Hague, Netherland.

[C5] ***D. Oueslati****, H. Rmili, C.Dumouchel and J.M.Floch*, “**Printed 2D-Irregular Fractal-jet Antenna Miniaturization for Practical Application.**”, 14th Mediterranean Microwave Symposium (MMS 2014), 12-14 Dec. 2014 Marrakech, Morocco.

[C6] ***D. Oueslati***, *S. N. Jha, C. Craeye, H.Rmili and T.Aguili*, “**Chipless Passive RFID Tag Analysis Using Eigenmode Technique.**”, URSI Benelux Forum 2015 - IEEE APS - NARF, Netherland, Dec. 2015.

Bibliography

[1] http://librfidhub.blogspot.be.

[2] www.rfsaw.com.

[3] S. Preradovic and N. Karmakar, *Fully Printable Chipless RFID Tag, Advanced Radio Frequency Identification Design and Applications*, Mar. 2011.

[4] C. Geuzaine and J.-F. Remacle. (2006). [Online]. Available: www.geuz.org/gmsh

[5] Mentor graphics, Wilsonville, OR, USA, Mentor Graphics by IE3D, Hyper Lynx 3D EM, Release 15.2, 2012.

[6] M. Cabedo-Fabres, E. Antonino-Daviu, A. Valero-Nogueira, and M. Bataller, "The theory of characteristic modes revisited: A contribution to the design of antennas for modern applications," *IEEE Antennas Propagat. Mag.*, vol. 49, no. 5, pp. 52–68, Oct. 2007.

[7] D. J. Ludick, J. V. Tonder, and U. Jakobus, "A hybrid tracking algorithm for characteristic mode analysis," in *Int. Conf. on Electromagnetic in Advanced Applicat. (ICEAA)*, Aug 2014, pp. 455–458.

[8] [Online]. Available: http://archive.boston.com/bigpicture/2011/10/nikon_small_world_photomicrogr.html#photo19

[9] H. Stockman, "Communication by means of reflected power," *Proc. IRE*, vol. 36, no. 10, pp. 1196–1204, Oct. 1948.

[10] P. Kitsos and Y. Zhang, *RFID Security: Techniques,Protocols and SystemonChip Design*. Springer Science, New York, 2008.

[11] N. C. Karmakar, *Handbook of Smart Antennas for RFID Systems*. Wiley-IEEE Press, 2010.

[12] K. Finkenzeller, *RFID Handbook: Radio-Frequency Identification Fundamentals and Applications*. 2nd ed., Wiley, 2004.

[13] A. R. Koelle, S. W. Depp, and R. W. Freyman, "Short-range radiotelemetry for electronic identification, using modulated rf backscatter," *Proce. IEEE*, vol. 63, no. 8, pp. 1260–1261, Aug. 1975.

[14] R. Want, "An introduction to RFID technology," *IEEE Pervasive Computing*, vol. 5, no. 1, pp. 25–33, Jan. 2006.

[15] M. Kiani and M. Ghovanloo, "An RFID-based closed-loop wireless power transmission system for biomedical applications," *IEEE Trans. Circuits Syst. II, Exp. Briefs*, vol. 57, no. 4, pp. 260–264, Apr. 2010.

[16] Q. Xiao, C. Boulet, and T. Gibbons, "RFID security issues in military supply chains," in *2nd Int. Conf. Availability, Rel. and Security ARES*, Apr. 2007, pp. 599–605.

[17] R. Pateriya and S. Sharma, "The evolution of RFID security and privacy: A research survey," in *Int. Conf. Commun. Syst. and Network Technologies (CSNT)*, Katra, Jammu, Jun. 2011, pp. 115–119.

[18] H. Rmili, D. Oueslati, L. Ladhar, and M. Sheikh, "Design of a chipless RFID tags based on natural fractal geometries for security applications," *Microw. Opt. Technol. Lett.*, vol. 58, no. 1, pp. 75–82, Jan. 2016.

[19] http://www.rfidjournal.com.

[20] http://www.alientechnology.com/tags.

[21] S. Tedjini, N. Karmakar, E. Perret, A. Vena, R. Koswatta, and R. E-Azim, "Hold the chips: Chipless technology, an alternative technique for RFID," *IEEE Microwave*, vol. 14, no. 5, pp. 56–65, Jul. 2013.

[22] A. Fawky, M. Khaliel, A. El-Awamry, M. El-Hadidy, and T. Kaiser, "Novel pseudo-noise coded chipless RFID system for clutter removal and tag detection," in *IEEE Int. Conf. on RFID*, San Diego, CA, Apr. 2015, pp. 100–104.

[23] S. Preradovic, S. Roy, and N. Karmakar, "RFID system based on fully printable chipless tag for paper-/plastic-ltem tagging," *IEEE Antennas Propagat. Mag.*, vol. 53, no. 5, pp. 15–32, Oct. 2011.

[24] A. F. Peterson, S. L. Ray, and R. Mittra, *Computational Methods for Electromagnetics*. IEEE Press Series on Electromagnetic Wave Theory, Wiley-IEEE Press, 1997.

[25] E. K. Miller, L. Medgyesi-Mitschang, and E. H. Newman, *Computational Electromagnetics: Frequency-Domain Method of Moments*. IEEE Press, 1992.

[26] Rezaiesarlak.R and Manteghi.M, *Chipless RFID: Design Procedure and Detection Techniques*. Springer, 2015.

[27] www.ansys.com/products/electronics/ansys-hfss/hfss-features.

[28] Cst, Computer Simulation Technology. [Online]. Available: www.cst.com

[29] J. M. Jin, *The Finite Element Method in Electromagnetics*. New York: Wiley, 1993.

[30] S. S. Rao, *The Finite Element Method in Engineering*. Butterworth Heinemann, 2010.

[31] M. N. O. Sadiku, "A simple introduction to finite element analysis of electromagnetic problems," *IEEE Trans. Edu.*, vol. 32, no. 2, pp. 85–93, May. 1989.

[32] A. Taflove and S. C. Hagness, *Computational Electrodynamics: The Finite-Difference Time-Domain Method*. 2nd ed. Boston: Artech House, 2000.

[33] W. Yu and R. Mittra, *CFDTD: Conformal Finite Difference Time Domain Maxwell's equations solver, software and user's guide.* Artech House, 2003.

[34] T. Weiland, "A discretization model for the solution of maxwell's equations for six-component fields," *Archiv Elektronik und Uebertragungstechnik*, vol. 31, pp. 116–120, Mar. 1977.

[35] R. F. Harrington, *Field Computation by Moment Methods*. Wiley-IEEE Press, 1993.

[36] H. Holter and H. Steyskal, "Infinite phased-array analysis using fdtd periodic boundary conditions-pulse scanning in oblique directions," *IEEE Trans. Antennas Propag.*, vol. 47, no. 10, pp. 1508–1514, Oct. 1999.

[37] P. A. Tirkas and C. A. Balanis, "Finite-difference time-domain method for antenna radiation," *IEEE Trans. Antennas Propag.*, vol. 40, no. 3, pp. 334–340, Mar. 1992.

[38] D. S. Katz, M. J. Piket-May, A. Taflove, and K. R. Umashankar, "Fdtd analysis of electromagnetic wave radiation from systems containing horn antennas," *IEEE Trans. Antennas Propag.*, vol. 39, no. 8, pp. 1203–1212, Aug. 1991.

[39] U. S. Inan and R. A. Marshall, "Finite difference frequency domain," in *Numerical Electromagnetics*. Cambridge University Press, 2011, pp. 342–355.

[40] R. Sarkis, "Antenna arrays for direction of arrival estimation and imaging : from mutual coupling analysis to real-world design," Ph.D. dissertation, University Louvain la Neuve, Dec. , 2011.

[41] R. F. Harrington, "Matrix methods for field problems," *Proc. IEEE*, vol. 55, no. 2, pp. 136–149, Feb. 1967.

[42] D. S. Weile, G. Pisharody, N.-W. Chen, B. Shanker, and E. Michielssen, "A novel scheme for the solution of the time-domain integral equations of electromagnetics," *IEEE Trans. Antennas Propaga.*, vol. 52, no. 1, pp. 283–295, Jan. 2004.

[43] D. Pozar, "Input impedance and mutual coupling of rectangular microstrip antennas," *IEEE Trans. Antennas Propag.*, vol. 30, no. 6, pp. 1191–1196, Nov 1982.

[44] A. K. Skrivervik and J. R. Mosig, "Analysis of finite phase arrays of microstrip patches," *IEEE Transact. Antennas Propag.*, vol. 41, no. 8, pp. 1105–1114, Aug 1993.

[45] www.feko.info/product-detail/numerical _ methods/mom.

[46] M. C. Fabrés, "Systematic design of antennas using the theory of characteristic modes," Ph.D. dissertation, Pretoria university, 2004.

[47] C.Yikai and W. Chao-Fu, *Characteristic Modes: Theory and Applications in Antenna Engineering*. John Wiley & Sons, Inc., Hoboken, New Jersey, 2015.

[48] B. Nuttawit Surittikul, M.S., "Pattern reconfigurable printed antennas and time domain method of characteristic modes for antenna analysis and design," Ph.D. dissertation, The Ohio State University, 2006.

[49] S. Li and B.-S. Wang, "Field expressions and patterns in elliptical waveguide," *IEEE Trans. Microw. Theory Tech.*, vol. 48, no. 5, pp. 864–867, May. 2000.

[50] M. Schneider and J. Marquardt, "Fast computation of modified mathieu functions applied to elliptical waveguide problems," *IEEE Trans. Microw. Theory Tech.*, vol. 47, no. 4, pp. 513–516, Apr. 1999.

[51] R. E. Collin, *Field Theory of Guided Waves*. McGraw Hill, New York, 1960.

[52] R. Mittra and S. W. Lee, *Analytical Techniques in the Theory of Guided Waves*. Macmillan, New York, 1971.

[53] L. J. Chu, "Physical limitations of omni−directional antennas," *Journal of Applied Physics*, vol. 19, no. 12, pp. 1163–1175, 1948.

[54] R. F. Harrington, "Effect of antenna size on gain, bandwidth and efficiency," *J. Res. Nat. Bur. Stand.D, Radio Propag.*, vol. 64D, no. 1, pp. 1–12, Jan.-Feb. 1960.

[55] Y. Lo, D. Solomon, and W. Richards, "Theory and experiment on microstrip antennas," *IEEE Trans. Antennas Propag.*, vol. 27, no. 2, pp. 137–145, Mar. 1979.

[56] R. K. Mongia and A. Ittipiboon, "Theoretical and experimental investigations on rectangular dielectric resonator antennas," *IEEE Trans. Antennas Propag.*, vol. 45, no. 9, pp. 1348–1356, Sep. 1997.

[57] K. W. Leung, E. H. Lim, and X. S. Fang, "Dielectric resonator antennas: From the basic to the aesthetic," *Proc. IEEE*, vol. 100, no. 7, pp. 2181–2193, July 2012.

[58] R. J. Garbacz, "Modal expansions for resonance scattering phenomena," *Proc. IEEE*, vol. 53, no. 8, pp. 856–864, Aug. 1965.

[59] R. Garbacz and R. Turpin, "A generalized expansion for radiated and scattered fields," *IEEE Trans. Antennas Propag.*, vol. 19, no. 3, pp. 348–358, May 1971.

[60] D. M. Pozar and D. H. Schaubert, *Microstrip Antennas: The Analysis and Design of Microstrip Antennas and Arrays*. IEEE Press, John Wiley & Sons, Inc., Hoboken, New Jersey, 1995.

[61] R. F. Harrington and J. R. Mautz, "Theory of characteristic modes for conducting bodies," *IEEE Trans. Antennas Propag.*, vol. 19, no. 5, pp. 622–628, Sep. 1971.

[62] ——, "Computation of characteristic modes for conducting bodies," *IEEE Trans. Antennas Propag.*, vol. 19, no. 5, pp. 629–639, Sep. 1971.

[63] R. Harrington, J. Mautz, and Y. Chang, "Characteristic modes for dielectric and magnetic bodies," *IEEE Trans. Antennas Propag.*, vol. 20, no. 2, pp. 194–198, Mar. 1972.

[64] H. Alroughani, J. L. T. Ethier, and D. A. McNamara, "On the classification of characteristic modes, and the extension of sub-structure modes to include penetrable material," in *Int. Conf. on Electromagnetics in Advanced Applicat. (ICEAA)*, Aug. 2014, pp. 159–162.

[65] ——, "Observations on computational outcomes for the characteristic modes of dielectric objects," in *IEEE Antennas and Propag. Society Int. Symp. (APSURSI)*, July 2014, pp. 844–845.

[66] R. T. Maximidis, C. L. Zekios, T. N. Kaifas, E. E. Vafiadis, and G. A. Kyriacou, "Characteristic mode analysis of composite metal-dielectric structure, based on surface integral equation/moment method," in *8th Euro. Conf. Antennas and Propag. (EuCAP 2014)*, Apr. 2014, pp. 2822–2826.

[67] Y. Chen and C. F. Wang, "Surface integral equation based characteristic mode formulation for dielectric resonators," in *IEEE Antennas and Propag. Society Int. Symp. (APSURSI)*, July 2014, pp. 846–847.

[68] R. Rezaiesarlak and M. Manteghi, "On the application of characteristic modes for the design of chipless rfid tags," in *IEEE Antennas and Propag. Society Int. Symp. (APSURSI)*, July 2014, pp. 1304–1305.

[69] E. A. Elghannai and R. G. Rojas, "Characteristic mode analysis and design of passive uhf−rfid tag antenna," in *IEEE Int. Conf. on RFID*, Apr. 2014.

[70] D. Oueslati, S. Jha, H. Rmili, and C. Craeye, "Passive RFID systems: Eigen-mode analysis," in *Proc. 7th Eur. Conf. Antennas and Propag. (EuCAP)*, Gothenburg, Apr. 2013, pp. 3208–3212.

[71] Y. Hou and G. Xiao, "Properties of the gram matrices associated with loop-flower basis functions," in *PIERS Proceedings*, Guangzhou, China, August 2014.

[72] B. D. Raines and R. G. Rojas, "Wideband tracking of characteristic modes," in *5th Euro. Conf. Antennas and Propag. (EUCAP)*, April 2011, pp. 1978–1981.

[73] H. Alroughani, "An appraisal of the characteristic modes of composite objects," Ph.D. dissertation, University of Ottawa, Canada, 2013.

[74] S. Grout, C. Dumouchel, J. Cousin, and H. Nuglisch, "Fractal analysis of atomizing liquid flows," *Int. Journal of Multiphase Flow*, vol. 33, no. 9, pp. 1023–1044, 2007.

[75] C. S. Hartmann, "A global saw id tag with large data capacity," in *Proc. IEEE Ultrasonics Symp. 2002*, vol. 1, Munich, Germany, Oct. 2002, pp. 65–69.

[76] S. Tedjini, N. Karmakar, E. Perret, A. Vena, R. Koswatta, and R. E-Azim, "Hold the chips: Chipless technology, an alternative technique for rfid," *IEEE Microw. Mag.*, vol. 14, no. 5, pp. 56–65, Jul. 2013.

[77] L. Yang, A. Rida, R. Vyas, and M. M. Tentzeris, "Rfid tag and rf structures on a paper substrate using inkjet-printing technology," *IEEE Trans. Microw. Theory Tech.*, vol. 55, no. 12, pp. 2894–2901, Dec. 2007.

[78] A. Vena, E. Perret, and S. Tedjini, "High−capacity chipless rfid tag insensitive to the polarization," *IEEE Trans. Antennas Propag.*, vol. 60, no. 10, pp. 4509–4515, Oct. 2012.

[79] T. Han, W. Wang, J. M. Lin, H. Wu, H. Wang, and Y. Shui, "P2h−2 phases of carrier wave in a saw identification tags," in *IEEE Ultrasonics Symp.*, New York, NY, Oct. 2007, pp. 1669–1672.

[80] T. Han, W. Wang, H. Wu, and Y. Shui, "Reflection and scattering characteristics of reflectors in saw tags," *IEEE Trans. Ultrason. Ferroelectr. Freq. Control*, vol. 55, no. 6, pp. 1387–1390, June 2008.

[81] N. Saldanha and D. C. Malocha, "P4j−1 design parameters for saw multi-tone frequency coded reflectors," in *IEEE Ultrasonics Symp.*, New York, NY, Oct. 2007, pp. 2087–2090.

[82] S. Harma, W. G. Arthur, C. S. Hartmann, R. G. Maev, and V. P. Plessky, "Inline saw rfid tag using time position and phase encoding," *IEEE Trans. Ultrason. Ferroelectr.Freq. Control*, vol. 55, no. 8, pp. 1840–1846, Aug. 2008.

[83] S. Harma, W. G. Arthur, R. G. Maev, C. S. Hartmann, and V. P. Plessky, "P0−14 inline saw rfid tag using time position and phase encoding," in *IEEE Ultrasonics Symp.*, New York, NY, Oct. 2007, pp. 1239–1242.

[84] L. Wei, H. Tao, and S. Yongan, "Surface acoustic wave based radio frequency identification tags," in *IEEE Int. Conf. e-Business Eng. (ICEBE '08)*, vol. 1, Xi'an, China, Oct. 2008, pp. 563–567.

[85] J. Yao, J. Liu, and B. Gao, "The realization of a passive identification tag transmitter based on saw," in *4th Int. Conf. Wireless Commun., Networking and Mobile Computing*, Dalian, Oct. 2008, pp. 1–4.

[86] D. Enguang and F. Guanping, "Passive and remote sensing based upon surface acoustic wave in special environments," in *SBMO/IEEE MTT−S Inte. Proc. Microwave and Opt. Conf., Linking to the Next Century*, Natal, Aug. 1997, pp. 133–139.

[87] L. Zheng, S. Rodriguez, L. Zhang, B. Shao, and L.-R. Zheng, "Design and implementation of a fully reconfigurable chipless rfid tag using inkjet printing technology," in *IEEE Int. Symp. Circuits and Sys.*, Seattle, WA, pp. 1524-1527, May 2008, May 2008, pp. 1524–1527.

[88] S. Shrestha, M. Balachandran, M. Agarwal, V. V. Phoha, and K. Varahramyan, "A chipless rfid sensor system for cyber centric monitoring applications," *IEEE Trans. Microw. Theory Tech.*, vol. 57, no. 5, pp. 1303–1309, May 2009.

[89] J. McVay, A. Hoorfar, and N. Engheta, "Space−filling curve rfid tags," in *IEEE Radio and Wireless Symp.*, San Diego, USA, Jan. 2006, pp. 199–202.

[90] I. Jalaly and I. D. Robertson, "Capacitively−tuned split microstrip resonators for rfid barcodes," in *European Microwave Conf. (EuMC)*, vol. 2, Paris, France, Oct. 2005, pp. 1–4.

[91] S. Preradovic, I. Balbin, N. C. Karmakar, and G. F. Swiegers, "Multiresonator−based chipless rfid system for low-cost item tracking," *IEEE Trans. Microw. Theory Tech.*, vol. 57, no. 5, pp. 1411–1419, May 2009.

[92] S. Preradovic, I. Balbin, N. C. Karmakar, and G. Swiegers, "Chipless frequency signature based rfid transponders," in *Euro. Conf. Wireless Technology (EuWiT)*, Amsterdam, Oct. 2008, pp. 302–305.

[93] D. Girbau, J. Lorenzo, A. Lazaro, C. Ferrater, and R. Villarino, "Frequency-coded chipless rfid tag based on dual-band resonators," *IEEE Antennas Wireless Propap. Lett.*, vol. 11, pp. 126–128, Jan. 2012.

[94] R. Das. Chipless rfid - the end game. IDTechEx, Cambridge,MA, Internet article (Feb. 2006).

[95] K. C. Jones. Invisible tattoo ink for chipless rfid safe, company says. EE Times white paper (Oct. 2006).

[96] J. Collins. Rfid fibers for secure applications. (Mar. 2004).

[97] S. Preradovic, I. Balbin, N. Karmakar, and G. Swiegers, "A novel chipless RFID system based on planar multiresonators for barcode replacement," in *IEEE Int. Conf. on RFID*, Apr. 2008, pp. 289–296.

[98] P. Narkcharoen and S. Pranonsatit, "The applications of fill until full (fuf) for multiresonator-based chipless rfid system," in *8th Int. Conf. Elect. Eng./Electron., Comput., Telecommun. and Inform. Technology (ECTI-CON)*, Khon Kaen, May 2011, pp. 176–179.

[99] M. S. Bhuiyan, A. Azad, and N. Karmakar, "Dual-band modified complementary split ring resonator MCSRR based multi-resonator circuit for chipless rfid tag," in *8th Int. Conf. Intelligent Sensors, Sensor Networks and Inform. Proc.*, Melbourne, VIC, Apr. 2013, pp. 277–281.

[100] G. A. Casula, G. Montisci, P. Maxia, and G.Mazzarella, "A narrowband chipless multiresonator tag for uhf rfid," *Journal of Electromagnetic Waves and Applications*, vol. 28, pp. 214–227, Jan. 2014.

[101] S. Mukherjee, "Chipless radio frequency identification by remote measurement of complex impedance," in *Eur. Microwave Conf.*, Munich, Oct. 2007, pp. 1007–1010.

[102] L. Yang, R. Zhang, D. Staiculescu, C. P. Wong, and M. M. Tentzeris, "A novel conformal rfid−enabled module utilizing inkjet−printed antennas and carbon nanotubes for gas-detection applications," *IEEE Antennas Wireless Propap. Lett.*, vol. 8, pp. 653–656, 2009.

[103] A. Vena, E. Perret, and S. Tedjini, "Chipless rfid tag using hybrid coding technique," *IEEE Trans. Microw. Theory Tech.*, vol. 59, pp. 3356–3364, Dec. 2011.

[104] M. Manteghi, "A space−time−frequency target identification technique for chipless rfid applications," in *IEEE Int. Symp. Antennas and Propag. (APSURSI)*, Spokane, WA, July 2011, pp. 3350–3351.

[105] A. Vena, E. Perret, and S. Tedjni, "A depolarizing chipless RFID tag for robust detection and its FCC compliant UWB reading system," *IEEE Trans. Microw. Theory Tech.*, vol. 561, pp. 2982–2994, Aug. 2013.

[106] C. Mandel, M. Schussler, M. Maasch, and R. Jakoby, "A novel passive phase modulator based on lh delay lines for chipless microwave rfid applications," in *IEEE MTT−S Int. Microwave Workshop on Wireless Sensing, Local Positioning, and RFID (MWS)*, Cavtat, Sept. 2009, pp. 1–4.

[107] B. Shao, Q. Chen, R. Liu, and L.-R. Zheng, "A reconfigurable chipless RFID tag based on sympathetic oscillation for liquid-bearing applications," in *IEEE Int. Conf. on RFID*, Apr. 2011, pp. 170–175.

[108] Y. Chen, Z. Chen, and L. Xu, "RFID system security using identity-based cryptography," in *3rd Int. Symp. on Intell. Informa. Technology and Security Informatics (IITSI)*, Jinggangshan, Apr. 2010, pp. 460–464.

[109] E. M. Amin, M. S. Bhuiyan, N. C. Karmakar, and B. Winther-Jensen, "Development of a low cost printable chipless rfid humidity sensor," *IEEE Sensors J.*, vol. 14, no. 1, pp. 140–149, Jan 2014.

[110] S. Preradovic, S. M. Roy, and N. C. Karmakar, "Rfid system based on fully printable chipless tag for paper-/plastic-ltem tagging," *IEEE Antennas Propagat. Mag.*, vol. 53, no. 5, pp. 15–32, Oct. 2011.

[111] A. Lazaro, A. Ramos, D. Girbau, and R. Villarino, "Chipless uwb rfid tag detection using continuous wavelet transform," *IEEE Antennas and Wireless Propag. Lett.*, vol. 10, pp. 520–523, June 2011.

[112] A. Ramos, D. Girbau, A. Lazaro, and S. Rima, "Ir-uwb radar system and tag design for time-coded chipless rfid," in *6th Euro. Conf. on Antennas and Propag. (EUCAP)*, Mar. 2012, pp. 2491–2494.

[113] R. E. A. Anee and N. C. Karmakar, "Chipless rfid tag localization," *IEEE Trans. Microw. Theory Tech.*, vol. 61, no. 11, pp. 4008–4017, Nov. 2013.

[114] P. Kalansuriya, N. C. Karmakar, and E. Viterbo, "On the detection of frequency-spectra-based chipless rfid using uwb impulsed interrogation," *IEEE Trans. Microw Theory Tech.*, vol. 60, no. 12, pp. 4187–4197, Dec. 2012.

[115] I. Balbin and N. C. Karmakar, "Phase-encoded chipless rfid transponder for large-scale low-cost applications," *IEEE Microw. Wireless Compon. Lett.*, vol. 19, no. 8, pp. 509–511, Aug. 2009.

[116] M. Zomorrodi, N. C. Karmakar, and S. G. Bansal, "Introduction of electromagnetic image-based chipless rfid system," in *IEEE Eighth Int. Conf. on Intelligent Sensors, Sensor Networks and Inform. Process.*, Apr. 2013, pp. 443–448.

[117] M. A. Islam and N. Karmakar, "Design of a 16-bit ultra-low cost fully printable slot-loaded dual-polarized chipless rfid tag," in *Asia-Pacific Microw. Conf.*, Dec. 2011, pp. 1482–1485.

[118] P. Kalansuriya, N. Karmakar, and E. Viterbo, "Signal space representation of chipless rfid tag frequency signatures," in *IEEE Global Telecommun. Conf. (GLOBECOM)*, Houston, TX, USA, Dec. 2011, pp. 1–5.

[119] L. Xu and K. Huang, "Design of compact trapezoidal bow−tie chipless rfid tag," *Int. Journal of Antennas and Propag.*, vol. 2015, pp. 1–7, Oct. 2014.

[120] B. B. Mandelbrot, *The Fractal Geometry of Nature*, Aug. 1982.

[121] D. H. Werner, R. L. Haupt, and P. L. Werner, "Fractal antenna engineering: the theory and design of fractal antenna arrays," *IEEE Antennas Propag. Mag.*, vol. 41, no. 5, pp. 37–58, Oct. 1999.

[122] D. H. Werner and S. Ganguly, "An overview of fractal antenna engineering research," *IEEE Antennas Propag. Mag.*, vol. 45, no. 1, pp. 38–57, Feb. 2003.

[123] C. Puente-Baliarda, J. Romeu, R. Pous, and A. Cardama, "On the behavior of the sierpinski multiband fractal antenna," *IEEE Trans. Antennas Propag.*, vol. 46, no. 4, pp. 517–524, Apr. 1998.

[124] C. P. Baliarda, J. Romeu, and A. Cardama, "The koch monopole: a small fractal antenna," *IEEE Trans. Antennas Propag.*, vol. 48, no. 11, pp. 1773–1781, Nov. 2000.

[125] C. Borja, G. Font, S. Blanch, and J. Romeu, "High directivity fractal boundary microstrip patch antenna," *Electronics Lett.*, vol. 36, no. 9, pp. 778–779, Apr. 2000.

[126] C. Puente, J. Claret, F. Sagues, J. Romeu, M. Q. Lopez-Salvans, and R. Pous, "Multiband properties of a fractal tree antenna generated by electrochemical deposition," *Electronics Lett.*, vol. 32, no. 25, Dec. 1996.

[127] H. Rmili, J. M. Floch, and H. Zangar, "Experimental study of a 2d−irregular fractal−jet printed antenna," in *3rd Euro. Conf. Antennas and Propag.(EUCAP)*, Mar. 2009, pp. 2403–2406.

[128] C. Dumond, M. Khelloufi, and L. Allam, "Experimental study of 2-d electrochemically deposited random fractal monopole antennas," in *Progress In Electromagnetics Research C*, vol. 36, Jan. 2013, pp. 119–130.

[129] H. Rmili, O. E. Mrabet, J. M. Floc'h, and J. L. Miane, "Study of an electrochemically-deposited 3-d random fractal tree-monopole antenna," *IEEE Trans. Antennas Propag.*, vol. 55, no. 4, pp. 1045–1050, Apr. 2007.

[130] H. Rmili, J.-L. Miane, J.-M. Floch, and H. Zangar, "Design of multi and wideband 3d fractal monopole antenna for wireless operations in l- and s-bands," *Microwave Opt. Technol. Lett.*, vol. 51, no. 8, pp. 1976–1979, Aug. 2009.

[131] D. Oueslati, H. Rmili, C. Dumouchel, and J. M. Floch, "Numerical analysis of radiation properties of 2d-irregular fractal-jet printed antenna," in *8th Euro. Conf. Antennas and Propag. (EuCAP)*, Apr. 2014, pp. 2165–2169.

[132] D. Oueslati, H. Rmili, C. Dumouchel, J. M. Floch, and L. Laadhar, "Numerical analysis of the size effect on a printed 2d-irregular fractal-jet antenna," in *Proc. Mediterranean Microwave Symp. (MMS)*, Dec. 2014, pp. 1–4.

[133] H. Rmili, J. M. Floch, and H. Zangar, "Experimental study of a 2-d irregular fractal-jet printed antenna," *IEEE Antennas Wireless Propag. Lett.*, vol. 8, pp. 328–331, Feb. 2009.

[134] S. V. Krupenin, V. V. Kolesov, A. A. Potapov, and N. G. Petrova, "The irregular-shaped fractal antennas for ultra wideband radio systems," in *3rd Int. Conf. on Ultrawideband and Ultrashort Impulse Signals*, Sept. 2006, pp. 323–325.

[135] www.fractenna.com.

[136] J. K. Pakkathillam, M. Kanagasabai, C. Varadhan, and P. Sakthivel, "A novel fractal antenna for uhf near-field rfid readers," *IEEE Antennas Wireless Propag. Lett.*, vol. 12, pp. 1141–1144, 2013.

[137] K.Vasanthi, "A novel fractal antenna for uhf near-field rfid readers," *Int. J. of Innovative Research in Sci., Eng. and Technology*, vol. 12, pp. 1141–1144, 2013.

[138] C. Dumouchel, J. Cousin, and K. Triballier, "Analysis of liquid−gas interface at low weber number: interface length and fractal dimension," *Experiments in Fluids*, vol. 39, no. 4, pp. 651–666, 2005.

[139] www.mathworks.com/products/matlab.

[140] I. B. Trad, H. Rmili, J. M. Floch, and H. Zangar, "Design of a dual-band rejected uwb printed monopole antenna," in *5th Euro. Conf. Antennas and Propag. (EUCAP)*, April 2011, pp. 627–630.

[141] M. S. Bhuiyan and N. Karmakar, "Chipless rfid tag based on split−wheel resonators," in *7th Euro. Conf. Antennas and Propag. (EuCAP)*, April 2013, pp. 3054–3057.

[142] M. A. Islam, Y. Yap, N. Karmakar, and A. K. M. Azad, "Orientation independent compact chipless rfid tag," in *IEEE Int. Conf. RFID-Technologies and Applicat. (RFID-TA)*, Nov. 2012, pp. 137–141.

[143] M. A. Islam and N. C. Karmakar, "A novel compact printable dual−polarized chipless rfid system," *IEEE Trans. Microw. Theory Tech.*, vol. 60, no. 7, pp. 2142–2151, July 2012.

[144] H. S. Jang, W. G. Lim, K. S. Oh, S. M. Moon, and J. W. Yu, "Design of low−cost chipless system using printable chipless tag with electromagnetic code," *IEEE Microw. Wireless Compon. Lett.*, vol. 20, no. 11, pp. 640–642, Nov. 2010.

[145] C. E. Baum, "On the singularity expansion method for the solution of electromagnetic interaction problems," *EMP Interaction Note 8, Air Force Weapons Laboratory, Kirkland AFB*, Feb. 1971.

[146] C. E. Baum, E. J. Rothwell, K. M. Chen, and D. P. Nyquist, "The singularity expansion method and its application to target identification," *Proc. IEEE*, vol. 79, no. 10, pp. 1481–1492, Oct. 1991.

[147] J. Chauveau, N. de Beaucoudrey, and J. Saillard, "Selection of contributing natural poles for the characterization of perfectly conducting targets in resonance region," *IEEE Trans. Antennas Propag.*, vol. 55, no. 9, pp. 2610–2617, Sept. 2007.

[148] F. Tesche, "On the analysis of scattering and antenna problems using the singularity expansion technique," *IEEE Trans. Antennas Propag.*, vol. 21, no. 1, pp. 53–62, Jan. 1973.

[149] S. Licul and W. A. Davis, "Unified frequency and time-domain antenna modeling and characterization," *IEEE Trans. Antennas Propag.*, vol. 53, no. 9, pp. 2882–2888, Sept. 2005.

[150] C. Marchais, B. Uguen, A. Sharaiha, G. L. Ray, and L. L. Coq, "Compact characterisation of ultra wideband antenna responses from frequency measurements," *IET Microw. Antennas Propag.*, vol. 5, no. 6, pp. 671–675, Apr. 2011.

[151] F. Sarrazin, J. Chauveau, P. Pouliguen, P. Potier, and A. Sharaiha, "Accuracy of singularity expansion method in time and frequency domains to characterize antennas in presence of noise," *IEEE Trans. Antennas Propag.*, vol. 62, no. 3, pp. 1261–1269, March 2014.

[152] A. Blischak and M. Manteghi, "Pole residue techniques for chipless rfid detection," in *IEEE Antennas and Propag. Society Int. Symp.*, Jun. 2009, pp. 1–4.

[153] R. Rezaiesarlak and M. Manteghi, "Complex-natural-resonance-based design of chipless rfid tag for high-density data," *IEEE Trans. Antennas Propag.*, vol. 62, no. 2, pp. 898–904, Feb. 2014.

[154] C.-T. Tai, *Dyadic Green Functions in Electromagnetic Theory*. Institute of Electrical and Electronics Engineers, Université du Michigan, 1992.

[155] M. Manteghi and R. Rezaiesarlak, *Design Procedure and Detection Techniques*. Cham, Switzerland: Springer Int. Publishing AG, 2015.

[156] D. Ferreira, A. Tinoco Salazar, I. Bianchi, and J. d. S. Lacava, "Planar multilayer structure analysis: an educational approach," *Journal of Microwaves, Optoelectronics and Electromagnetic Applications*, vol. 11, pp. 93 – 106, Jun 2012.

[157] K. Nikellis, N. K. Uzunoglu, Y. Koutsoyannopoulos, and S. Bantas, "Full-wave modeling of stripline structures in multilayer dielectrics," *Progress In Electromagnetics Research, PIER*, vol. 57, pp. 253–264, 2006.

[158] R. Plonsey and R. E. Collin, *Principles and Applications of Electromagnetic Fields*. New York: McGraw-Hill, 1961.

[159] R. Mittra, *Computer Techniques for Electromagnetics*. Elmsford, NY: Pergamon Press, 1973.

[160] R. Hansen, *Moment Methods in Antennas and Scattering*. Boston: Artech House, 1990.

[161] J. Moore and R. Pizer, *Moment Methods in Electromagnetics: Techniques and Applications*. New York: John Wiley and Sons, 1984.

[162] N. K. N. Morita and J. Mautz, *Integral Equation Methods for Electromagnetics*. Boston: Artech House, 1992.

[163] W. C. Gibson, *The Method of Moments in Electromagnetics*. Champon & Hall, CRC Press, Taylors and Francis Group, 2008.

[164] S. N. Jha, "Fast spectral-domain macro basis function analysis of large arrays of printed antennas," Ph.D. dissertation, University Louvain la Neuve, Aug. , 2014.

[165] A. W. Glisson, "On the developement of numerical techniques for treating arbitrarily- shaped surfaces," Ph.D. dissertation, University of Mississippi, 1978.

[166] R. Mittra and C. Klein, *Numerical and Asymptotic Techniques in Electromagnetics; Stability and Convergence of Moment Method Solutions*. Chapter 5, Springer-Verlag Berlin Heidelberg New York, pp.129-163, 1975.

[167] T. Sarkar, "A note on the choice weighting functions in the method of moments," *IEEE Trans. Antennas Propag.*, vol. 33, no. 4, pp. 436–441, April 1985.

[168] T. Sarkar, A. Djordjevic, and E. Arvas, "On the choice of expansion and weighting functions in the numerical solution of operator equations," *IEEE Trans. Antennas Propag.*, vol. 33, no. 9, pp. 988–996, Sep. 1985.

[169] S. Rao, D. Wilton, and A. Glisson, "Electromagnetic scattering by surfaces of arbitrary shape," *IEEE Trans. Antennas Propag.*, vol. 30, no. 3, pp. 409–418, May 1982.

[170] D. Schaubert, D. Wilton, and A. Glisson, "A tetrahedral modeling method for electromagnetic scattering by arbitrarily shaped inhomogeneous dielectric bodies," *IEEE Trans. Antennas Propag.*, vol. 32, no. 1, pp. 77–85, Jan. 1984.

[171] S.-O. Park, C. Balanis, and C. Birtcher, "Analytical evaluation of the asymptotic impedance matrix of a grounded dielectric slab with roof-top functions," *IEEE Trans. Antennas Propag.*, vol. 46, no. 2, pp. 251–259, Feb. 1998.

[172] M. Bailey and M. Deshpande, "Integral equation formulation of microstrip antennas," *IEEE Trans. Antennas Propag.*, vol. 30, no. 4, pp. 651–656, Jul 1982.

[173] C. Geuzaine and J. Remacle, "Gmsh: a three-dimensional finite element mesh generator with built -in pre- and post-processing facilities," *Int. Journal for Numerical Methods in Engineering*, vol. 79, no. 11, pp. 1309–1331, Oct. 2009.

[174] K. Michalski and D. Zheng, "Electromagnetic scattering and radiation by surfaces of arbitrary shape in layered media. I. theory," *IEEE Trans. Antennas Propag.*, vol. 38, no. 3, pp. 335–344, Mar. 1990.

[175] D. Gonzalez Ovejero, "Analysis of non-periodic antenna arrays : an accelerated macro basis function approach," Ph.D. dissertation, University Louvain la Neuve, Juin , 2012.

[176] K. Michalski and J. Mosig, "Multilayered media Green's functions in integral equation formulations," *IEEE Trans. Antennas Propag.*, vol. 45, no. 3, pp. 508–519, Mar. 1997.

[177] A. K. Skrivervik and J. R. Mosig, "Analysis of printed array antennas," *IEEE Trans. Antennas Propag.*, vol. 45, no. 9, pp. 1411–1418, Sept. 1997.

[178] K. L. Lai, L. Tsang, and C. C. Huang, "Spatial domain green's functions for planar multilayered structures," *Microw. Opt. Technol. Lett.*, vol. 44, no. 1, pp. 86–91, 2005.

[179] C.Craeye, "Method of moments simulations of antennas printed on layered medium," *Internal Note, UCL*, May 2010.

[180] F. Ling, D. Jiao, and J.-M. Jin, "Efficient electromagnetic modeling of microstrip structures in multilayer media," *IEEE Trans. Microw. Theory Tech.*, vol. 47, no. 9, pp. 1810–1818, Sep. 1999.

[181] A. Fort, F. Keshmiri, G. R. Crusats, C. Craeye, and C. Oestges, "A body area propagation model derived from fundamental principles: Analytical analysis and comparison with measurements," *IEEE Transactions on Antennas and Propagation*, vol. 58, no. 2, pp. 503–514, Feb. 2010.

[182] D. Oueslati, S. Jha, C. Craeye, H.Rmili, and T. Aguili, "Selective excitation of chipless passive rfid tags using an svd-eigenmode approach," *Submitted in IEEE Trans. Antennas Propag.*, Jully 2016.

[183] R. Harrington and J. Mautz, "Control of radar scattering by reactive loading," *IEEE Trans. Antennas Propag.*, vol. 20, no. 4, pp. 446–454, Jul. 1972.

[184] ——, "Pattern synthesis for loaded n-port scatterers," *IEEE Trans. Antennas Propag.*, vol. 22, no. 2, pp. 184–190, Mar. 1974.

[185] J. R. Mautz and R. F. Harrington, "Radiation and scattering from bodies of revolution," *Appl. Scientific Research*, vol. 20, no. 1, pp. 405–435, Jan. 1969.

[186] B. A. Austin and K. P. Murray, "The application of characteristic mode techniques to vehicle-mounted nvis antennas," *IEEE Antennas Propagat. Mag.*, vol. 40, no. 1, pp. 7–21, 30, Feb. 1998.

[187] R. J. Garbacz, "A generalized expansion for radiated and scattered fields," Ph.D. dissertation, Ph.D. dissertation, Ohio, State University, Columbus, 1968.

[188] Z. Bai, J. Demmel, J. Dongarra, A. Ruhe, and H. van der Vorst, *Templates for the Solution of Algebraic Eigenvalue Problems*. Society for Industrial and Applied Mathematics, 2000.

[189] S. Rao, D. Wilton, and A. Glisson, "Electromagnetic scattering by surfaces of arbitrary shape," *IEEE Trans. Antennas Propag.*, vol. 30, no. 3, pp. 409–418, 1982.

[190] M. Capek, P. Hazdra, and J. Eichler, "A method for the evaluation of radiation q based on modal approach," *IEEE Transactions on Antennas and Propagation*, vol. 60, no. 10, pp. 4556–4567, Oct. 2012.

[191] G. H. Golub and C. F. V. Loan, *Matrix Computations*. Johns Hopkins Univ. Press, third edition, 1996.

[192] W. H. Press, S. A. Teukolsky, W. T. Vetterling, and B. P. Flannery, "Numerical recipes in c." Cambridge University Press, U.K., 1992.

[193] J. Dongarra, C. Moler, J. Bunch, and G. Stewart, *LINPACK Users' Guide*. Society for Industrial and Applied Mathematics, 1979.

[194] M. Oliveros, M. Carminati, A. Zanutta, T. Mattila, S. Jussila, K. Nummila, A. Bianco, G. Lanzani, and M. Caironi, "Photosensitive chipless radio-frequency tag for low-cost monitoring of light-sensitive goods," *Sensors and Actuators B, Chemical*, vol. 223, pp. 839–845, Feb. 2016.

[195] D. Maimut and K. Ouafi, "Lightweight cryptography for RFID tags," *IEEE Security & Privacy*, vol. 10, no. 2, pp. 76–79, Mar. 2012.

[196] Z. Shen and R. H. Macphie, "Rigorous evaluation of the input impedance of a sleeve monopole by modal-expansion method," *IEEE Trans. Antennas Propag.*, vol. 44, no. 12, pp. 1584–1591, Dec. 1996.

[197] H. Stuart, "Eigenmode analysis of small multielement spherical antennas," *IEEE Trans. Antennas Propag.*, vol. 56, no. 9, pp. 2841–2851, Sept. 2008.

[198] Comsol multiphysics.

[199] Ansys HFSS.

[200] G. Shaker, N. Sangary, and S. Safavi-Naeini, "Notes on eigen modal analysis of antennas," *Progress In Electromagnetics Research B*, vol. 62, pp. 153–165, 2015.

[201] C. T. Famdie, W. L. Schroeder, and K. Solbach, "Numerical analysis of characteristic modes on the chassis of mobile phones," in *1st Eur. Conf. Antennas and Propag. (EuCAP)*, Nice, Nov. 2006, pp. 1–6.

[202] B. Souny, H. Aubert, and H. Baudrand, "Elimination of spurious solutions in the calculation of eigenmodes by moment method," *IEEE Trans. Microw. Theory Tech.*, vol. 44, no. 1, pp. 154–157, Jan. 1996.

[203] J. Chalas, K. Sertel, and J. Volakis, "Computation of the Q limits for arbitrary-shaped antennas using characteristic modes," in *IEEE Int. Symp. Antennas and Propag. (APSURSI)*, Spokane, WA, Jul. 2011, pp. 772–774.

[204] M. Araujo, J. Rodriguez, J. Bertolo, L. Landesa, J. Taboada, and F. Obelleiro, "Geometrically based preconditioner for the fast multipole method using rooftop basis functions and Galerkin testing procedure," in *IEEE Int. Symp. Antennas and Propag. Soc. (APSURSI '09)*, Charleston, SC, Jun. 2009, pp. 1–4.

[205] N. Herscovici and D. Pozar, "Analysis and design of multilayer printed antennas: a modular approach," *IEEE Trans. Antennas Propag.*, vol. 41, no. 10, pp. 1371–1378, Oct. 1993.

[206] W. L. Stutzman and G. A. Thiele, *Antenna Theory and Design*. 2nd ed., John Wiley & Sons, Inc., Hoboken, New York, NY, 1998.

[207] C. Balanis, *Antenna Theory: Analysis and Design*. Harper & Row, Inc., Hoboken, New York, NY, 1982.

[208] M. Abedin and M. Ali, "Effects of a smaller unit cell planar EBG structure on the mutual coupling of a printed dipole array," *IEEE Antennas Wireless Propag. Lett.*, vol. 4, pp. 274–276, 2005.

[209] L. Aberbour and C. Craeye, "On the radiation resistance of planar monopole antennas," *IEEE Trans. Antennas Propag.*, vol. 57, no. 4, pp. 1035–1042, Apr. 2009.

[210] D. J. Ludick, U. Jakobus, and M. Vogel, "A tracking algorithm for the eigenvectors calculated with characteristic mode analysis," in *8th Eur. Conf. Antennas and Propag.(EuCAP)*, April 2014, pp. 569–572.

[211] Z. Miers and B. K. Lau, "Wideband characteristic mode tracking utilizing far-field patterns," *IEEE Antennas Wireless Propag. Lett.*, vol. 14, pp. 1658–1661, Mar. 2015.

[212] G. Helmberg, *Introduction to Spectral Theory in Hilbert Space: North-Holland Series in Applied Mathematics and Mechanics*. North-Holland and American Elsevier, 1969.

[213] R. R. Patil, V. R. M, and P. V. Hunagund, "Simulation characterization of patch antenna using ultra thin conductors for wireless lan applications," *IJCA Proceedings on National Conference on Recent Advances in Information Technology*, no. 4, pp. 1–4, February 2014.

[214] M. Capek, P. Hazdra, P. Hamouz, and J. Eichler, "A method for tracking characteristic numbers and vectors," *Progress In Electromagnetics Research B*, vol. 33, pp. 115–134, 2011.

[215] E. Safin and D. Manteuffel, "Advanced eigenvalue tracking of characteristic modes," *IEEE Transactions on Antennas and Propagation*, vol. 64, no. 7, pp. 2628–2636, July 2016.

[216] H. Peitgen, H. Jurgens, and D. Saupe, *Chaos and Fractals: New Frontiers of Science*, 1992.

[217] M. Dekking, J. L. Vehel, E. Lutton, and C. T. (editors), *Fractals: Theory and Application in Engineering*, 1999.

[218] C. Dumond, M. Khelloufi, and L. Allam, "Experimental study of 2-d electrochemicallydeposited random fractal monopole antennas," *Progress In Electromagnetics Research C*, vol. 36, pp. 119–130, Jan. 2013.

[219] M. Kitlinski and R. Kieda, "Compact cpw-fed sierpinski fractal monopole antenna," *Electronics Lett.*, vol. 40, no. 22, pp. 1387–1388, Oct. 2004.

[220] B. Mirzapour and H. R. Hassani, "Size reduction and bandwidth enhancement of snowflake fractal antenna," *IET Microw. Antennas Propag.*, vol. 2, no. 2, pp. 180–187, Mar. 2008.

[221] K. Vinoy, "Fractal shaped antenna elements for wide-and multi-band wireless application," Ph.D. dissertation, The Pennsylvania State University, 2002.

[222] R. Meys and F. Janssens, "Measuring the impedance of balanced antennas by an S -parameter method," *IEEE Antennas Propagat. Mag.*, vol. 40, no. 6, pp. 62–65, Dec. 1998.

[223] X. Qing, C. K. Goh, and Z. N. Chen, "Impedance characterization of RFID tag antennas and application in tag co-design," *IEEE Trans. Microw. Theory Tech.*, vol. 57, no. 5, pp. 1268–1274, May 2009.